



저작자표시 2.0 대한민국

이용자는 아래의 조건을 따르는 경우에 한하여 자유롭게

- 이 저작물을 복제, 배포, 전송, 전시, 공연 및 방송할 수 있습니다.
- 이차적 저작물을 작성할 수 있습니다.
- 이 저작물을 영리 목적으로 이용할 수 있습니다.

다음과 같은 조건을 따라야 합니다:



저작자표시. 귀하는 원저작자를 표시하여야 합니다.

- 귀하는, 이 저작물의 재이용이나 배포의 경우, 이 저작물에 적용된 이용허락조건을 명확하게 나타내어야 합니다.
- 저작권자로부터 별도의 허가를 받으면 이러한 조건들은 적용되지 않습니다.

저작권법에 따른 이용자의 권리는 위의 내용에 의하여 영향을 받지 않습니다.

이것은 [이용허락규약\(Legal Code\)](#)을 이해하기 쉽게 요약한 것입니다.

[Disclaimer](#) 

공학박사 학위논문

**Development of Full Electromagnetic
Start-up Model and its Validation for the
Prediction of Ohmic Discharges in
Spherical Tori**

구형 토러스 장치에서의 저항 가열 방전 예측을
위한 전자기장 시동 모델 개발과 검증

2023년 2월

서울대학교 대학원

에너지시스템공학부

김 성 철

Abstract

Development of Full Electromagnetic Start-up Model and its Validation for the Prediction of Ohmic discharges in Spherical Tori

Seong Cheol Kim

Department of Energy System Engineering

(Fusion & Plasma Engineering)

The Graduate School

Seoul National University

A tokamak start-up model is developed to predict ohmic discharges in VEST (Versatile Experiment Spherical Torus) which has been operated at Seoul National University. There is significant electromagnetic effect by the central solenoid, PF coils, and vacuum vessel eddy currents and impurity effect by the plasma wall interaction in overall discharge of VEST. Therefore, it is required to consider these effects for the model development. For development of the tokamak start-up model, a zero dimensional burn-through simulator, DYON is utilized with dedicated atomic processes model at start-up phase.

For the prediction of ohmic discharge for VEST-upgrade, validation with comparison between the model and experimental data should be necessary. In the validation step, several plasma parameters such as plasma current and electron temperature & density and filterscope data are utilized for the comparison.

The plasma current evolution is one of the important parameters in the model result, which is obtained by the circuit equation. For a reliable result, exact modelling for circuit parameters is required. Several start-up models in previous studies has a limitation for exact calculation of loop voltage as driving source of plasma current. For exact calculation of loop voltage, an electromagnetic analysis which considers a central solenoid, PF coils and vacuum vessel is required. In this research, electromagnetic model is developed and it is validated by utilizing the experimental flux loop data in VEST. Other factors to determine the plasma current evolution are the plasma inductance and resistance. It is found that external inductance with large aspect ratio assumption is invalid to ST plasmas. Therefore, new external inductance for VEST is developed based on the Hirshman model. Also, in STs, effective plasma resistance can be larger than one calculated by classical spitzer model due to the larger trapped particle fraction, called the neoclassical effect. In order to consider this effect, the analytic model derived by O. Sauter is introduced. For exact calculation of neoclassical factor, simulation result by NCLASS which calculates the neoclassical transport is utilized. In the case of confinement model, the previous model with convective transport losses is utilized. The confinement model utilized in the start-up model is confirmed by comparison between the model and experiment in VEST. Main impurity source is set to be carbon. The proper coefficient related to the plasma wall interaction is found with parameter scan simulation and it is utilized in validation and prediction at chapter 4.

Validation of the start-up model is conducted in order to confirm the validity of the model in VEST. Ohmic discharges in VEST is divided into three: (1) central solenoid coil current, (2) outer PF coil current and (3) wall conditions. The star-up model can reproduce the ohmic discharges under the above operational conditions with reasonable level. However, there are discrepancies between the model and experiment. For example, it is observed that electron temperature increases during the plasma current ramp-down phase

which is thought to be caused by the compressional heating. It is limitation to reproduce this feature by using the present start-up model. Therefore, improvements of the model are needed for better reproduction of experiments in VEST. After the validation, the model is utilized for prediction of ohmic discharges in VEST. According to the prediction result, similar current evolution with the target plasma can be achieved with slow ramp-down of the CS current waveform from 20 kA to -20 kA during 50 ms. However, the wall condition with low hydrogen retention wall is required for the target plasma current. In other words, it is difficult to achieve the target plasma current with present wall conditions after the boronization due to the significant hydrogen retention. Therefore, improvements in wall conditioning methods should be required. The model is utilized for mid-and huge size ST devices, MAST and STEP. The start-up model well reproduces a ohmic discharge conducted in MAST. Also, predictive burn-through simulation is conducted for prediction in STEP which is a huge fusion project on design step in the UK.

In this research, new start-up model based on the 0D burn-through simulator is developed for prediction of ohmic discharges in VEST and it is validated in VEST by reproducing the experimental data. After the validation, the model is utilized in prediction of ohmic discharge of VEST. It is confirmed that the model can be utilized regardless of machine specification by the simulation results in MAST and STEP. Even though the start-up model is applied in conventional ohmic discharge in this research, it is expected that the model is utilized for alternative start-up method such as outer PF coil start-up or double plasma merging start-up methods.

Keywords: Tokamak start-up, burn-through, Tokamak start-up model, electromagnetic analysis, spherical torus, VEST.

Student Number: 2014-22716

Table of Contents

Abstract	i
Table of Contents	iv
List of Figures	vii
Chapter 1. Introduction	1
1.1. Nuclear Fusion and Tokamaks	1
1.2. Tokamak start-up and its modelling	4
1.3. Motivation.....	7
1.4. Previous works.....	11
1.5. Objectives of this research.....	16
Chapter 2. Compact ST device, VEST	17
2.1. Ohmic discharge.....	17
2.2. Equilibrium reconstruction	21
2.2.1. External magnetic diagnostics and wall modelling	22
2.2.2. Procedure of equilibrium reconstruction.....	28
2.3. Validation diagnostics.....	33
2.3.1. Thomson scattering.....	34
2.3.2. Filterscope system	37
Chapter 3. Development of Full Electromagnetic Start-up Model in VEST	39
3.1. Full electromagnetic model	39
3.1.1. Full circuit equation	40
3.1.2. Plasma circuit model.....	48
3.2. Plasma volume model with Townsend criterion	56
3.3. Confinement model	62
3.4. Plasma wall interaction model	65

Chapter 4. Model Validation and Prediction of Ohmic Discharges in Spherical Torus Devices	67
4.1. Identification of burn-through regime in VEST	68
4.1.1. Experimental operation window in E -field and prefill pressure.....	68
4.1.2. Reproduction of burn-through region using the start-up model	72
4.2. Time evolution of plasma parameters in ohmic discharges with different operational conditions	75
4.2.1. Ohmic discharges with different central solenoid currents	76
4.2.2. Ohmic discharges with different outer PF coil currents.....	82
4.2.3. Ohmic discharges with different wall conditioning methods	92
4.3. Prediction of ohmic discharges for VEST-Upgrade.....	98
4.4. Validation in MAST and prediction in STEP.....	102
Chapter 5. Conclusions	108
5.1. Summary and conclusions	108
5.2. Future works	110
5.2.1. Preliminary result of small ST formation using the start-up model.....	110
5.2.2. Future works.....	113
Bibliography	114
국문초록	118

List of Tables

Table 1.1 Previous studies for tokamak start-up modelling.....	13
Table 3.1 Original and modified fitting coefficients for external inductance model.....	49

List of Figures

Figure 1.1 Cross-section for fusion. Taken from figure 1.2.2 [1]	2
Figure 1.2 Basic characteristic of tokamak geometry. Taken from figure 120 [2].....	3
Figure 1.3 Minimum electric field for Townsend avalanche breakdown in several tokamak devices and experiment data points. Taken from figure 12 [7].....	6
Figure 1.4 Time evolution in (a) the plasma current and loop voltage at machine center and (b) vacuum vessel eddy current in each element and total vacuum eddy current.	9
Figure 1.5 Neutral pressure measurements during the ohmic discharge in VEST [11].....	10
Figure 1.6 Comparison of DYON simulation results and JET experiments with the C wall (#77210) and the Be wall (#82003). Taken from figure 6 of [13].....	14
Figure 1.7 (a) Comparison of BKD0 output with the experimental data for shot 38378 and shot 38376. (b) Operational window in terms of electric field and neutral pressure for different cases and configurations. Taken from figure 12 and 13 of [15]..	15
Figure 2.1 Picture of VEST device and specification of VEST operation in present and future.....	17
Figure 2.2 Schematic of a poloidal plane in VEST.....	19
Figure 2.3 EC-assisted ohmic discharge procedure in VEST: evolution of (a) Toroidal field coil current (b) prefill neutral pressure (c) ECH injected power (d) PF01 coil current (e) PF05 coil current (f) PF06 and PF09-10 coil current and (g) plasma current.....	20
Figure 2.4 Location of the external magnetic diagnostics sensors with poloidal plane view and digitization scheme of external magnetics signals.....	24
Figure 2.5 Comparison of inboard and outboard magnetic field between experiment and electromagnetic models: Experiment and electromagnetic model.	25
Figure 2.6 Comparison of side magnetic field and flux loops between experiment and electromagnetic models: Experiment and electromagnetic model	26
Figure 2.7 Comparison of side magnetic field and flux loops between experiment and electromagnetic models: Experiment and electromagnetic model	27
Figure 2.8 Equilibrium fitting result with the shape reconstruction in the shot#37440: (a) magnetic signals, (b) element distribution in 8 by 5 rectangular grids and (c) magnetic fitting error between measurements and reconstruction.	30
Figure 2.9 Time evolution in plasma current, plasma shape and 2D poloidal magnetic flux distribution from the shape reconstruction in the shot#37440	31
Figure 2.10 (a) Time evolution of plasma current, plasma shape and global MHD parameters, (b) Magnetic fitting error between measurements and reconstruction, and (c) Time evolution of 2D poloidal magnetic flux distribution from the EFIT-like reconstruction in the shot#37440.	32

Figure 2.11 Thomson scattering system in VEST	35
Figure 2.12 Process for obtaining the volume averaged electron temperature and density: (Left) Equilibrium flux surface and Thomson scattering measurement positions, (Middle) Mapping into the flux surface dimension and interpolation, (Right) Conversion to real dimension and volume averaging	36
Figure 2.13 Filterscope system in VEST	38
Figure 3.1 Full circuit system: blue box (PF coils – known parameters) and yellow box (vacuum vessel and plasma current – unknown parameters)	43
Figure 3.2 (a) Input VEST structure and vacuum vessel (b) and PF coils (c) element table	45
Figure 3.3 (Left) Input PF coil current waveforms for full EM model in the vacuum magnetic field calculation and (Right) flux loops data from full EM model and experimental measurements	46
Figure 3.4 (Left) Input plasma and PF coil current waveforms for full EM model in the magnetic field calculation (Right) flux loops data from full EM model and experimental measurements	47
Figure 3.5 Comparison of plasma external self-inductance value between the large aspect ratio and the Hirshman models with aspect ratio	53
Figure 3.6 Comparison of normalized analytic and exact external self-inductance (reconstruction) values for the Hirshman, new modified and large aspect ratio models	53
Figure 3.7 Time evolution in the plasma current and the normalized internal inductance from the equilibrium reconstruction (a: initial assumption, b: equilibrium reconstruction, and c: interpolation) in the shot#37440	54
Figure 3.8 Neoclassical enhancement factor	54
Figure 3.9 Time evolution in (a) the plasma current and H_{α} line emission signal and (b) the plasma volume structure calculated by the Townsend volume model in the shot#37440	55
Figure 3.10 (a) Evolution of two-dimensional electromagnetic field using full electromagnetic model (from left to right: 290 – 310 ms). (a) poloidal magnetic flux (b) radial magnetic field (c) vertical magnetic field (d) toroidal loop voltage (e) toroidal electric field	60
Figure 3.11 Evolution of 2D plasma volume with two methods: finite element method and single filament method.....	61
Figure 3.12 Time evolution in (a) the energy confinement time from the experiment and model and (b) the ratio of the ohmic heating power and power losses from the model.....	64
Figure 3.13 Time evolution in (a) the plasma current from the experiment and model, (b) the electron temperature from the experiment and model and (c) the electron density from the experiment and model.....	66
Figure 4.1. Time evolution in the plasma current and filterscope signals (H_{α} , OII and CIII) at the burn-	

through success (up) and fail (down) cases.....	70
Figure 4.2 Scattered points representing the burn-through success, fail and the plasma breakdown fail with the Townsend breakdown curve in electric field and prefill pressure space.....	71
Figure 4.3 Burn-through line obtained by the model with Fig.4.2.....	73
Figure 4.4 Base pressure and partial pressure of water measured by Residual Gas Analyzer (RGA).	74
Figure 4.5 Operational conditions in the shot#37970 and 37919: (a) PF coil current waveforms, (b) loop voltage and equilibrium field at machine center, and (c) neutral pressure evolutions	78
Figure 4.6 Features of ohmic discharges in the shot#37970 and 37919: (a) plasma current and filterscope signals ($H\alpha$, OII and CIII), electron temperature and density evolutions (b) in the shot#37970 and (c) in the shot#37919	79
Figure 4.7 Time evolution in (from up to down): plasma current, electron temperature, electron, electron density, $H\alpha$ line emission signal and CIII line emission signal from the model and experiment in the shot#37919	80
Figure 4.8 Time evolution in (from up to down): plasma current, electron temperature, electron, electron density, $H\alpha$ line emission signal and CIII line emission signal from the model and experiment in the shot#37970.....	81
Figure 4.9 Operational conditions in the shot#37440, 37441 and 37442: (a) PF coil current waveforms, (b) loop voltage and equilibrium field at machine center, and (c) neutral pressure evolutions.	85
Figure 4.10 Features of ohmic discharges in the shot#37440, 37441 and 37442: (a) plasma current and filterscope signals ($H\alpha$, OII and CIII), electron temperature and density evolutions (b) in the shot#37440, (c) in the shot#37441 and (d) in the shot#37442.....	86
Figure 4.11 Evolution in (a) plasma current, (b) major radius, (c) lower limiter current, (d) mid-limiter current, and (e) upper limiter current in the shot#37440, 37441, and 37442.	87
Figure 4.12 CIII filtered fast camera images in the shot#37440, 37441, and 37442	88
Figure 4.13 Time evolution in (from up to down): plasma current, electron temperature, electron, electron density, $H\alpha$ line emission signal and CIII line emission signal from the model and experiment in the shot#37440.....	89
Figure 4.14 Time evolution in (from up to down): plasma current, electron temperature, electron, electron density, $H\alpha$ line emission signal and CIII line emission signal from the model and experiment in the shot#37441	90
Figure 4.15 Time evolution in (from up to down): plasma current, electron temperature, electron, electron density, $H\alpha$ line emission signal and CIII line emission signal from the model	

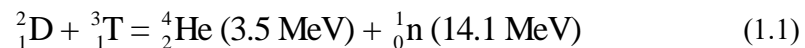
and experiment in the shot#37442	91
Figure 4.16 Operational conditions in the shot#37906 and 37866: (a) PF coil current waveforms, (b) loop voltage and equilibrium field at machine center, and (c) neutral pressure evolutions	94
Figure 4.17 Features of ohmic discharges in the shot#37906 and 37866: (a) plasma current and filterscope signals ($H\alpha$, OII and CIII), electron temperature and density evolutions (b) in the shot#37911 and (c) in the shot#37869	95
Figure 4.18 Time evolution in (from up to down): plasma current, electron temperature, electron, electron density, $H\alpha$ line emission signal and CIII line emission signal from the model and experiment in the shot#37906	96
Figure 4.19 Time evolution in (from up to down): plasma current, electron temperature, electron, electron density, $H\alpha$ line emission signal and CIII line emission signal from the model and experiment in the shot#37866.....	97
Figure 4.20 Prediction of evolution parameters in two cases: central solenoid current, loop voltage at plasma center, plasma current, electron temperature, electron density and $H\alpha$ line emission signal from up to down.	100
Figure 4.21 Prediction of evolution parameters in two cases: central solenoid current, loop voltage at plasma center, plasma current, electron temperature, electron density and $H\alpha$ line emission signal from up to down	101
Figure 4.22 Schematic of central solenoid and PF coils in MAST. Taken from figure 2 of [17]	104
Figure 4.23 (a) Input coil current waveforms utilized in the start-up model, (b) vacuum vessel eddy current, (c) plasma volume, (d) plasma self-inductance, (e) plasma resistance, and (f) plasma current evolution in MAST simulation. Taken from figure 3 of [17]	105
Figure 4.24 Evolution of plasma volume and poloidal magnetic flux map simulated in the start-up model during the plasma breakdown and burn-through phases. Taken from figure 4 of [17]..	106
Figure 4.25 Simulation results in STEP: vacuum poloidal magnetic flux map, PF coil currents, vacuum vessel eddy current, plasma current, loop voltage, plasma volume, plasma temperature and plasma density evolutions. Taken from page 21 of [50]	107
Figure 5.1 Partial solenoid coil current and loop voltage evolution in the shot#38243.....	111
Figure 5.2 Time evolution in the plasma current, electron temperature, electron density and $H\alpha$ line emission signal from the model (shot#37243: experimentally fail case)	112

Chapter 1. Introduction

1.1. Nuclear Fusion and Tokamaks

Realization of clear and renewable energy source is an urgent issue due to the growth of energy demand in the world-wide. New energy sources should have unlimited resource and not destroy the environment. Nuclear energy released by the fusion reaction is an energy source which meets these requirements. Therefore, nuclear fusion is one of the strong candidates for the future energy source.

Huge amount of energy can be generated by fusing two light nuclei into a heavy nucleus with higher binding energy (alpha particle). The most probable fusion reaction is between deuterium and tritium (D-T reaction) [1] by following reaction:



When a deuterium ion and a tritium ion collide with sufficient energy for fusion reaction, an alpha particle and a neutron are generated with energy of 3.5 MeV and 14.1 MeV, respectively. Figure 1.1 shows the cross-section for three different fusion reactions. For fusion reaction, at least above 10 keV energy is required for all cases. Importantly, many fusion reactions are needed to utilize the nuclear fusion as an energy source. For this, fully ionized gas state with high temperature and density is necessary and it is called the plasma. DT fusion reaction is relatively easy to be achieved due to its higher cross-section at lower deuterium ion energy. Nevertheless, it is difficult to maintain the extremely high temperature with dense fuel density. Also, on earth it is impossible to maintain fusion reactions with strong gravity like the sun. Various fusion device concepts have been suggested for the fusion energy research, but the most promising concept for the nuclear fusion is a Tokamak device.

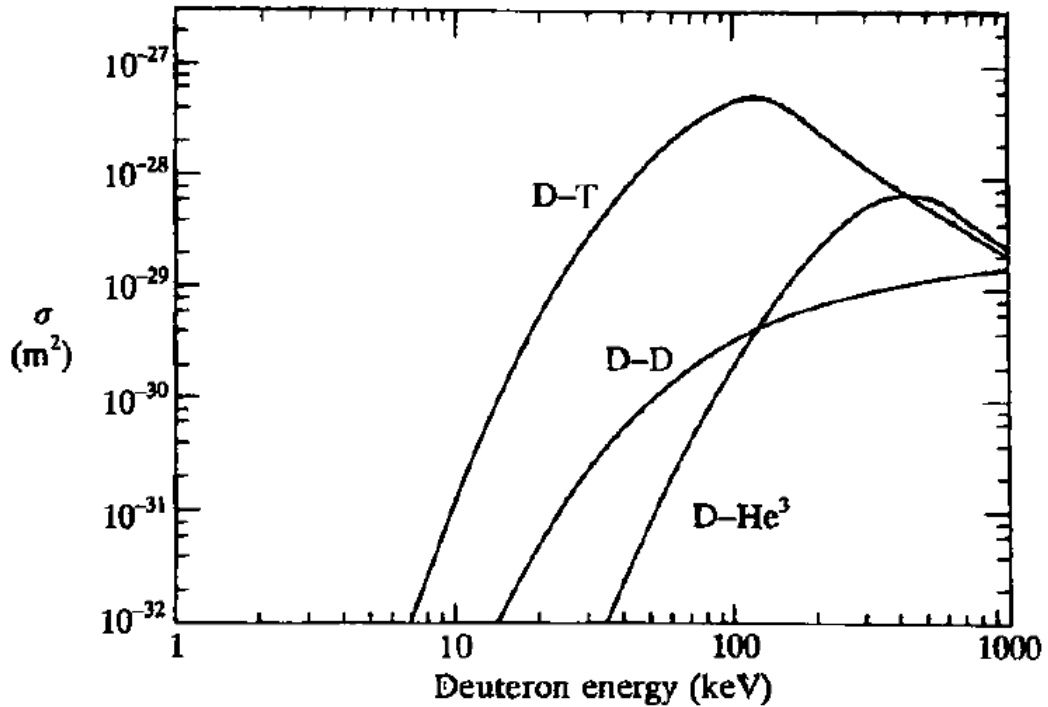


Figure 1.1 Cross-section for fusion reactions. Taken from figure1.2.2 [1].

Tokamak confines a high temperature and density plasma in a shape of torus utilizing the complicated magnetic field which electrons and ions orbit around the magnetic field line. This complicated magnetic field line that move around the torus is necessary to confine a plasma in a stable equilibrium, which can be formed by toroidal and poloidal magnetic fields. The toroidal magnetic field can be generated by wrapping a series of coil around the toroidally continuous vacuum vessel. This configuration makes I/R dependency on the toroidal magnetic field strength according to the Ampere's law. The I/R dependency leads drift motions by ∇B and magnetic curvature. In a pure toroidal magnetic field, the ions and electrons are separated by the drift motion and it generates an electric field. Consequently, the combination of electric field and magnetic field makes an $E \times B$ drift resulting in complete loss of the charged particles. One solution to tackle this

problem is to utilize the poloidal magnetic field and tokamak is a concept which utilize the poloidal magnetic field by generation of plasma current. Fig. 1.2 shows a schematic cross-section of tokamak depicting key components; toroidal field coil, poloidal field coil and plasma current. An external poloidal field coil provides an equilibrium magnetic field (or vertical magnetic field) to satisfy the radial force balance as the plasma tends to move outward. By using the sets of poloidal field coils, plasma shape parameters such as major radius, minor radius, elongation and triangularity are controlled.

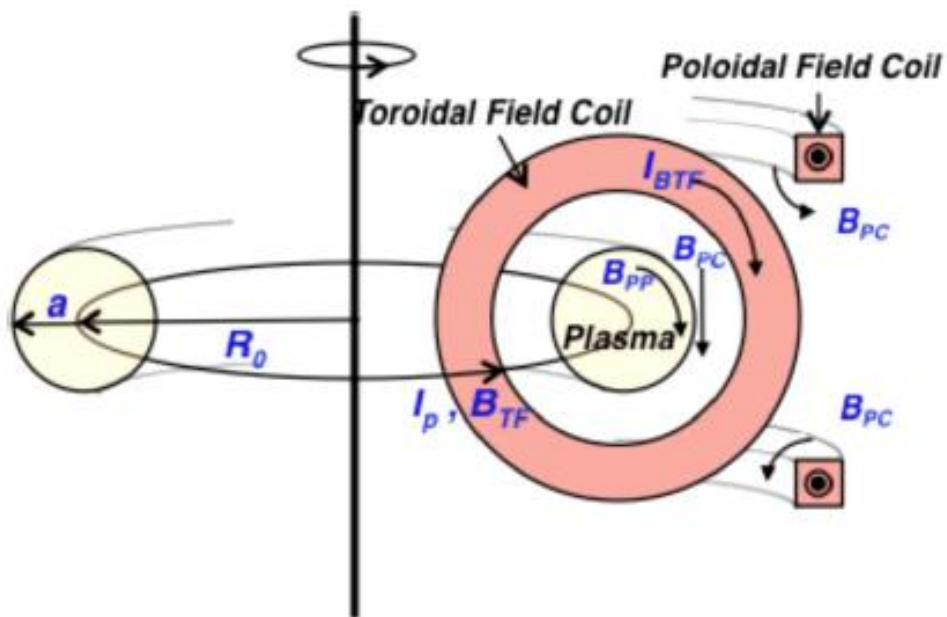


Figure 1.2 Basic characteristic of tokamak geometry. Taken from figure 120 [2].

1.2. Tokamak start-up and its modelling

The tokamak start-up is divided into three phases: plasma breakdown, burn-through and current ramp-up. The plasma breakdown can be described by the Townsend avalanche theory which is originally used to describe DC breakdown. In the conventional ohmic discharge of tokamak, toroidal electric field is induced by the central solenoid coil swing. Due to the similarities of plasma breakdown in tokamak and DC breakdown, it is utilized for tokamak breakdown phase [3-6]. According to the Townsend theory with the α process, the minimum electric field for breakdown can be represented by a function as neutral pressure and connection length. The connection length is defined as the distance that the electrons travel along the magnetic field line till they hit the vacuum vessel wall. The Townsend minimum electric field for breakdown is expressed as following:

$$E_{min} (V/m) = \frac{1.25 \times 10^4 p(Torr)}{\ln(510 p(Torr) L_f(m))} \quad (1.2)$$

where p is neutral pressure and L_f is a connection length. Fig. 1.3 shows a Townsend breakdown curve in several tokamak devices [7]. Recently, it is reported that Townsend theory has a limitation to explain the tokamak breakdown phase due to self-generated electric field by plasma. In the research, tokamak breakdown in KSTAR device is analyzed by using the particle-in-cell (PIC) simulation which considers the self-generated electric field by plasma [8, 9].

After the successful plasma breakdown in tokamak, electrons generated during the breakdown phase are continuously accelerated by induced toroidal electric field and ionize the prefilled hydrogen (or deuterium) neutrals. This process with fully ionization of injected fuels is the ‘burn-through’. In the burn-through process, not only the hydrogen fuels but also low- Z impurities such as carbon and oxygen are ionized. For successful burn-through, ohmic heating power need to exceed the sum of ionization and radiation power losses. With failure in plasma burn-through, plasma current cannot ramp up due to

its high spitzer resistance with the relation of electron temperature, $\eta_{sptz} \propto T_e^{-3/2}$. After the successful burn-through, plasma current can rise with ohmic heating.

The tokamak start-up is very dynamic phase in which plasma parameters significantly vary. So, it is very difficult to control plasma parameters experimentally in this phase with the real-time feedback control. Typically, an approach with the feedforward control is utilized for a successful start-up in all devices at this phase. It is necessary to establish a predictive model for the tokamak start-up with given operational conditions such as PF coil currents, prefill pressure and wall conditions and so on. Tokamak start-up model can provide a proper operational scenario for the successful tokamak start-up. If a reliable tokamak start-up model is developed, it can significantly reduce trial an error in experiments. The tokamak start-up model can be utilized not only to look for the operational recipes for the successful start-up but also to provide several design parameters such as vacuum vessel, central solenoid and PF coil structure for construction of new tokamak machine. For example, electromagnetic effect from the PF coil and vacuum vessel current is significant in the start-up phase. It is important to estimate several electromagnetic parameters exactly such as loop voltage and poloidal magnetic field which are main parameters to determine the burn-through success or fail.

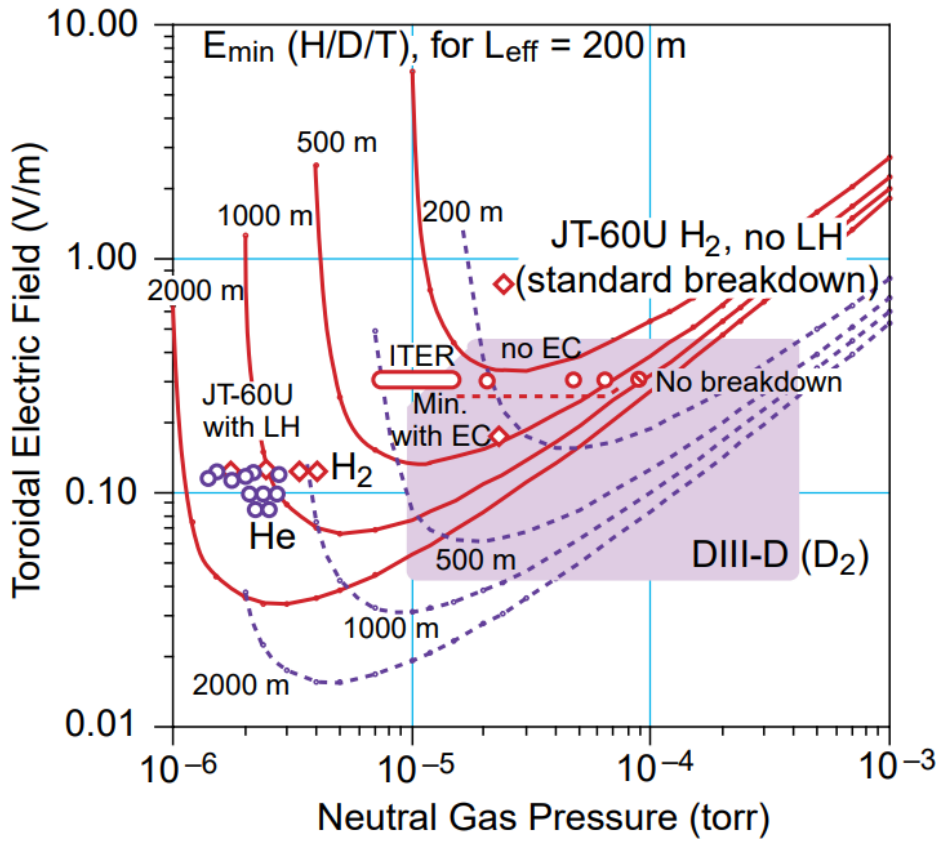


Figure 1.3 Minimum electric field for Townsend avalanche breakdown in several tokamak devices and experiment data points. Taken from figure 12 [7].

1.3. Motivation

Versatile Experiment Spherical Torus (VEST) is a compact ST device which has been operated at Seoul National University in Korea [10]. Improvements in plasma performance such as plasma current and plasma beta are required for advanced tokamak studies and it is prepared for upgrade of VEST device. Mainly, power control systems for the central solenoid and PF coils are upgraded for higher ohmic power and plasma shape control. With the upgraded coil power systems, a new plasma current evolution which has a maximum plasma current with ~ 10 MA/s ramp-up rate and a flat-top phase during ~ 20 ms with the maximum plasma current is targeted. A predictive start-up modelling is necessary to achieve the target plasma current with the operational limitation of the central solenoid and PF coil systems.

Typically, there is a limitation for utilization of the start-up model in the start-up phase. Effects by electromagnetic and atomic physics such as ionization, radiation and charge exchange are dominant in the start-up phase. When the plasma current grows to some extent after the burn-through phase, the transport effect becomes dominant than effects by electromagnetic and atomic physics. Therefore, the start-up model is utilized to simulate the burn-through phase and partial current rise phase in medium or huge tokamak devices. However, features of ohmic discharge in VEST is different from medium or huge tokamak devices. Firstly, the electromagnetic effect from the PF coil and vacuum vessel is dominant during the whole discharge in VEST. Fig.1.4 shows time evolutions in the plasma current, loop voltage and vacuum vessel eddy currents. The loop voltage affects plasma evolution and significant vacuum vessel eddy currents flow during the whole discharge. In addition to the electromagnetic effect, atomic physics are dominant even after the burn-through phase. Fig.1.5 shows time evolutions in the plasma current and neutral pressure in typical VEST ohmic discharge. It is observed that the increase of neutral pressure is measured by a fast penning ion gauge installed in VEST [11]. It

indicates that significant neutrals are released from the wall due to the interactions between the plasma and wall. In other words, features of the start-up phase are observed in whole ohmic discharge of VEST. The start-up model can be applied to the plasma breakdown and burn-through phases as well as the whole current rise phase in VEST.

Electromagnetic analysis is important in terms of prediction of target plasma current evolution. Main driving source for plasma current is a loop voltage induced by central solenoid, PF coils and vacuum vessel eddy currents. For exact estimation of loop voltage, configuration of complicated coil and vacuum vessel should be considered. In this research, the full electromagnetic analysis with consideration of PF coils and vacuum vessel is developed for exact estimation of loop voltage as driving source which generates the plasma current. Also, a model for neutral particles should be considered. In the early start-up phase (i.e. the plasma breakdown and the burn-through phases), the effect of neutral particles is mainly due to the prefilled hydrogen fuel and initial impurities. After the early start-up phase, the effect of neutral particle is dominated mainly by the plasma wall interactions. Several factors which can affect the plasma wall interactions should be considered: What is impurity species, where are impurity sources in the vacuum vessel, and when does plasma touch the impurity sources. In the chapter 3.4, the plasma wall interaction model is described.

Even though the start-up modelling in this research starts with motivation for the prediction of new ohmic discharge in VEST, the start-up model can be utilized as burn-through simulation for the optimization of operational scenario or design of tokamak machine in huge devices such as ITER and STEP. In this research, utilization of the start-up model for burn-through simulation in STEP is shortly described in the chapter 4.4.

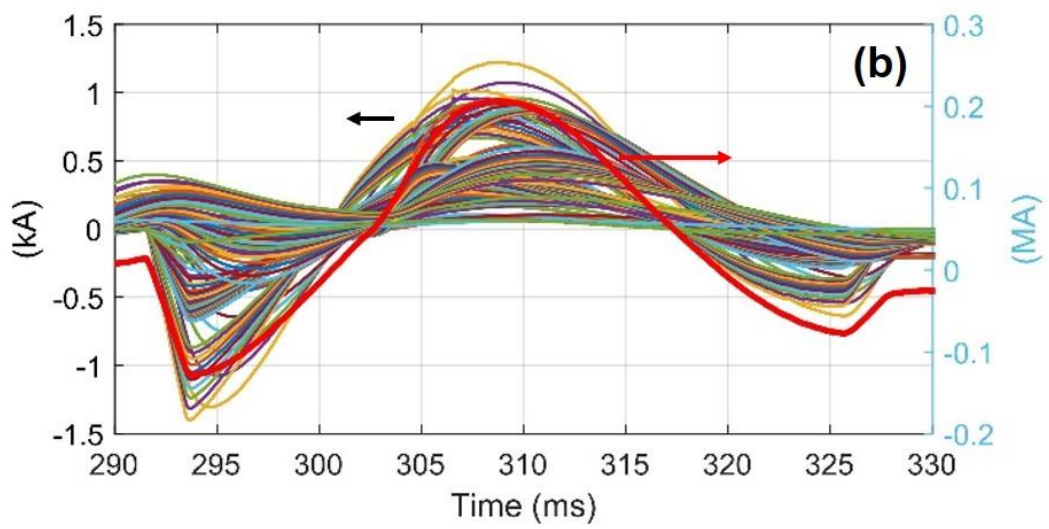
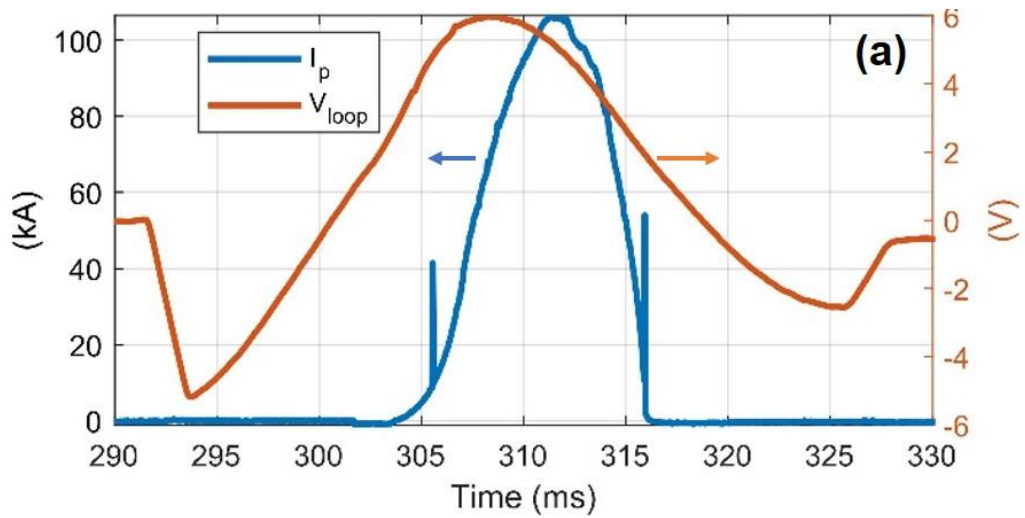


Figure 1.4 Time evolution in (a) the plasma current and loop voltage at machine center and (b) vacuum vessel eddy current in each element and total vacuum eddy current.

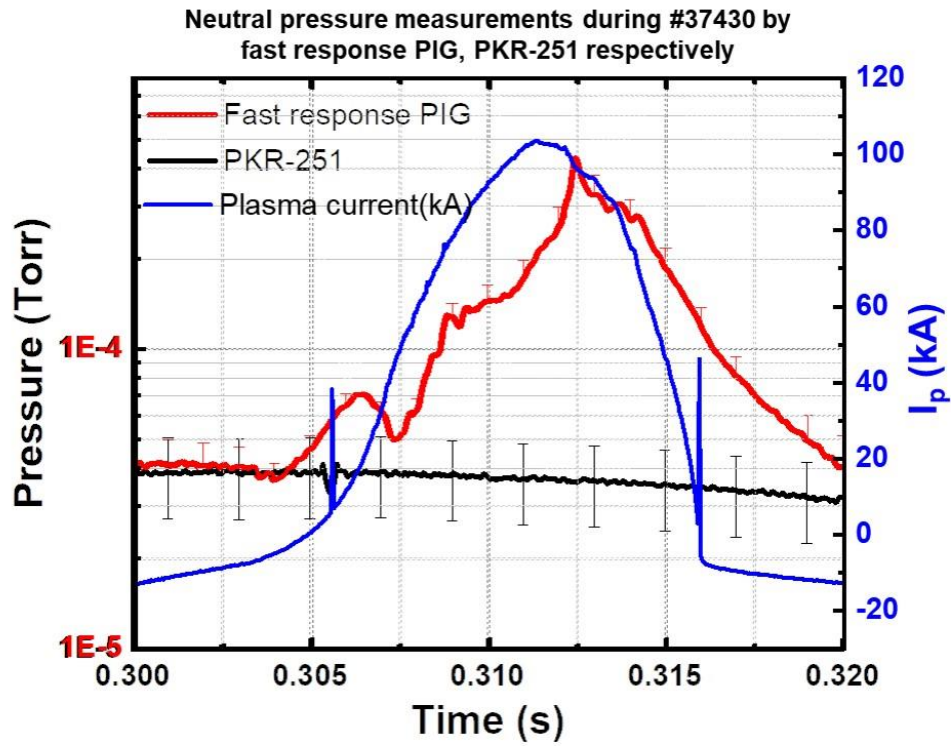


Figure 1.5 Neutral pressure measurements during the ohmic discharge in VEST: Red line (penning gauge measurement), black line (commercial gauge measurement) and blue line (plasma current) [11].

1.4. Previous works

In this section, previous studies for start-up modelling are described. Table 1.1 shows a short description of previous studies for start-up modelling in terms of circuit model, plasma wall interaction model and confinement model. In the B Lloyd paper [5], burn-through simulation in ITER is conducted with a 0D based model which consists of energy & particle balances and single circuit equation. From the energy & particle balances, time evolution in electron's and ion's temperature & density are obtained. The plasma current evolution is calculated by an electric circuit equation. In this 0D burn-through model, impurity density is simply assumed to be constant ratio to the main deuterium ion density and INTOR scaling law is utilized for confinement model.

Second example is a DYON code with 0D burn-through model developed by Hyun-Tae Kim [12-14]. Basic structure of DYON code is similar as the model in B Lloyd's modelling. In the DYON code, ion's and neutral's particle balance with various species such as carbon, oxygen, nitrogen and beryllium are established. Two circuit equations are utilized to consider a passive structure in JET. Different confinement model is utilized at open field and closed field phases. Detailed confinement model in DYON code is described in the chapter 3.3. DYON code is validated in JET ohmic discharges and Fig.1.6 shows comparison of DYON simulation results and JET experiments with the C wall and the Be wall [13]. It is showed that DYON code well reproduce the experimental results with different two wall.

BKD0 is one of main stream burn-through model with DYON code. BKD0 has similar model structure as DYON code. In the paper with BKD0 [15], BKD0 linked to a beam tracing code computing for EC absorption is validated and utilized to determine the operation window of sustained breakdown as a function of toroidal electric field and neutral pressure as shown in Fig.1.7. The overall evolution in the plasma current and density well reproduced. Also, it shows the agreement between simulations and

experimental results in 2D operational window.

0D models as mentioned above such as DYON and BKD0 utilize experimental loop voltage waveform measured by flux loop for model input in circuit equation. Even though each model reproduces the experimental results with reasonable level, the use of experimentally measured loop voltage such as flux loop data in specific position is improper. Also, it is difficult to apply the model to other devices with this approach. Rather than the use of experimental data, exact estimation of loop voltage at plasma center position is required for a reliable plasma current evolution.

There is a new model with full electromagnetic analysis for direct induction start-up scenario development on MAST-U and NSTX-U [16]. In this study, the electromagnetic code called the LRDFIT calculates a time-dependent vacuum field with consideration of PF coils and vacuum vessel structure. Therefore, it is possible to estimate exact loop voltage and magnetic field in the start-up phase. However, the overall start-up model is based on the experimental results in MAST and NSTX. In other words, temperature and density evolution cannot be obtained like other start-up models. It is difficult to apply this model to other devices due to the lower predictive capability.

Recently, a full electromagnetic model with DYON code is developed and validated on MAST ohmic discharges [17]. Several model such as full electromagnetic circuit model and Townsend volume model described in the paper are included in this dissertation. Detailed descriptions of the full electromagnetic start-up model are described in the chapter 3.

Previous studies	Features
B Lloyd., et al., NF, 1996. 38 (1627-1643) [5]	<ul style="list-style-type: none"> ● 0D burn-through code with energy & particle balances and single circuit equation ● Constant impurity density ratio to main ion density ● INTOR scaling for confinement model ● Simulation of ITER burn-through
<p><u>DYON code</u></p> <p>Hyun-Tae Kim., et al., NF, 2012. 52 (103016) [12]</p> <p>Hyun-Tae Kim., et al., PPCF, 2013. 55 (124032) [13]</p> <p>Hyun-Tae Kim., et al., JNM, 2013. 438 (S1271-S1274) [14]</p>	<ul style="list-style-type: none"> ● 0D burn-through code with energy & particle balances and two ring circuit equations with passive structure in vacuum vessel ● Plasma wall interaction model with wall sputtering yield in various species ● Confinement model with convective transport loss & different form in open field and closed field regime ● Validation in JET Ohmic discharges & simulation of ITER burn-through
<p><u>BK0D code</u></p> <p>G. Granucci., et al., NF, 2015. 55 (093025) [15]</p>	<ul style="list-style-type: none"> ● 0D burn-through code with energy & particle balances and single circuit equation ● Confinement model with convective transport loss ● Simulation of FTU tokamak burn-through
<p><u>Full EM empirical code</u></p> <p>D. J. Battaglia., et al., NF, 2019. 59 (126016) [16]</p>	<ul style="list-style-type: none"> ● Full electromagnetic circuit model ● No other physics model such as energy & particle balances ● Empirical model with based on experimental database ● Start-up scenario check in MAST-U & NSTX-U
<p><u>Full EM code with DYON</u></p> <p>Hyun-Tae Kim...Seongcheol Kim., et al., NF, 2022. 62 (126012) [17]</p>	<ul style="list-style-type: none"> ● Full electromagnetic & Townsend volume model + DYON code ● Validation in MAST Ohmic discharge

Table 1.1 Previous studies for tokamak start-up modelling.

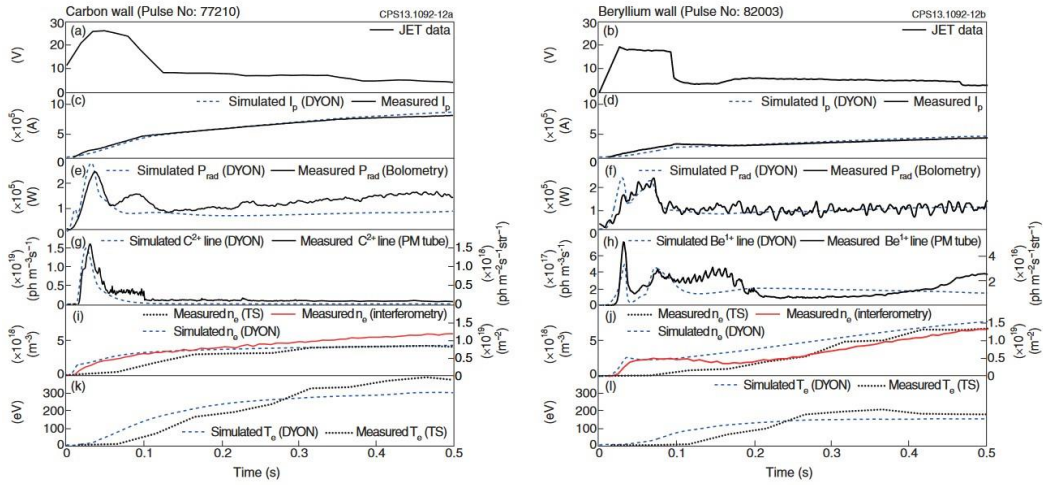


Figure 1.6 Comparison of DYON simulation results and JET experiments with the C wall (#77210) and the Be wall (#82003). Taken from figure 6 of [13].

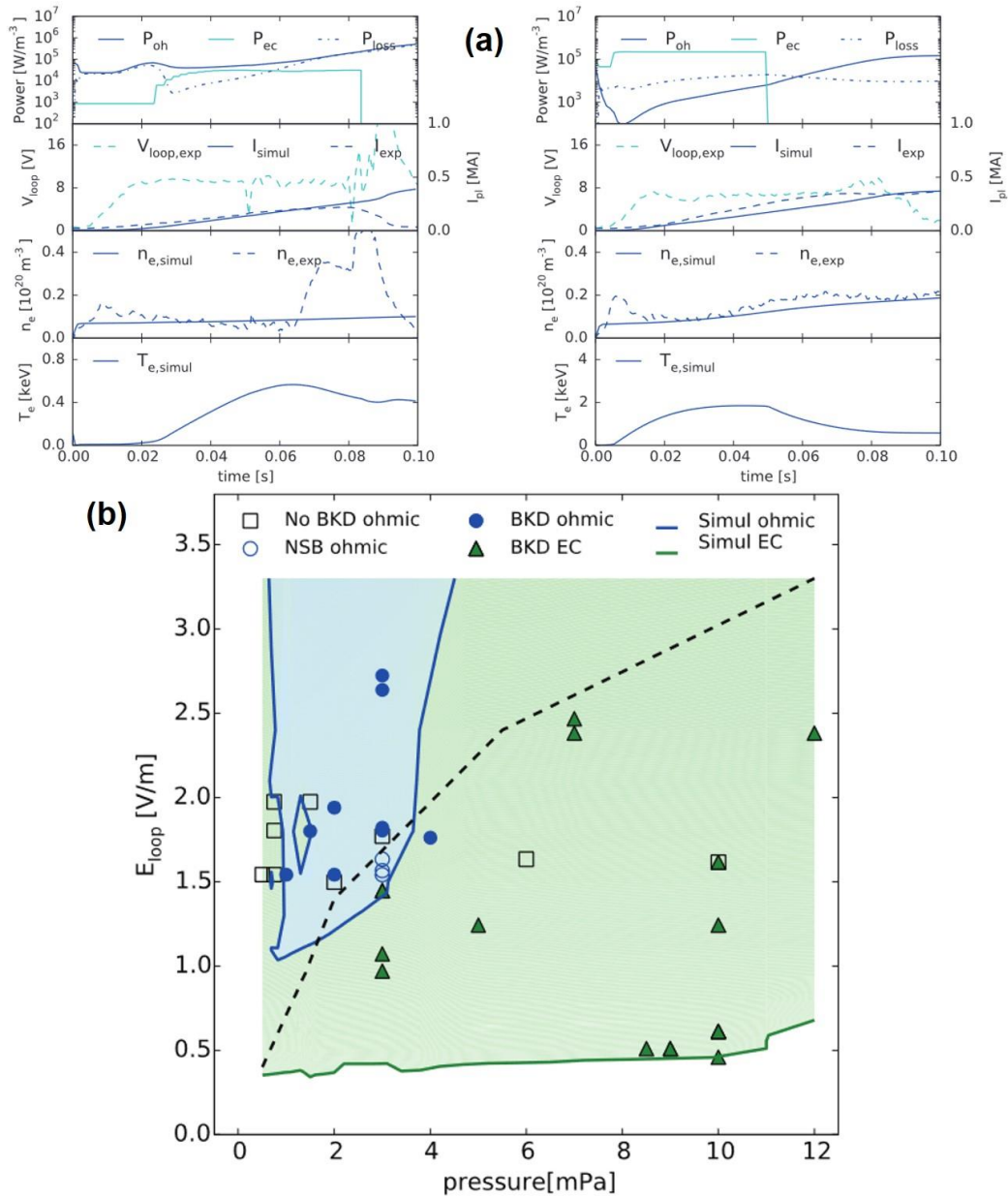


Figure 1.7 (a) Comparison of BKD0 output with the experimental data for shot 38378 and shot 38376. (b) Operational window in terms of electric field and neutral pressure for different cases and configurations. Taken from figure 12 and 13 of [15].


1.5. Objectives of this research

Main objective of this research is to develop a reliable start-up model for achievement of 300 kA target plasma current in VEST. In this research, previous DYON code [12-14] is utilized for power and particle balance model because sub-models such as atomic physics model and confinement model are well-established than other models. For its applicability in VEST, the new start-up model is validated on ohmic discharges with different operational conditions. After the validation in VEST, predictive simulations using the start-up model are conducted for achievement of 300 kA target plasma current in VEST. In order to suggest that this model can be utilized not only in a compact device, VEST, but also other devices, it is showed a validation on MAST [17] and a prediction on STEP.

Chapter 2. Compact ST device, VEST

2.1. Ohmic discharge

VEST (Versatile Experiment Spherical Torus) is a compact spherical torus which has been operated at Seoul National University in Korea [10]. It has been constructed for studying the innovative start-up, non-inductive current drive, and disruption research. Fig. 2.1 shows a picture of VEST device and specification of VEST in present and future. Toroidal field is operated between 0.1 – 0.18 T at machine center. Major and minor radius is about 0.43 m and 0.33 m, respectively. Plasma elongation is operated about 2. Maximum plasma current is about 170 kA in present state. There are several heating and current drive sources: electron cyclotron heating (8 GHz – 3 kW and 2.45 GHz – 6 kW) [18], neutral beam injection (15 keV – 600 kW) [19-21] and lower hybrid fast wave (500 MHz – 10 kW) [22, 23]. In this section, ohmic discharge [24] and validation diagnostic systems for plasma start-up model are described.



	Present	Future
Toroidal B Field	0.1 – 0.18 T	0.1 – 0.18 T
Major Radius	0.43 m	0.43 m
Minor Radius	0.33 m	0.33 m
Aspect Ratio	> 1.33	> 1.33
Plasma Current	< 170 kA	< 300 kA
H & CD (ECH, NBI, LHFW)	ECH (7.9GHz, 3kW) ECH (2.45GHz, 15kW) NBI (15keV, 600kW) LHFW (500MHz, 10kW)	ECH (7.9GHz, 3kW) ECH (2.45GHz, 30kW) NBI (20keV, 1.2MW) LHFW (500MHz, 200kW)

Figure 2.1 Picture of VEST device and specification of VEST operation in present and future.

The TF coil in VEST consists of 24-turn around the vacuum vessel and is powered by an ultra-capacitor bank. It typically carries 200 – 360 kAt total current to generate the toroidal magnetic field of 0.1 – 0.18 T on the machine center (~0.4 m). The schematic of a poloidal plane in VEST is shown in Fig. 2.2, where the poloidal field (PF) coils, vacuum

vessel and the piezoelectric valve (PEV) for the prefill gas injection are marked. An ohmic discharge starts with the toroidal field ramping-up. The toroidal magnetic field flat-top is maintained for 100 – 150 ms. And an ohmic plasma is generated, maintained and terminated within the TF flat-top region. Then, neutral gas (H₂) is pre-filled by PEV control. Next, electron cyclotron heating (ECH) power is injected in EC-assisted ohmic discharge for pre-ionization which guarantees the robust start-up and pre-ionization plasma is formed [18]. In a pure ohmic discharge, ECH power isn't utilized. After the formation of pre-ionization plasmas, PF01(central solenoid) coil current ramps-up. PF05 is used for the formation of the trapped particle configuration which enables a more efficient ECH assisted ohmic start-up [25]. Toroidal loop voltage is induced by PF01 coil current ramp-down. After the generation of plasma current, plasma shape and position are adjusted by using PF06 and PF09-10 coil which provide equilibrium magnetic field. Typical ohmic discharge process is shown in Fig. 2.3. Detailed features of VEST ohmic discharges are described at chapter 4.

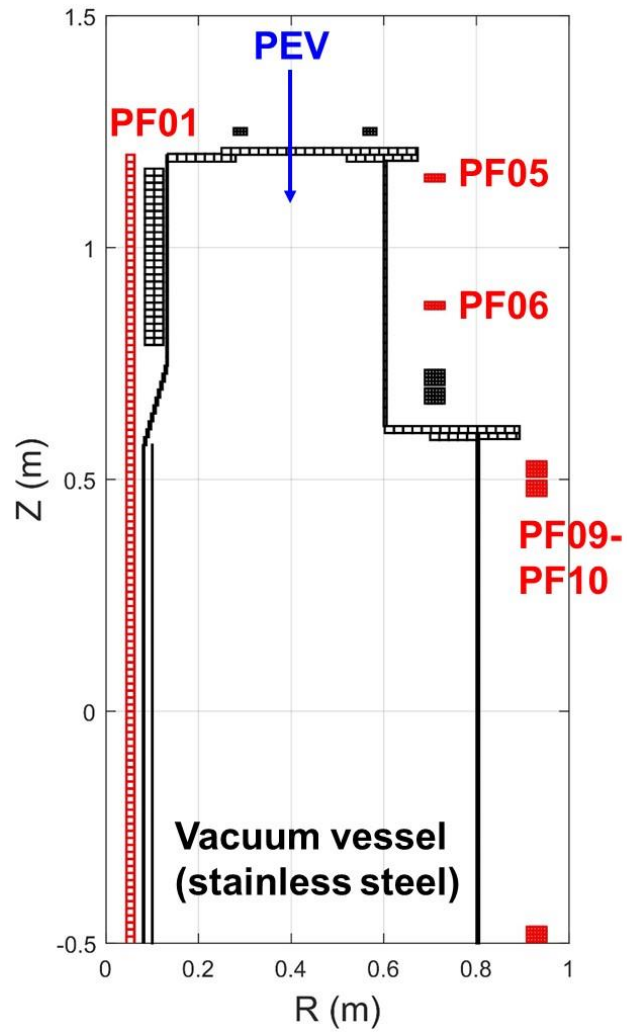


Figure 2.2 Schematic of a poloidal plane in VEST. Vacuum vessel are colored in black. PF coils utilized in typical ohmic discharge are colored in red. Location of PEV is colored in blue.

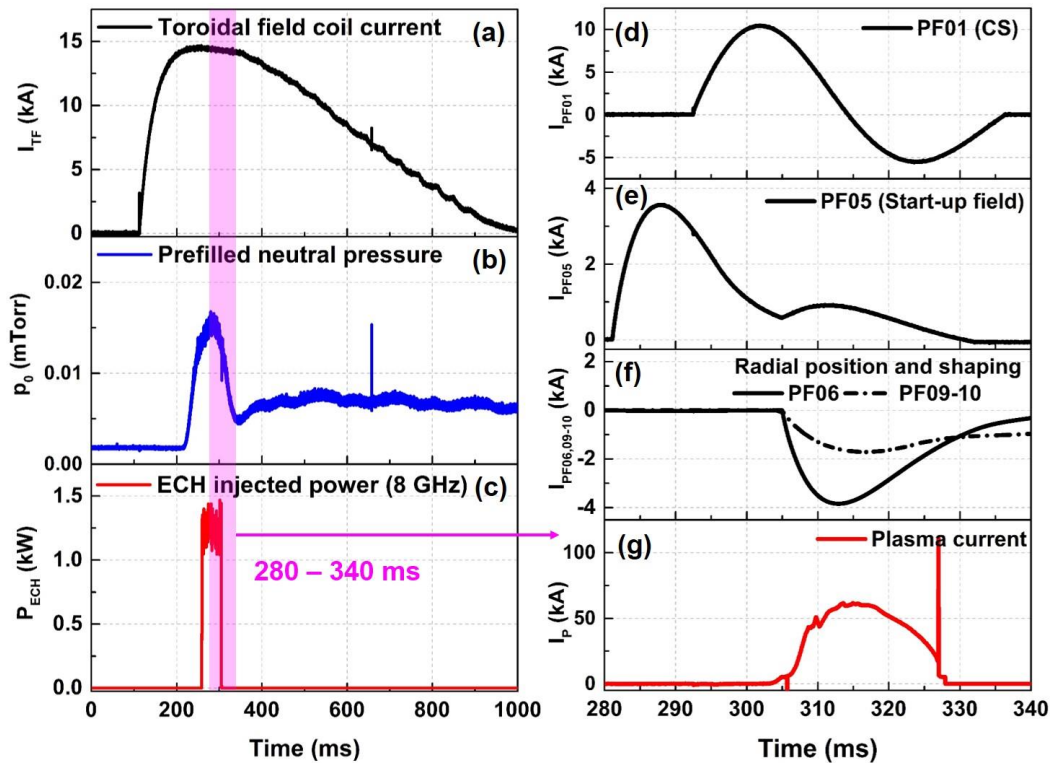


Figure 2.3 EC-assisted ohmic discharge procedure in VEST: evolution of (a) Toroidal field coil current (b) prefill neutral pressure (c) ECH injected power (d) PF01(Central solenoid) coil current (e) PF05 coil current (f) PF06 and PF09-10 coil current and (g) plasma current.

2.2. Equilibrium reconstruction

Tokamak equilibrium can be obtained by solving the Grad-shafranov equation which describes a force balance state in toroidal geometry and this process is called the equilibrium reconstruction. The Grad-shafranov equation is expressed as,

$$\Delta^* \psi = -\mu_0 R J_\phi = -\mu_0 R^2 \frac{\partial p(\psi)}{\partial \psi} - \frac{\partial FF(\psi)}{\partial \psi} \quad (2.1)$$

where ψ is the poloidal magnetic flux, R is the radial position, J_ϕ is the toroidal current density, p is the plasma pressure, $F = RB_\phi/\mu_0$ and $\Delta^* = R^2 \nabla \cdot (\nabla/R^2)$. EFIT is the well-known equilibrium reconstruction code, which efficiently solves for the equilibrium numerically using the Picard iteration scheme by dividing $\psi = \psi_p + \psi_{ext}$ into a plasma and an external component, ψ_p and ψ_{ext} , separately computed using the differential and the integral forms of the Grad-shafranov equation [26]. From the equilibrium reconstruction, the plasma shape (R_0, a, κ, V_p) and global MHD parameters (l_i, W_{mhd}, β) can be obtained. The plasma shape and the normalized internal inductance are important input parameters for the start-up model in this research.

Various diagnostics such as magnetics, Thomson scattering, charge exchange spectroscopy and motional stark effect measurement can be utilized for constraints to solve the equilibrium equation. However, equilibrium reconstruction with only external magnetic constraints in VEST is described at this section.

2.2.1. External magnetic diagnostics and wall modelling

Magnetic diagnostics in VEST are located inside and outside the plasma. Magnetic diagnostics located outside the plasma are called the external magnetic diagnostics [27]. In this research, magnetic diagnostics inside the plasma, internal magnetics [28, 29], are not utilized. The location of the external magnetic diagnostics sensors is shown in Fig.2.4. Total 64 magnetic probes are placed at inboard, outboard and side region and they measure a time derivative vertical component of poloidal magnetic field. Total 11 flux loops are distributed along the poloidal plane and measure the loop voltage at each position. The digitization and processing scheme of the external magnetics is shown in Fig.2.4. Flux loops are sampled at 25 kS/s, while magnetic probes are sampled at 250 kS/s. For constraints in equilibrium reconstruction, signals from flux loops and magnetic probes are digitally filtered to low pass filter with 5 kHz and integrated with time.

Even though typical electromagnetic modelling is conducted with axial symmetry in cylindrical geometry, magnetic sensors in a real situation are significantly affected by 3D effect near the vacuum port. In VEST, inboard limiter with tungsten sheet wraps around the centerstack to protect external magnetic sensors located inboard. Significant eddy current is induced on the inboard limiter during the ohmic discharge. The inboard limiter is partially cut due to the installation of carbon mirror for the interferometer. Due to this situation, magnetic sensors located near the centerstack are affected by such a 3D effect. It is necessary to consider this effect for a reliable equilibrium reconstruction. In order to consider this effect in axial symmetry geometry, effective resistances of wall element are adjusted to minimize the difference in magnetic signals between the experiment and electromagnetic model. This work is conducted on the inboard tungsten limiter and outer wall of main vacuum chamber. Fig.2.5 and 2.6 show the time evolution of poloidal magnetic field and poloidal magnetic flux in vacuum field with experiments and electromagnetic models. In the case of outboard magnetic probes, side magnetic probes

and flux loops, there are little improvements in the model with compensated wall resistances. Better agreements in the case of inboard magnetic probes near the mid-plane are showed by compensating the effective wall resistances. Fig.2.7 shows a correlation factor which is the covariance of two variables divided by the product of their standard deviations and means a measure of linear correlation between two sets of data. The closer the correlation factor is to 1, the stronger the linear correlation between the two sets of data is. As mentioned above, inboard magnetic signals are significantly improved with the compensated wall resistances. The compensated wall resistances are utilized for equilibrium reconstruction as described in section 2.2.2.

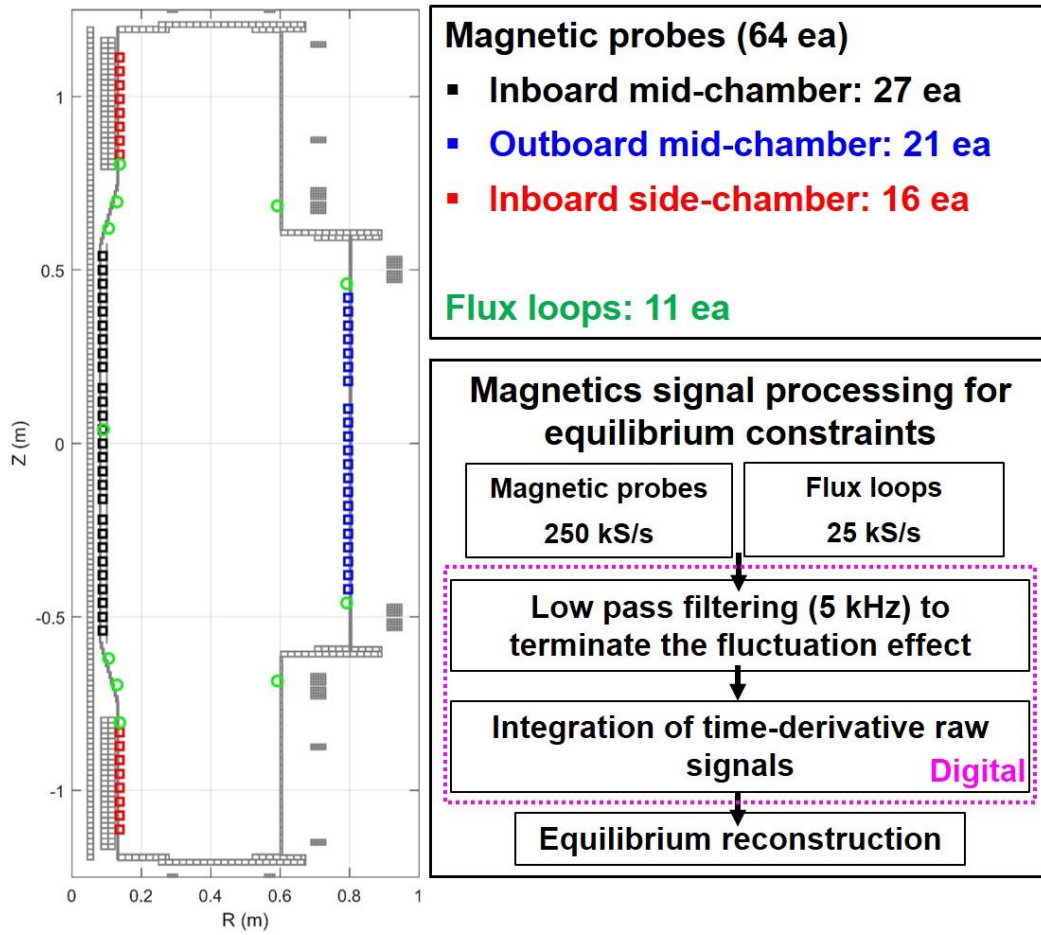


Figure 2.4 Location of the external magnetic diagnostics sensors with poloidal plane view and digitization scheme of external magnetics signals.

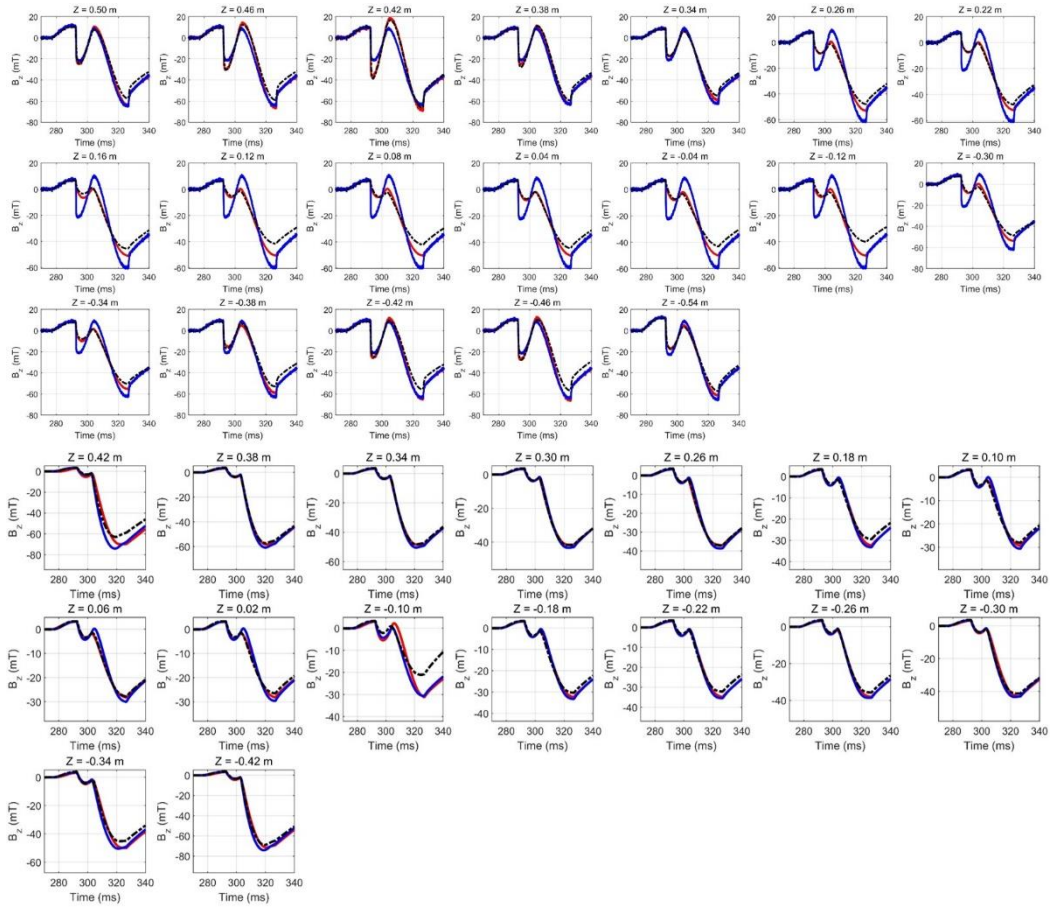


Figure 2.5 Comparison of inboard (upper 3 rows) and outboard (lower 3 rows) magnetic field between experiment and electromagnetic models: Experiment (black dash line) and electromagnetic model (red line: compensated wall resistance, blue line: uncompensated wall resistance).

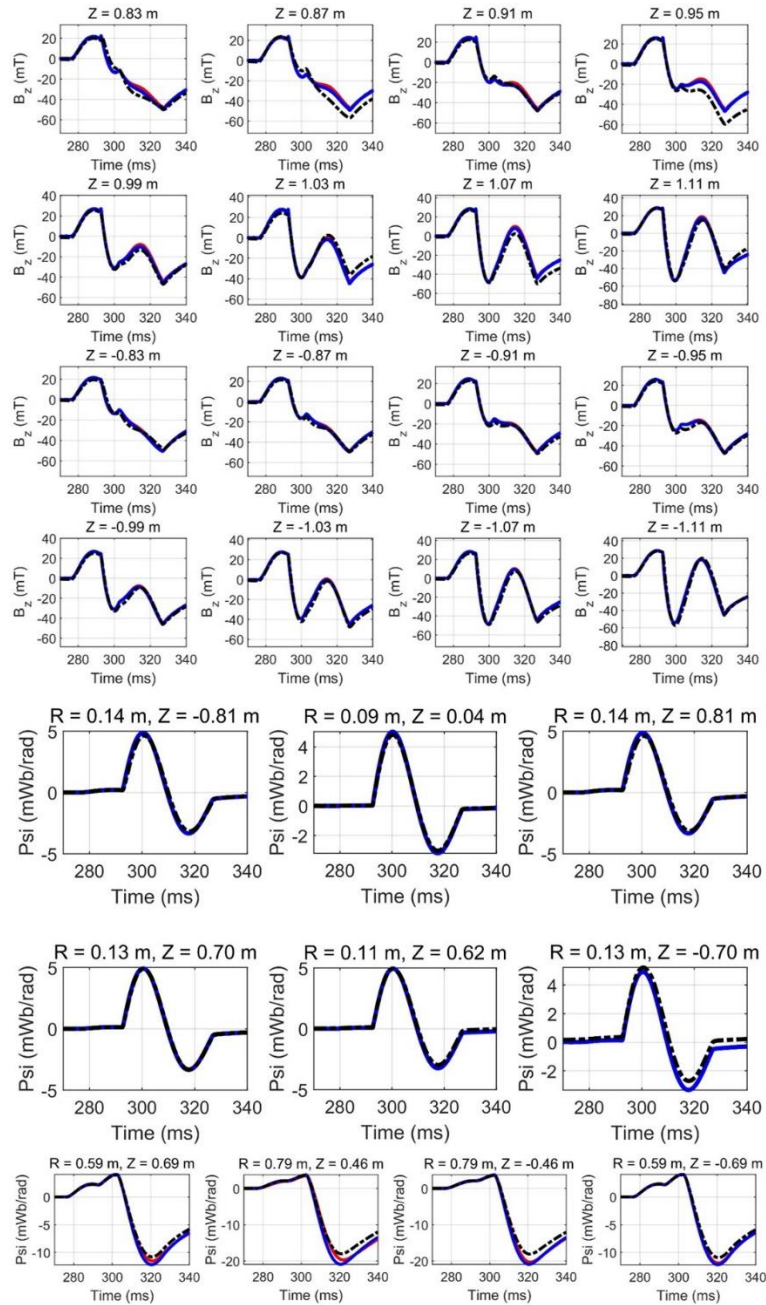


Figure 2.6 Comparison of side magnetic field (upper 4 rows) and flux loops (lower 3 rows) between experiment and electromagnetic models: Experiment (black dash line) and electromagnetic model (red line: compensated wall resistance, blue line: uncompensated wall resistance).

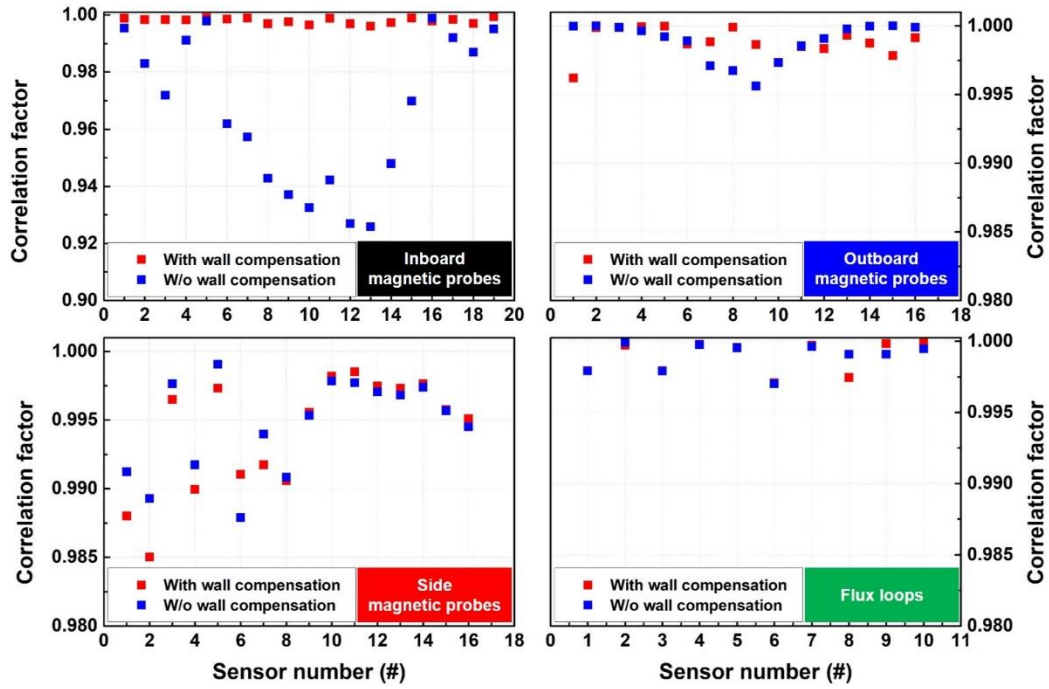


Figure 2.7 Comparison of side magnetic field (upper 4 rows) and flux loops (lower 3 rows) between experiment and electromagnetic models: Experiment (black dash line) and electromagnetic model (red line: compensated wall resistance, blue line: uncompensated wall resistance).

2.2.2. Procedure of equilibrium reconstruction

Equilibrium reconstruction in VEST has a similar process with the EFIT code. In the equilibrium process with only the external magnetics constraints, p' and FF' in the Grad-shafranov equation are modelled to be polynomial basis function as the normalized poloidal magnetic flux, $\psi_N = (\psi - \psi_a)/(\psi_b - \psi_a)$ where ψ_a and ψ_b are the poloidal magnetic flux at magnetic axis and plasma boundary, respectively. The p' and FF' are represented using a set of polynomial basis functions in terms of a number of linear parameters as α_n and γ_n , $p'(\psi) = \sum_n \alpha_n \psi_N^n$, $FF'(\psi) = \sum_n \gamma_n \psi_N^n$. The unknown parameters α_n and γ_n are determined from all available magnetic data by minimizing $\chi^2 = \sum_i \left[\frac{(M_i - C_i)}{\sigma_i} \right]^2$ where M and C are measured and computed sensor signals respectively and σ_i is the uncertainty associated with the i -th magnetic measurement. For the Picard iteration step in equilibrium reconstruction, 2D distribution of the initial poloidal magnetic flux is necessary. In VEST, the shape reconstruction with the finite element methods [30] provides not only the plasma shape information but also the 2D poloidal magnetic flux for the input in the EFIT-like reconstruction. In the shape reconstruction of VEST, current density which is distributed in rectangular grids is determined by minimizing the cost function, $E = \sum_i w_i \left(\frac{M_i - \sum_j K_{ij} I_j}{M_i} \right)^2 + \alpha \sum_i \frac{I_i^2}{I_p^2}$ where w_i is a weight of i -th measurement, M_i is a i -th measurement at fitting time, K_{ij} is a kernel between i -th measurement and j -th element, I_j is a current of j -th element and I_p is a total plasma current measured by a rogowski coil. α is the weighting parameter to prevent the non-physical fitting oscillation of the current elements. The equilibrium features are evaluated using the fitted plasma current distribution, PF coil currents, and the vacuum vessel eddy currents. After the fitting process, distribution of the poloidal magnetic flux is calculated by solving the Ampere's equation. Then, the magnetic axis

and plasma boundary positions are extracted and the flux surfaces are identified by the field following method. Finally, the plasma shape information such as major radius, minor radius, elongation and triangularity can be obtained by the definition of the plasma shape. Fig.2.8 shows an example of VEST equilibrium fitting result by using the shape reconstruction based on the finite element method. Reconstructed magnetic signals are in good agreement with the measured magnetic signals with $\sim 5\%$ error on average. The time evolution in plasma shape and poloidal magnetic flux distribution after the post-processing are shown in Fig.2.9. From the result, there is a transition from the outboard limited plasma to the inboard limited plasma.

EFIT-like equilibrium which solves the Grad-shafranov equation is conducted with inputs obtained by the shape reconstruction. The polynomial orders are empirically set at $n_p = 2$ and $n_F = 2$. Fig.2.10 shows a magnetic fitting error and the time evolution of equilibrium parameters including the plasma shape and global MHD parameters such as the normalized internal inductance and the plasma stored energy. Fitting error on average is $\sim 25\%$ as shown in Fig.2.10. The normalized internal inductance is ~ 0.5 , which means a flat current density profile on average. It is a consistent result in the fast current ramp-up of VEST ohmic discharge. The time evolution in plasma shape and normalized internal inductance are utilized for calculation of plasma circuit parameters such as plasma self-inductance and plasma resistance in the start-up model.

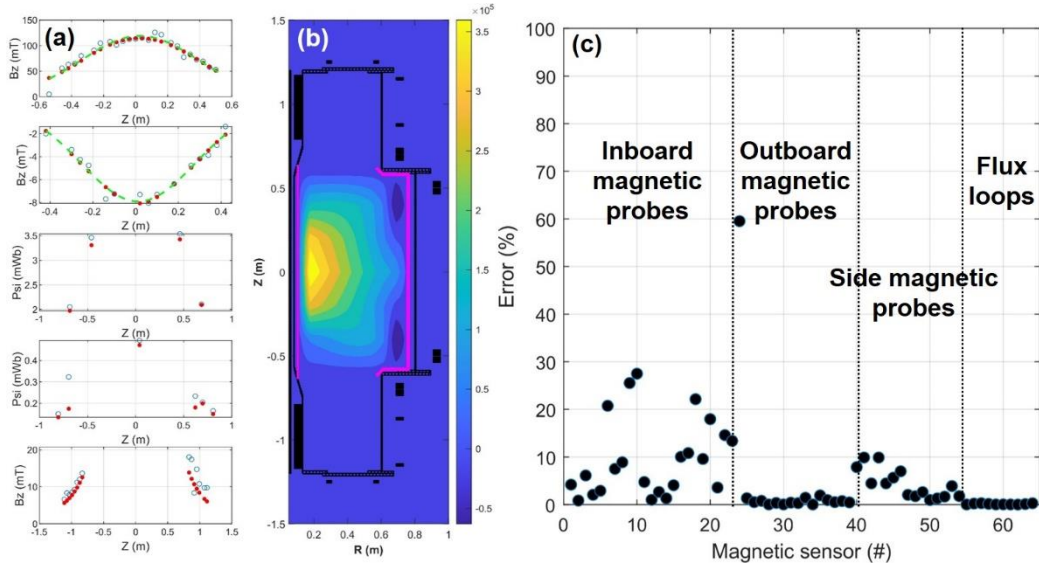


Figure 2.8 Equilibrium fitting result with the shape reconstruction in the shot#37440: (a) magnetic signals (blue circle: measurement, green: measurement after smoothing, red: reconstruction), (b) element distribution in 8 by 5 rectangular grids (unit: A/m²) and (c) magnetic fitting error between measurements and reconstruction.

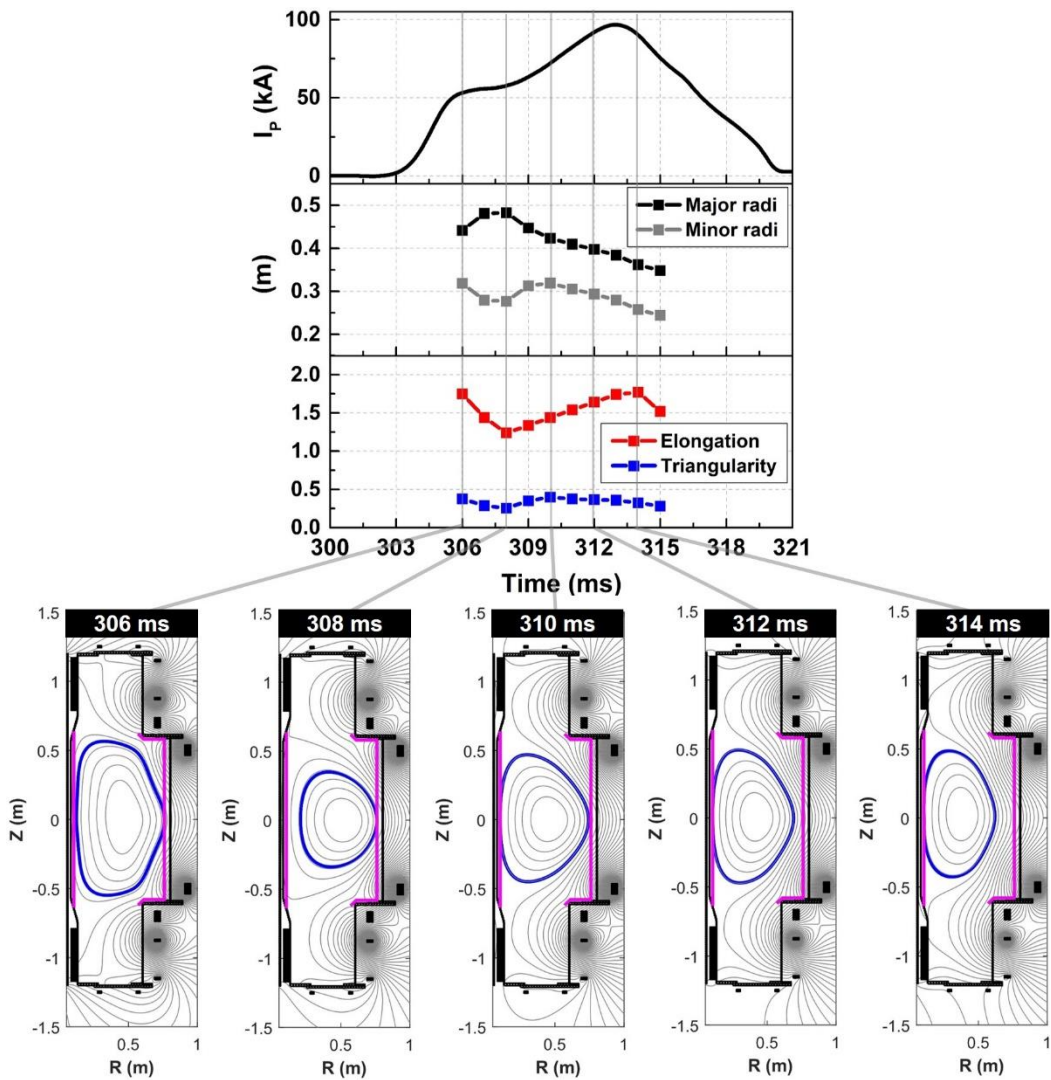


Figure 2.9 Time evolution in plasma current, plasma shape (major radius, minor radius, elongation and triangularity) and 2D poloidal magnetic flux distribution from the shape reconstruction in the shot#37440 (blue: plasma boundary, magenta: limiter position).

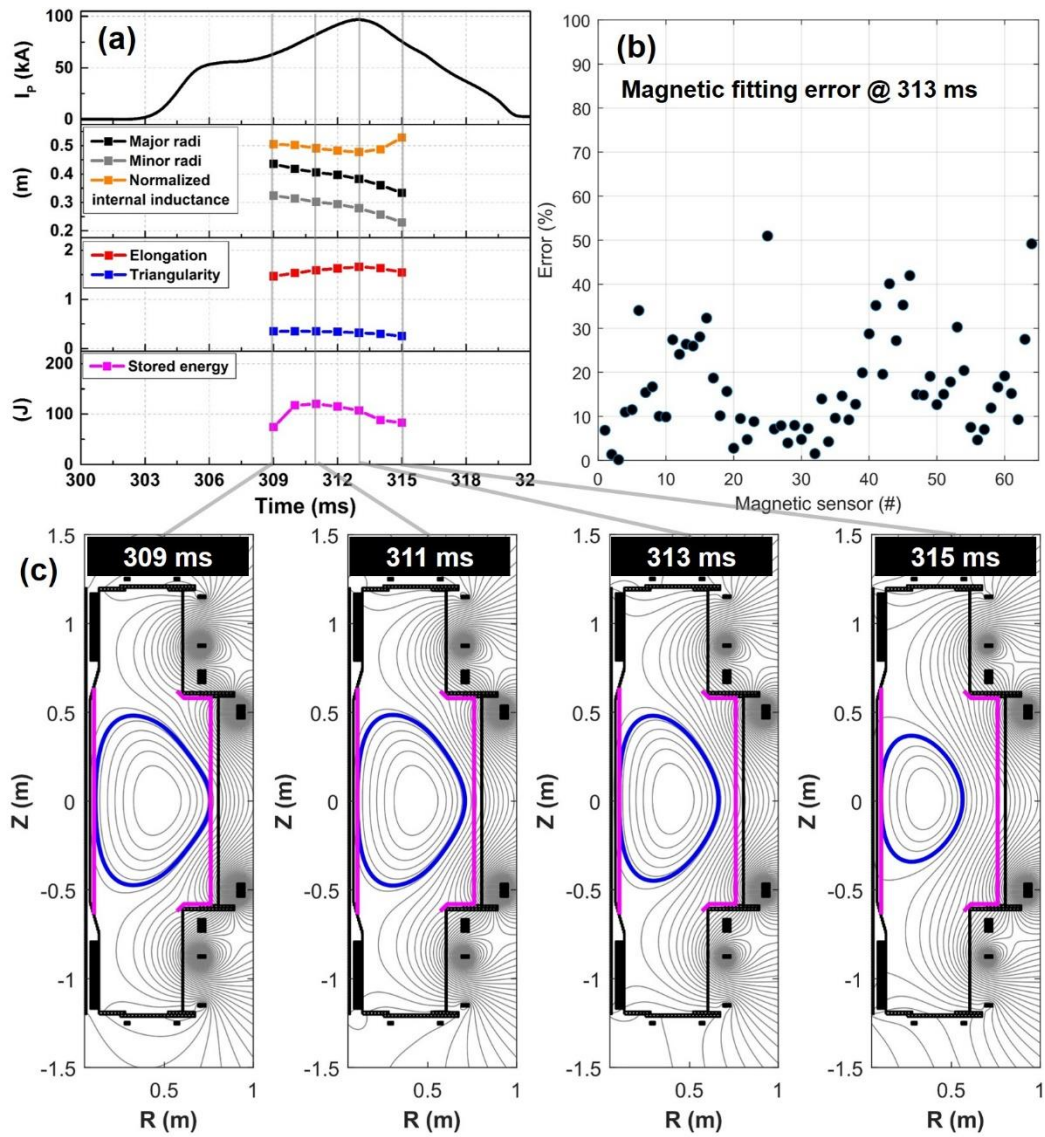


Figure 2.10 (a) Time evolution of plasma current, plasma shape (major radius, minor radius, elongation and triangularity) and global MHD parameters (normalized internal inductance and plasma stored energy), (b) Magnetic fitting error between measurements and reconstruction, and (c) Time evolution of 2D poloidal magnetic flux distribution from the EFIT-like reconstruction in the shot#37440.

2.3. Validation diagnostics

The reliability of model results can typically be confirmed by comparing them with the experimental results. Main outputs of the start-up model are plasma current, electron density & temperature and ion temperature. From these basic output parameters, various synthetic parameters can be obtained such as Z_{eff} , line emission signals with different wavelength and total radiative power and so on after the post-processing. In this section, several diagnostic systems in VEST are described for validation of the plasma start-up model.

2.3.1. Thomson scattering [31-33]

A Thomson scattering (TS) system on VEST has been utilized to measure the electron temperature and density of the core region ($0.23 \text{ m} < R < 0.50 \text{ m}$). The TS system consists of three parts as shown in Fig. 2.11: laser injection system, collection optics system, and polychromator with data acquisition (DAQ) system. Since the duration of VEST plasma discharge is around 20 ms, a laser with a high repetition rate is required to measure the fast time evolution of the electron properties. Therefore, the Nd:YAG laser has been upgraded to the burst mode laser [32]. It has 10 pulses with the energy of 2 J and the repetition rate of 1 kHz. As a result, ten-time point measurements during 10 ms are possible. The TS photons at the core region of plasma is collected by lens array and transferred to the polychromator through the optical fiber. The lens array is designed to focus the straight path of laser. These photons are divided by wavelength at the polychromator to measure the TS spectrum. The polychromator consists of the five interference filters, which cover the wavelength range of 950-1064 nm. Recently, five polychromators are assembled with the fast digitizer whose 32 channels support 200 ns with the sampling rate of 5GS/s. With the VEST TS system, the 1 kHz time evolution of radial profile of the electron temperature and density with five local points has been measured [33]. For validation of the plasma start-up model results, electron temperature and density profile are processed to be a volume averaged because electron temperature and density from the model are zero-dimensional parameters. When the volume averaged values are calculated, boundary in normalized poloidal magnetic flux is set to be from 0 to 0.5 to avoid underestimation of the electron temperature and density. Fig. 2.12 shows the volume-averaged processing of electron temperature and density.

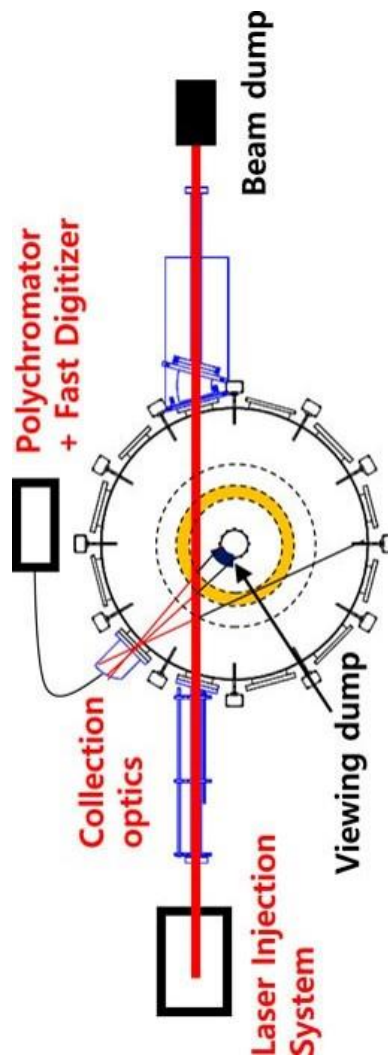


Figure 2.11 Thomson scattering system in VEST.

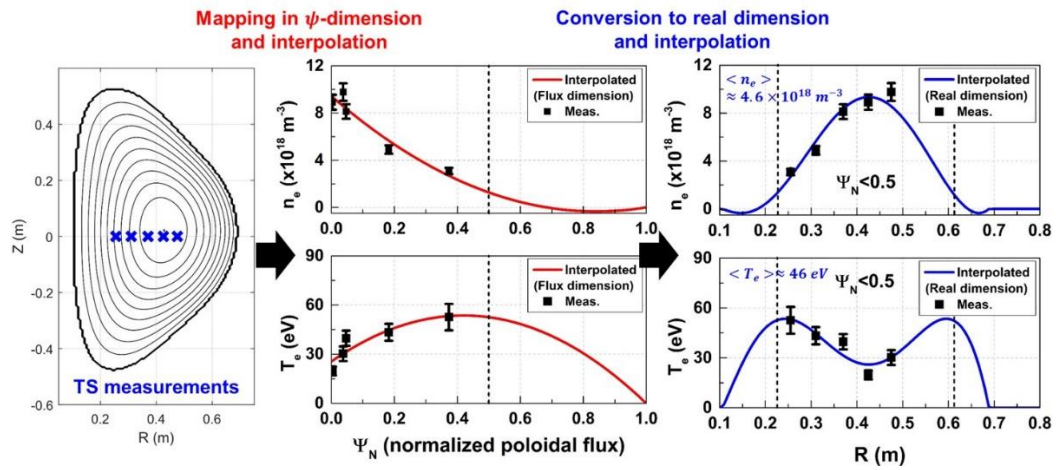


Figure 2.12 Process for obtaining the volume averaged electron temperature and density: (Left) Equilibrium flux surface and Thomson scattering measurement positions, (Middle) Mapping into the flux surface dimension and interpolation, (Right) Conversion to real dimension and volume averaging.

2.3.2. Filterscope system

The filterscope diagnostic system was developed for measuring the time evolution of visible spectral lines from several ions. The diagnostic system consists of collection optics, beam splitters (dichroic mirrors), bandpass filters, and detectors (photomultiplier tubes) with DC power supply. Fig.2.13 shows the schematic of the filterscope diagnostic system. Through the preliminary measurements using existing spectrograph for spectral line survey, we selected seven visible spectral lines such as H_γ (434.0 nm), OII (441.5 nm), $CIII$ (465 nm), H_β (486.1 nm), CII (514.0 nm), OV (650.0 nm), and H_α (656.3 nm). The visible light is collected by collection optics installed at mid-plane ($Z=0$) and split by each beam splitter in order of wavelength from the shortest to longest. Then, the split light is filtered by each bandpass filter and measured by detector as PMT with sampling rate of 250 kHz using digitizer. Even though different seven line emissions can be observed in one ohmic discharge simultaneously, not all filterscope diagnostics are utilized in this study. Two different line emission are utilized in this study: H_α (656.3 nm) and $CIII$ (465 nm). H_α line emission is an essential diagnostic for observation of hydrogen neutral burn-through. In other words, whether burn-through of hydrogen neutral are successful or not can be determined with the H_α line emission signal in both experiment and simulation. $CIII$ line emission is a very good indication of inboard wall interactions in VEST discharges. Therefore, $CIII$ line emission is also an essential diagnostic for plasma wall interaction model in the plasma start-up model.

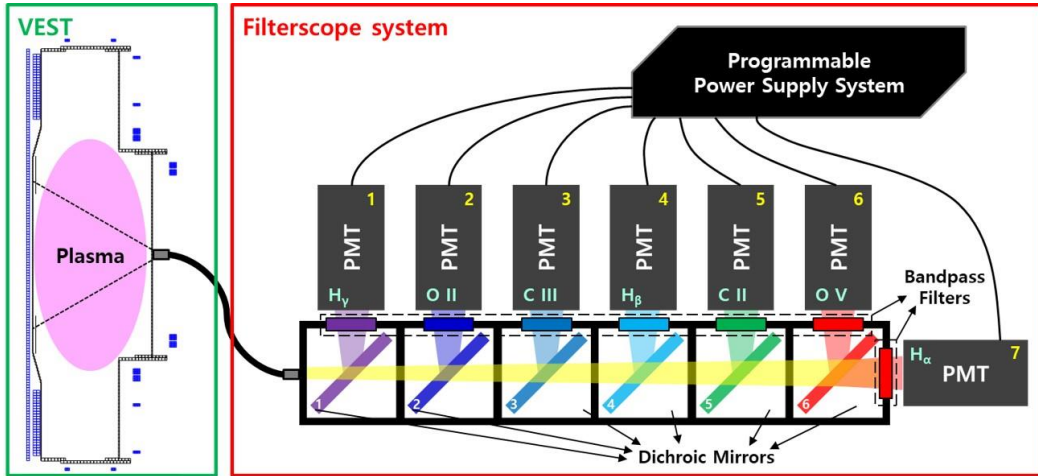


Figure 2.13 Filterscope system in VEST.

Chapter 3. Development of Full Electromagnetic Start-up Model in VEST

3.1. Full electromagnetic model

Prediction of the plasma current evolution is very important part at tokamak start-up phase. The plasma current evolution at tokamak start-up phase can be described with a simple circuit system and it is mainly calculated by electric circuit equation in start-up model. There are several factors which determine the plasma current evolution such as loop voltage, plasma inductance and plasma resistance. It is necessary to estimate these electric circuit parameters exactly for a reliable plasma current evolution. In this section, models for determination of circuit parameters are described. First, a full electromagnetic circuit model is described for exact calculation of loop voltage as driving force which generates the plasma current with consideration of PF coil and vacuum vessel structure. Secondly, plasma inductance and resistance model are described with low aspect ratio features.

3.1.1. Full circuit equation [17]

Circuit model in the previous start-up modelling studies typically consists of a single circuit equation in terms of plasma current. However, the circuit system in real situation are composed of plasma current, PF coil currents and vacuum vessel eddy current induced in passive conducting structures, all of which are linked one another through mutual inductances. The PF coils and the toroidally continuous structures such as the vacuum vessel are approximated to a set of single filaments with equivalent resistance and inductance. The vacuum vessel elements are treated as coils with zero voltage, that is, eddy currents induced only by electro motive force from the mutual inductance between coils and toroidally continuous structures.

The current of each filament can be solved by simple circuit equation with matrix form as following: $\vec{V}_{cv} = \vec{R}_{cv}\vec{I}_{cv} + \vec{M}_{cv} \frac{d\vec{I}_{cv}}{dt}$ where \vec{V}_{cv} is a $n \times 1$ column vector of voltage applied by power supply system to the PF coils and vacuum vessel elements (zero for the vector of vacuum vessel components). \vec{R}_{cv} is a $n \times n$ diagonal matrix of resistances and \vec{M}_{cv} is a $n \times n$ symmetric matrix of inductances in the PF coils and vacuum vessel elements. \vec{I}_{cv} is a $n \times 1$ column vector of currents in the PF coils and vacuum vessel elements. In the same manner, plasma current can be included in above circuit matrix by attaching the plasma current in the $(n + 1)$ th row of the corresponding column vectors. The plasma resistance R_p and self-inductance L_p are added in the resistance matrix and inductance matrix, respectively. Also, mutual inductance between the plasma current and the PF & vacuum vessel structure should be included in the inductance matrix. Then, the extended current vector, voltage vector, resistance matrix and mutual inductance matrix can be written as

$$\begin{aligned}
\vec{I}_{cvp} &= \begin{bmatrix} I_{c1} \\ I_{c2} \\ \vdots \\ I_{v1} \\ I_{v2} \\ \vdots \\ I_p \end{bmatrix}, \quad \vec{V}_{cvp} = \begin{bmatrix} V_{c1} \\ V_{c2} \\ \vdots \\ V_{v1} \\ V_{v2} \\ \vdots \\ V_p \end{bmatrix}, \quad \vec{R}_{cvp} = \begin{bmatrix} R_{c1} & 0 & \cdots & 0 & 0 & \cdots & 0 \\ 0 & R_{c2} & \cdots & 0 & 0 & \cdots & 0 \\ \vdots & \ddots & \vdots & \vdots & \vdots & \cdots & \vdots \\ 0 & 0 & \cdots & R_{v1} & 0 & \cdots & 0 \\ 0 & 0 & \cdots & 0 & R_{v2} & \cdots & 0 \\ \vdots & \vdots & \vdots & \vdots & \vdots & \ddots & \vdots \\ 0 & 0 & \cdots & 0 & 0 & \cdots & R_p \end{bmatrix} \\
\vec{M}_{cvp} &= \begin{bmatrix} L_{c1} & M_{c1,c2} & M_{c1,c3} & 0 & M_{c1,v1} & M_{c1,v2} & M_{c1,v3} & \cdots & M_{c1,p} \\ M_{c2,c1} & L_{c2} & M_{c2,c3} & 0 & M_{c2,v1} & M_{c2,v2} & M_{c2,v3} & \cdots & M_{c2,p} \\ M_{c3,c1} & M_{c3,c2} & L_{c3} & \vdots & M_{c3,v1} & M_{c3,v2} & M_{c3,v3} & \cdots & M_{c3,p} \\ \vdots & \vdots & \vdots & \ddots & \vdots & \vdots & \vdots & \cdots & \vdots \\ M_{v1,c1} & M_{v1,c2} & M_{v1,c3} & \cdots & L_{v1} & M_{v1,v2} & M_{v1,v3} & \cdots & M_{v1,p} \\ M_{v2,c1} & M_{v2,c2} & M_{v2,c3} & \cdots & M_{v2,v1} & L_{v2} & M_{v2,v3} & \cdots & M_{v2,p} \\ M_{v3,c1} & M_{v3,c2} & M_{v3,c3} & \cdots & M_{v3,v1} & M_{v3,v2} & L_{v3} & \cdots & M_{v3,p} \\ \vdots & \vdots & \vdots & \vdots & \vdots & \vdots & \vdots & \ddots & \vdots \\ M_{p,c1} & M_{p,c2} & M_{p,c3} & \cdots & M_{p,v1} & M_{p,v2} & M_{p,v3} & \cdots & L_p \end{bmatrix}
\end{aligned} \tag{3.1}$$

In more realistic situation, plasma current and its radial and vertical position can change in time. This require additional term $\frac{d\vec{M}_{cvp}}{dt}\vec{I}_{cvp}$ in the extended circuit system equation. The circuit equation with time derivative of mutual inductance can be written as:

$$\begin{aligned}
\vec{V}_{cvp} &= \vec{R}_{cvp}\vec{I}_{cvp} + \frac{d\vec{M}_{cvp}}{dt}\vec{I}_{cvp} \\
&= \left(\vec{R}_{cvp} + \frac{\partial\vec{M}_{cvp}}{\partial R}\frac{\partial R}{\partial t} + \frac{\partial\vec{M}_{cvp}}{\partial Z}\frac{\partial Z}{\partial t} + \frac{dL_p}{dt} \right) \vec{I}_{cvp} + \vec{M}_{cvp} \frac{d\vec{I}_{cvp}}{dt} \\
\frac{d\vec{I}_{cvp}}{dt} &= \vec{M}_{cvp}^{-1} \left(\vec{V}_{cvp} - \left(\vec{R}_{cvp} + \frac{\partial\vec{M}_{cvp}}{\partial R}\frac{\partial R}{\partial t} + \frac{\partial\vec{M}_{cvp}}{\partial Z}\frac{\partial Z}{\partial t} + \frac{dL_p}{dt} \right) \vec{I}_{cvp} \right)
\end{aligned} \tag{3.2}$$

Note, R and Z are the radial and vertical position of each element, respectively. The elements of time derivative of mutual inductance corresponding to PF coil-vacuum vessel and vacuum vessel-vacuum vessel are zero because the positions of all PF coils and

vacuum vessel are fixed. Full circuit system equation is shown in Fig. 3.1. In this study, PF coil currents are experimentally measurable parameters. Therefore, $\frac{d\vec{I}_{vp}}{dt}$ can be obtained by solving the reduced circuit system equation with known \vec{I}_c and $\frac{d\vec{I}_c}{dt}$. The reduced circuit system equation can be written as:

$$\begin{aligned}
 & \begin{bmatrix} \frac{dI_{v1}}{dt} \\ \frac{dI_{v2}}{dt} \\ \frac{dI_{v3}}{dt} \\ \vdots \\ \frac{dI_p}{dt} \end{bmatrix} = \vec{M}_{vp}^{-1} \begin{bmatrix} M_{c1,v1} & M_{v1,c2} & M_{v1,c3} & \cdots \\ M_{c2,v1} & M_{v2,c2} & M_{v2,c3} & \cdots \\ M_{c3,v1} & M_{v3,c2} & M_{v3,c3} & \cdots \\ \vdots & \vdots & \vdots & \vdots \\ M_{p,v1} & M_{p,c2} & M_{p,c3} & \cdots \end{bmatrix} \begin{bmatrix} \frac{dI_{c1}}{dt} \\ \frac{dI_{c2}}{dt} \\ \frac{dI_{c3}}{dt} \\ \vdots \end{bmatrix} \\
 & -\vec{M}_{vp}^{-1} \begin{bmatrix} 0 & 0 & \cdots & R_{v1} & 0 & \cdots & \frac{\partial M_{v1,p}}{\partial R} \frac{\partial R}{\partial t} + \frac{\partial M_{v1,p}}{\partial Z} \frac{\partial Z}{\partial t} \\ 0 & 0 & \cdots & 0 & R_{v2} & \cdots & \vdots \\ \vdots & \vdots & \vdots & \vdots & \vdots & \ddots & \vdots \\ \frac{\partial M_{c1,p}}{\partial R} \frac{\partial R}{\partial t} + \frac{\partial M_{c1,p}}{\partial Z} \frac{\partial Z}{\partial t} & \cdots & \cdots & \frac{\partial M_{v1,p}}{\partial R} \frac{\partial R}{\partial t} + \frac{\partial M_{v1,p}}{\partial Z} \frac{\partial Z}{\partial t} & \cdots & \cdots & R_p + \frac{dL_p}{dt} \end{bmatrix} \begin{bmatrix} I_{c1} \\ I_{c2} \\ \vdots \\ I_{v1} \\ I_{v2} \\ \vdots \\ I_p \end{bmatrix} \\
 & \hspace{20em} (3.3)
 \end{aligned}$$

V_c	=	M_c	M_{cv}	M_{cp}	$\frac{dI_c}{dt}$	+	R_c	0	0	I_c
0		M_{vc}	M_{vv}	M_{vp}	$\frac{dI_v}{dt}$		0	R_v	0	I_v
0		M_{pc}	M_{pv}	L_p	$\frac{dI_p}{dt}$		0	0	R_p	I_p
+										
		0	0	$\frac{\partial M_{cp}}{\partial R} \frac{\partial R}{\partial t} + \frac{\partial M_{cp}}{\partial Z} \frac{\partial Z}{\partial t}$						I_c
		0	0	$\frac{\partial M_{cp}}{\partial R} \frac{\partial R}{\partial t} + \frac{\partial M_{cp}}{\partial Z} \frac{\partial Z}{\partial t}$						I_v
		$\frac{\partial M_{cp}}{\partial R} \frac{\partial R}{\partial t} + \frac{\partial M_{cp}}{\partial Z} \frac{\partial Z}{\partial t}$		$\frac{\partial M_{vp}}{\partial R} \frac{\partial R}{\partial t} + \frac{\partial M_{vp}}{\partial Z} \frac{\partial Z}{\partial t}$			$\frac{dL_p}{dt}$			I_p

Figure 3.1 Full circuit system: blue box (PF coils - known parameters) and yellow box (vacuum vessel and plasma current - unknown parameters).

In the circuit system equation, resistance and inductance in each element (plasma current, PF coils and vacuum vessel) can be easily obtained by simple analytic formula. Especially, plasma resistance and inductance parameters are calculated by using the advanced model which will be described at section 3.1.2. By solving the circuit system equation, time evolution of currents in all vacuum vessel elements and plasma is obtained. Solutions of the circuit system equation are utilized in the Townsend model to estimate the plasma volume.

In order to validate the full electromagnetic model, flux loops data between the model and measurements are compared in simple vacuum magnetic field circumstance without and without plasma current. First of all, the vacuum vessel is discretized into 186 pieces and PF coils with large size such as PF01 are discretized into several pieces to enhance the accuracy of the simulation results. The input geometry and each element dimension of VEST are shown in Fig. 3.2. Fig. 3.3 show the input PF coil current waveforms and comparison of flux loops data between the full electromagnetic model and measurements in the vacuum discharge case without plasma current. The flux loops data from the full electromagnetic model are reasonably agreement with the experimental measurements. Secondly, the full electromagnetic model is conducted with experimental plasma current evolution as shown in Fig.3.4. Plasma current is simply set to be a single filamentary current and its position has been obtained from the magnetic equilibrium reconstruction described in section 2. There are differences between model and measurements at early start-up phase especially in far from the plasma filament. It is thought that the discrepancies are caused by the simple plasma current model, i.e. single filamentary current. Even though there are differences in flux loop signals between model and measurements, final loop voltage waveform at plasma center position isn't affect significantly. However, for more realistic situation, plasma modelling in the full electromagnetic circuit model will be improved.

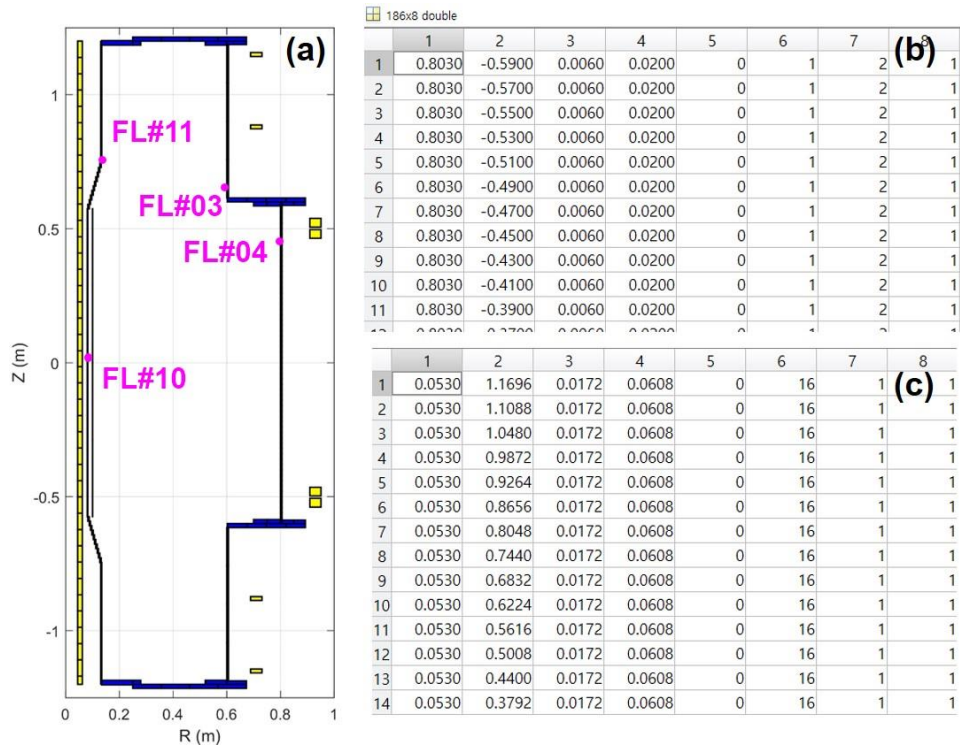


Figure 3.2 (a) Input VEST structure (blue: vacuum vessel, yellow: PF coils and magenta: flux loops) and vacuum vessel (b) and PF coils (c) element table (First column: R-position of each element, second column: R-position of each element, third column: width of each element, fourth column: height of each element, fifth: tilting angle of each element, sixth: toroidal turn number of each element, seventh: material type [0: tungsten, 1: copper, 2: stainless steel] and eight column: section number)

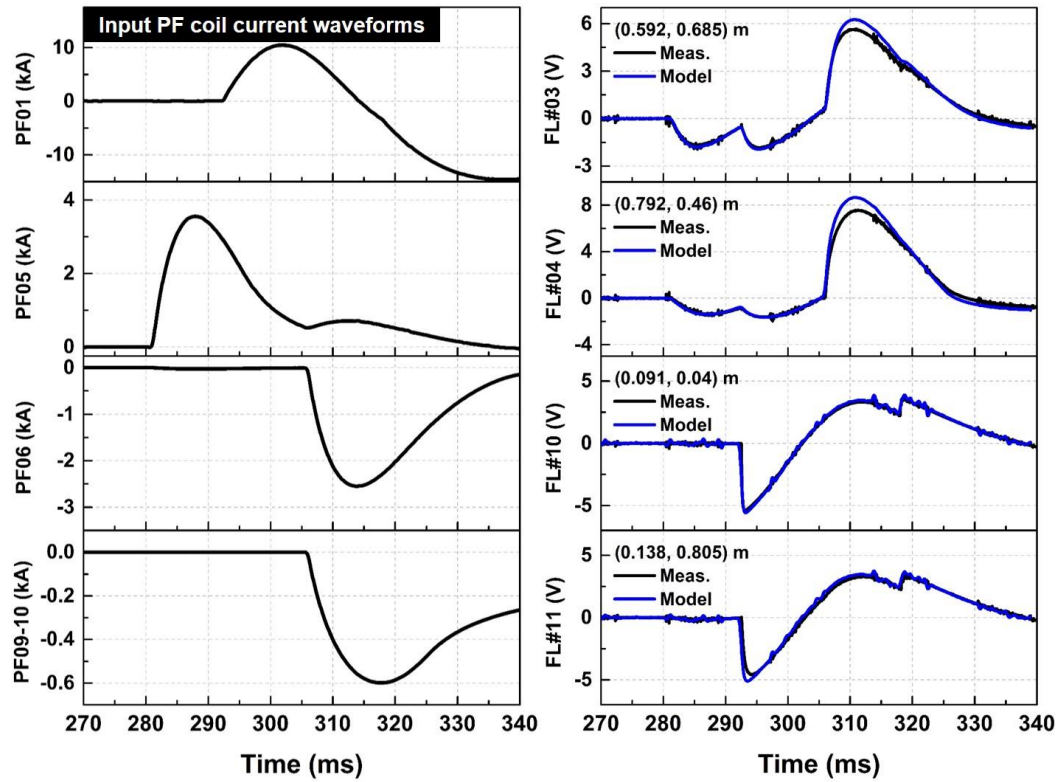


Figure 3.3 (Left) Input PF coil current waveforms for full EM model in the vacuum magnetic field calculation and (Right) flux loops data from full EM model (blue line) and experimental measurements (black line).

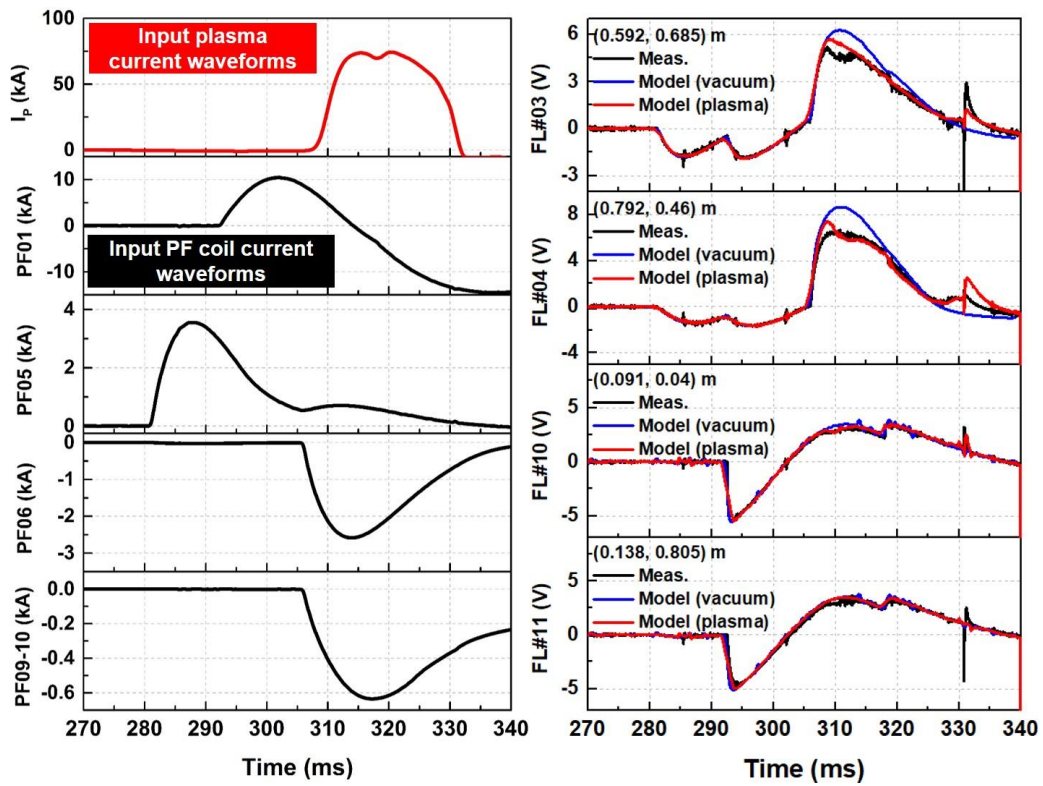


Figure 3.4 (Left) Input plasma and PF coil current waveforms for full EM model in the magnetic field calculation (Right) flux loops data from full EM model (red line – with plasma and blue line – w/o plasma) and experimental measurements (black line – with plasma).

3.1.2. Plasma circuit model [35]

Tokamak plasma has a self-inductance component which is dependent on the plasma shape information and the toroidal current density profile. Self-inductance component which depends on the plasma shape information is called to be a plasma external self-inductance, L_e . Other self-inductance related to the toroidal current density is a plasma internal self-inductance, L_i .

The plasma external self-external inductance describes the plasma current's own contribution to the flux surface at the plasma boundary. Therefore, unlike the internal self-inductance, it has significant dependence on the plasma shape such as aspect ratio and elongation. A simple external self-inductance formula with assumption on the large aspect ratio plasma is expressed by $L_e = \mu_0 R_0 \left\{ \ln \left(\frac{8}{\epsilon \kappa} \right) - 2 \right\}$ where μ_0 is the vacuum permeability, R_0 is the plasma major radius, κ is the plasma elongation and ϵ is the inverse aspect ratio. Typical tokamak start-up models have utilized above simple large aspect ratio formula. And there were several reports which show good agreements between experiments and model based on the simple formula in large aspect ratio device [12-15, 36]. However, this simple formula is invalid in spherical torus plasmas. For moderate elongation and low aspect ratio regime, the plasma external self-inductance can be negative due to the logarithmic nature as shown in Fig. 3.5. Therefore, it is necessary to establish a proper model for the plasma external self-inductance in ST plasmas. There is an improved formula developed by Hirshman and Neilson which can be utilized regardless of aspect ratio [37] and this formula has been utilized in several start-up modelling for ST plasmas [38, 39]. The improved formula is expressed as,

$$L_e = \mu_0 R_0 \left\{ \frac{a(\epsilon)(1 - \epsilon)}{(1 - \epsilon) + b(\epsilon)\kappa} \right\} \quad (3.4)$$

where $a(\epsilon) = (1 + 1.81\sqrt{\epsilon} + 2.05\epsilon) \ln \left(\frac{8}{\epsilon} \right) - (2.0 + 9.25\sqrt{\epsilon} - 1.21\epsilon)$ and

$$b(\epsilon) = 0.73\sqrt{\epsilon}(1 + 2\epsilon^4 - 6\epsilon^5 + 3.7\epsilon^6).$$

The red line in Fig. 3.1 shows that plasma external self-inductance has normal value at low aspect ratio regime. Confirmation has been conducted whether the improved formula can be utilized in a specific device using the equilibrium reconstruction results spanning the operating space of VEST with its actual PF coils and vacuum vessel structure. Fig. 3.6 shows the comparison in normalized external self-inductance between analytic formulae and real value from the equilibrium reconstruction. Even though the normalized external self-inductance value with advanced formula derived by Hirshman and Neilson is closer to the equivalent line than that of the large aspect ratio formula, it still has differences. To enhance the applicability to specific device, Hirshman and Neilson formula has been modified by refitting coefficients in the formula using experimental equilibrium reconstruction data in VEST. Fitting the coefficients to the VEST equilibrium provides the new values in Table 3.1. By using the modified Hirshman and Neilson formula, each equilibrium point is well aligned in the equivalent line as shown in Fig. 3.6 and this new plasma external self-inductance model is utilized for VEST plasmas.

$$a(\epsilon) = \left\{ 1 + \sum_{n=1}^{\frac{N_a}{2}} a_n (\sqrt{\epsilon})^n \right\} \ln\left(\frac{8}{\epsilon}\right) - \left\{ 2.0 + \sum_{n=1}^{\frac{N_a}{2}} a_{(\frac{N_a}{2}+n)} (\sqrt{\epsilon})^n \right\} \quad \text{and} \quad (3.5)$$

$$b(\epsilon) = b_1 \sqrt{\epsilon} \left\{ 1 + \sum_{n=2}^{\frac{N_b}{2}} b_n \epsilon^{2+n} \right\}$$

$a_n (N_a=4)$		$b_n (N_b=4)$	
Original	Modified	Original	Modified
1.81	1.56	0.73	5.65
2.05	1.66	2.00	-4.01
9.25	8.85	-6.00	-7.04
-1.21	-2.44	3.70	12.1

Table 3.1. Original and modified fitting coefficients for external inductance model (3.3).

Physically, the plasma internal self-inductance is defined to be the total poloidal magnetic energy inside the plasma volume and it is expressed as, $L_i = \frac{\mu_0 R_0 l_i}{2}$ where l_i is a normalized internal inductance and is obtained from equilibrium reconstruction. The normalized internal inductance is defined as l_i and its physical meaning is a hollowness of the toroidal current density. For example, when the current density is flat, l_i is ~ 0.5 . Strictly, l_i is a physical parameter with existence of the closed flux surface. So, it can be physically invalid to apply this parameter to the phase before the formation of the closed flux surface. Also, even though l_i is a parameter which has a profile effect, there is a limitation to simulate a dynamic phase such as a transition from the plasma breakdown to the burn-through with a simple 0D parameter. However, l_i is utilized in the overall start-up phase because evolution of the plasma current is calculated by the electric circuit equation regardless of the start-up phase. The initial l_i is assumed to be 0.5, i.e. uniform current density at the plasma breakdown initiation. The l_i during the dynamic phase is interpolated with the initial l_i and the l_i available from the equilibrium reconstruction as shown in Fig.3.7.

Plasma resistance based on the spitzer resistivity is simply expressed as,

$$R_p = 5 \times 10^{-5} \times \ln \Lambda \times Z_{eff} \times \frac{R_0}{a^2 \kappa} \times T_e^{-\frac{3}{2}} \text{ (eV)} \quad (3.6)$$

Here $\ln \Lambda$ is the Coulomb logarithm and Z_{eff} represents the effective charge defined as

$$Z_{eff} = \frac{\sum_A \sum_z n_A^{z+} z^2}{\sum_A \sum_{z \geq 1} n_A^{z+} z}$$

where subscript A represents hydrogen or an impurity. z means an ionic charge state. Accordingly, n_A^{z+} indicates hydrogen ion density n_H^{1+} or impurity ion densities n_I^{z+} of which the charge state is z . Importantly, the spitzer resistance is large dependent of the electron temperature, T_e . Typically, the trapped particle fraction can affect the effective plasma resistance and it is called the neoclassical resistance.

Neoclassical resistance adds a multiplicative factor that increases the resistance: $R_{neo} = F_{neo}R_p$ where F_{neo} can be calculated using an analytic function developed numerically for arbitrary collisionality by O. Sauter [40]. The analytic function valid for arbitrary f_t, ν_{e*} and Z_{eff} are given as follows:

$$F_{neo} = \frac{\eta_{neo}}{\eta_{sptz}} = \frac{\sigma_{sptz}}{\sigma_{neo}} = \frac{1}{1 - \left(1 + \frac{0.36}{Z_{eff}}\right)X + \frac{0.59}{Z_{eff}}X^2 - \frac{0.23}{Z_{eff}}X^3} \quad (3.7)$$

where $X = \frac{f_t}{1 + (0.55 - 0.1f_t)\sqrt{\nu_{e*} + 0.45(1-f_t)\nu_{e*}/Z_{eff}^{3/2}}}$.

Here f_t is the trapped particle fraction, and ν_{e*} is the electron collisionality expressed as $\nu_{e*} = 6.921 \times 10^{-18} \frac{qRn_e Z_{eff} \ln \Lambda_e}{T_e^2 \epsilon^{3/2}}$ where q is the safety factor, n_e is the electron density. The trapped particle fraction can be easily estimated by using Pade approximation [41]:

$$f_c^p \cong \frac{(1 - \epsilon^2)^{-\frac{1}{2}}(1 - \epsilon)^2}{1 + 1.46\epsilon^{\frac{1}{2}} + 0.2\epsilon}, f_t = 1 - f_c^p \quad (3.8)$$

In order to validate this approach in the plasma resistance model, numerical simulation has been conducted using NCLASS code [42] which can calculate the neoclassical resistivity with given plasma equilibrium and kinetic profiles. Fig. 3.8 shows the results from NCLASS simulation. The neoclassical factor has 1.5~2.0 with given plasma parameters. There is a discrepancy between the NCLASS and O. Sauter model. Therefore, the compensation factor is considered and this factor is utilized in the resistance model.

Importantly, trapped particles mainly occur after the formation of the closed flux surface. Therefore, it is physically invalid to apply the neoclassical theory in the open field structure as in the case of the normalized internal inductance. To resolve this problem, the time point of transition from the open field dominant phase to the closed flux surface

dominant phase is set based on the plasma current and the H_α line emission signal. Fig.3.9 shows time evolutions in the plasma current and H_α line emission signal and the plasma volume structure calculated by the Townsend volume model which will be described after this section. At 305 ms before the H_α peak, the open field structure is formed with low plasma current about 5 kA. After the plasma breakdown, both the open field and the closed flux surface structures exist simultaneously near 305.6 ms as shown in Fig.3.9 (b). Near the H_α peak, the volume model shows only the closed flux surface structure at 306 ms. The plasma current at the H_α peak is about 20 kA in this ohmic discharge and this value of the plasma current is to set to be a standard for the transition from the open field-dominant phase to the closed flux surface-dominant phase. In the open field-dominant phase, the classical spitzer resistivity is utilized. After this phase, the neoclassical resistivity model by O. Sauter is applied. VEST Ohmic discharges utilized for validation in this research have similar features as shown in Fig.3.9. However, the ad-hoc parameters cannot be applied to all operational conditions such as a low stray magnetic field. Therefore, the model during the transition from the open field-dominant phase to the closed flux surface-dominant phase will be improved to be applied for various operational conditions.

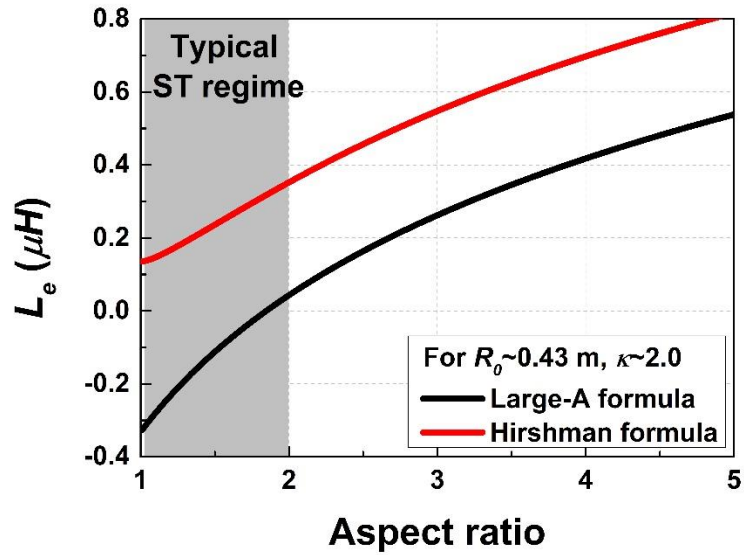


Figure 3.5 Comparison of plasma external self-inductance value between the large aspect ratio (black line) and the Hirshman (red line) models with aspect ratio.

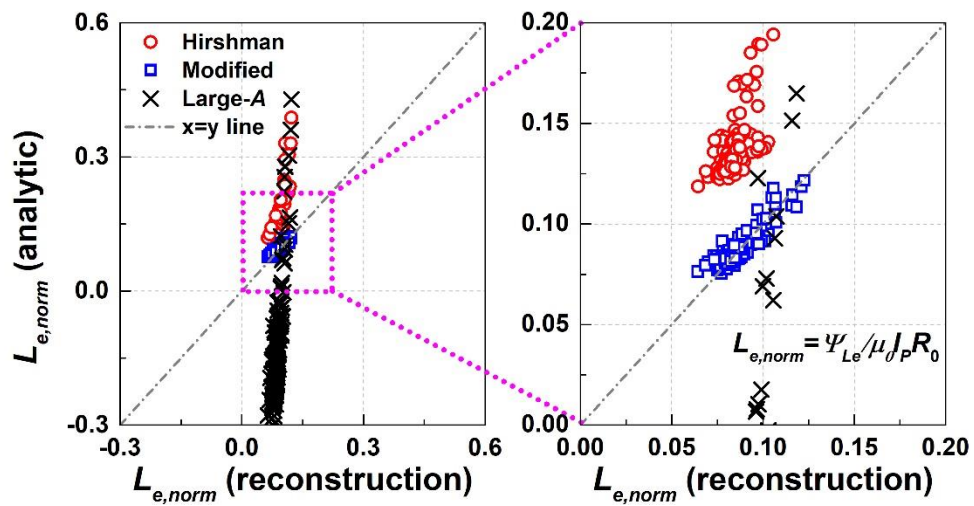


Figure 3.6 Comparison of normalized analytic and exact external self-inductance (reconstruction) values for the Hirshman (red circle), new modified (blue square) and large aspect ratio (black cross) models.

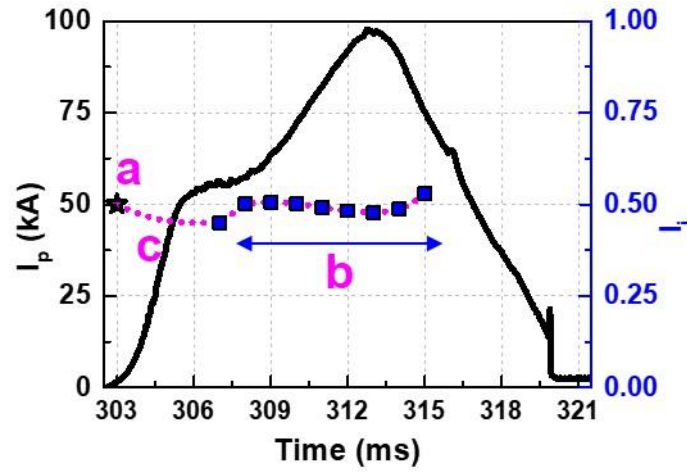


Figure 3.7 Time evolution in the plasma current and the normalized internal inductance from the equilibrium reconstruction (a: initial assumption, b: equilibrium reconstruction, and c: interpolation) in the shot#37440.

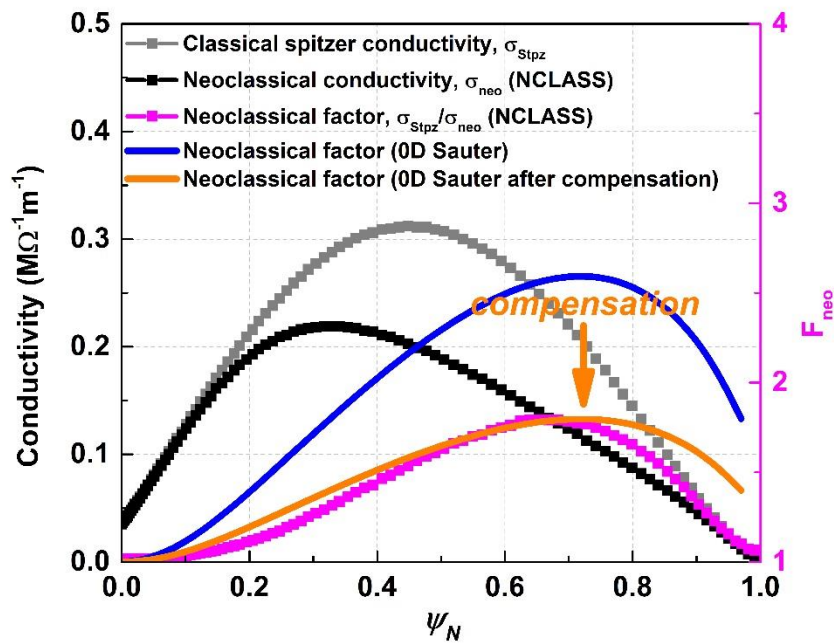


Figure 3.8 Neoclassical enhancement factor: Magneta (NCLASS), blue (0D Sauter) and orange (0D Sauter after compensation using the NCLASS simulation result).

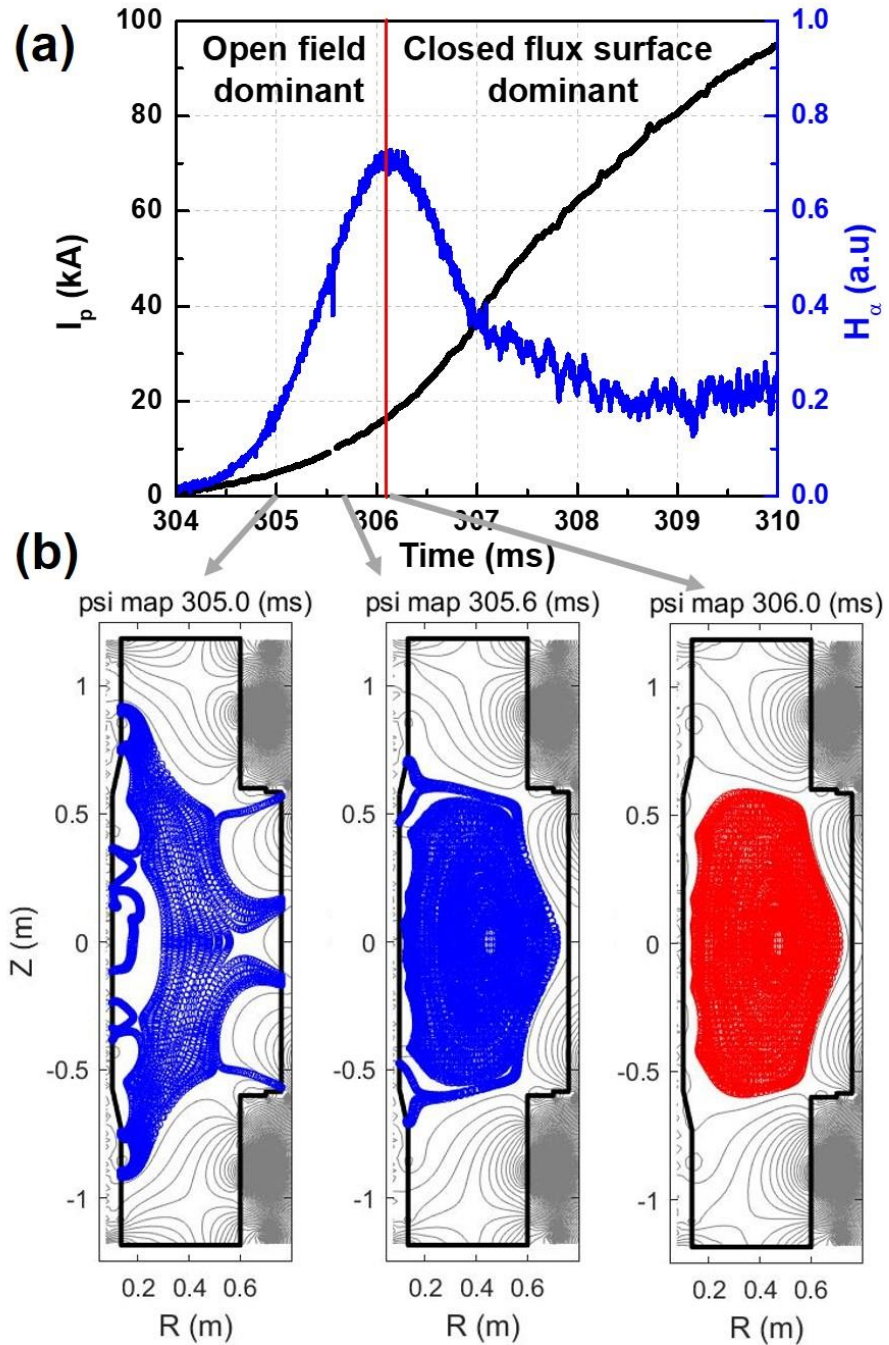


Figure 3.9 Time evolution in (a) the plasma current and H_α line emission signal and (b) the plasma volume structure calculated by the Townsend volume model in the shot#37440.

3.2. Plasma volume model with Townsend criterion [17]

This section focuses on the Townsend volume model for estimation of plasma volume. Townsend breakdown model here is well known criteria which describes a minimum electric field for successful breakdown as a function of neutral pressure and connection length. Townsend volume model utilizes the criterion to determine the plasma volume at early burn-through phase. To determine the criterion quantitatively, several physical quantities such as electric field, neutral pressure and connection length are required. Neutral pressure value is easily obtained from measurement and assumed to be uniform. Then, we need to calculate the electric field and connection length. For these parameters, two-dimensional poloidal magnetic field is needed. The poloidal magnetic flux at the position r from a toroidal ring current source (i.e. PF coils or wall eddy currents) at the position r_0 can be solved directly using Green's function as following:

$$\begin{aligned}\psi(r) &= I_c G(r, r_0) \\ G(r, r_0) &= \frac{\mu_0}{2\pi k} (rr_0)^{1/2} [(2 - k^2)K(k) - 2E(k)]\end{aligned}\tag{3.9}$$

where I_c is a source current, $k^2 = \frac{4rr_0}{(r+r_0)^2+(z-z_0)^2}$, and $K(k)$ and $E(k)$ are the complete elliptical integral of the first kind and complete elliptical integral of the second kind, respectively. With the Green's function, the poloidal magnetic flux can be easily calculated by multiplying the Green's function at given position and source current. The poloidal magnetic field can be calculated from the poloidal magnetic flux using following equations:

$$\begin{aligned}B_r &= -\frac{1}{r} \frac{\partial \psi}{\partial z} = -\frac{I_c}{r} \frac{\partial G(r, r_0)}{\partial z} \\ B_z &= +\frac{1}{r} \frac{\partial \psi}{\partial r} = +\frac{I_c}{r} \frac{\partial G(r, r_0)}{\partial r}\end{aligned}\tag{3.10}$$

Also, induced loop voltage can be expressed in terms of the poloidal magnetic flux as following: $V_{loop} = \frac{d\psi(r,z)}{dt}$ and the toroidal electric field is given by $E_t = \frac{V_{loop}}{2\pi r}$. Using above relations, it is possible to calculate the two-dimensional electromagnetic field with given PF coils and vacuum vessel eddy currents from the full electromagnetic model. Fig. 3.10 shows an example of two-dimensional electromagnetic field from the above relations.

So far, the 2D electromagnetic information is obtained using the Green's function. To evaluate the Townsend breakdown criterion, the connection length should be estimated accurately. Using the field line following method, it is possible to estimate the connection length with given two-dimensional vacuum poloidal magnetic field structure. The field line following method calculates the distance that particles should travel along the magnetic field line until they are lost at the vacuum vessel wall by using following equations:

$$\begin{aligned} R_{k+1} &= R_k + \frac{B_{r,k}}{\sqrt{B_{r,k}^2 + B_{z,k}^2 + B_{\phi,k}^2}} \Delta l \\ Z_{k+1} &= Z_k + \frac{B_{z,k}}{\sqrt{B_{r,k}^2 + B_{z,k}^2 + B_{\phi,k}^2}} \Delta l \end{aligned} \tag{3.11}$$

where (R_k, Z_k) and (R_{k+1}, Z_{k+1}) are k-th and (k+1) th grids, respectively during the field line following process, Δl is a unit length per one step in the field line following process. When the total number of points of field line following process in a field line is N , for open field lines connection length of the field line is calculated to be $L\Delta l$. Also, using the method the averaged electric field parallel to the magnetic field line can be obtained and it can be expressed as:

$$E_{\parallel}(R_k, Z_k) = \frac{B_{\phi,k}}{\sqrt{B_{r,k}^2 + B_{z,k}^2 + B_{\phi,k}^2}} \times E_{\phi}(R_k, Z_k)$$

$$\langle E_{\parallel} \rangle = \frac{\sum_{k=1}^{k=N} E_{\parallel}(R_k, Z_k)}{N} \quad (3.12)$$

For open field lines inside the vacuum vessel, the averaged parallel electric field is compared to the Townsend electric field, $E_{Townsend} = \frac{1.25 \times 10^4 p \text{ (Torr)}}{\ln(510p \text{ (Torr)}) L_{open} \text{ (m)}}$. If the criterion satisfies in a specific field line, then the breakdown can occur in the field line. All the grids which satisfy the Townsend criterion makes a volume and it is defined as the plasma volume in the early burn-through phase or open magnetic field phase.

After formation of the closed flux surface (CFS), the connection length is no longer important parameter because it has infinite value theoretically. Therefore, other approach is necessary for identification of plasma volume (or shape) after the formation of the CFS. There are two methods for identification of plasma shape. First one is a filament method and the other is an element method. According to the recent research which utilize the full electromagnetic plasms start-up code, single filament method reproduces well an ohmic discharge with moderate plasma elongation in MAST [17]. Especially, plasma volume from the volume model is reasonably agreement with the EFIT result. However, it is difficult to simulate an ohmic discharge with high elongation ($\kappa > 2$) using the single filament plasma current assumption. Therefore, advanced method with element current density distribution is developed to identify the plasma shape. In this method, it is assumed that plasma current has a uniform current density. Once a plasma current is calculated from the circuit system equation, it is uniformly distributed in set grid. Then, by solving the elliptical partial derivative equation below, total magnetic poloidal flux which includes PF coils, vacuum vessel eddy currents, and plasma current effect are calculated.

$$\Delta^* \psi = R \frac{\partial}{\partial R} \left(\frac{1}{R} \frac{\partial \psi}{\partial R} \right) + \frac{\partial^2 \psi}{\partial Z^2} = -\mu_0 j_{\phi} \quad (3.13)$$

Finally, plasma shape such as major radius, minor radius and elongation can be easily

obtained by definitions with a given poloidal magnetic flux distribution. Fig.3.11 show the 2D plasma volume evolution in the VEST ohmic discharge using the volume model with different two methods: single filament and finite element methods. There are no significant differences between two methods in the plasma breakdown phase. As the plasma current grows, the plasma volume calculated by two methods begins to be different. The plasma boundary available from the equilibrium reconstruction is plotted with the model result in each case. In the case of the finite element method, the highly elongated plasma is well reproduced. However, the plasma volume model with the single filament method cannot reproduce the plasma shape with high elongation in VEST.

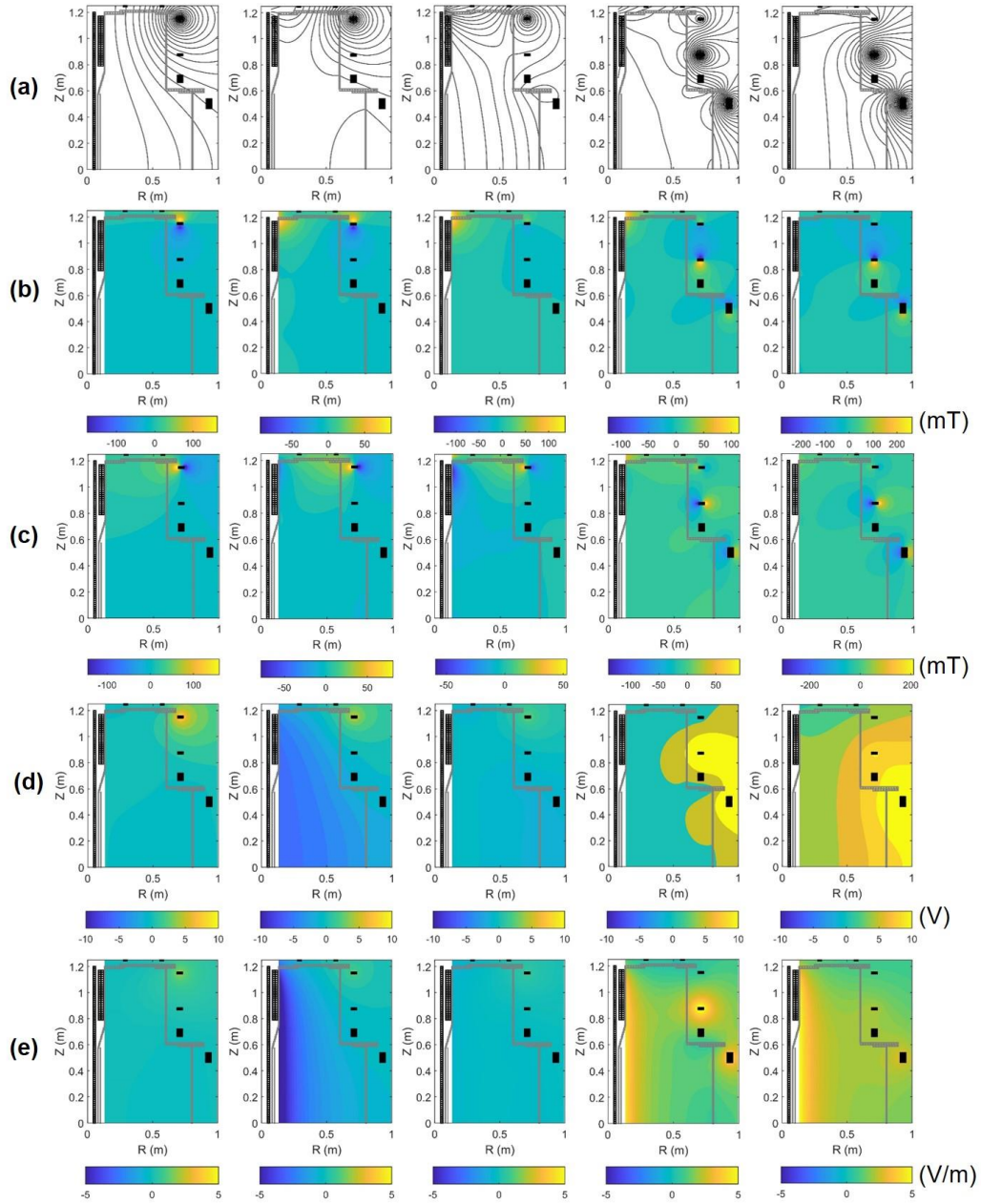


Figure 3.10 Evolution of two-dimensional electromagnetic field using full electromagnetic model (from left to right: 290 – 310 ms). (a) poloidal magnetic flux (b) radial magnetic field (c) vertical magnetic field (d) toroidal loop voltage (e) toroidal electric field.

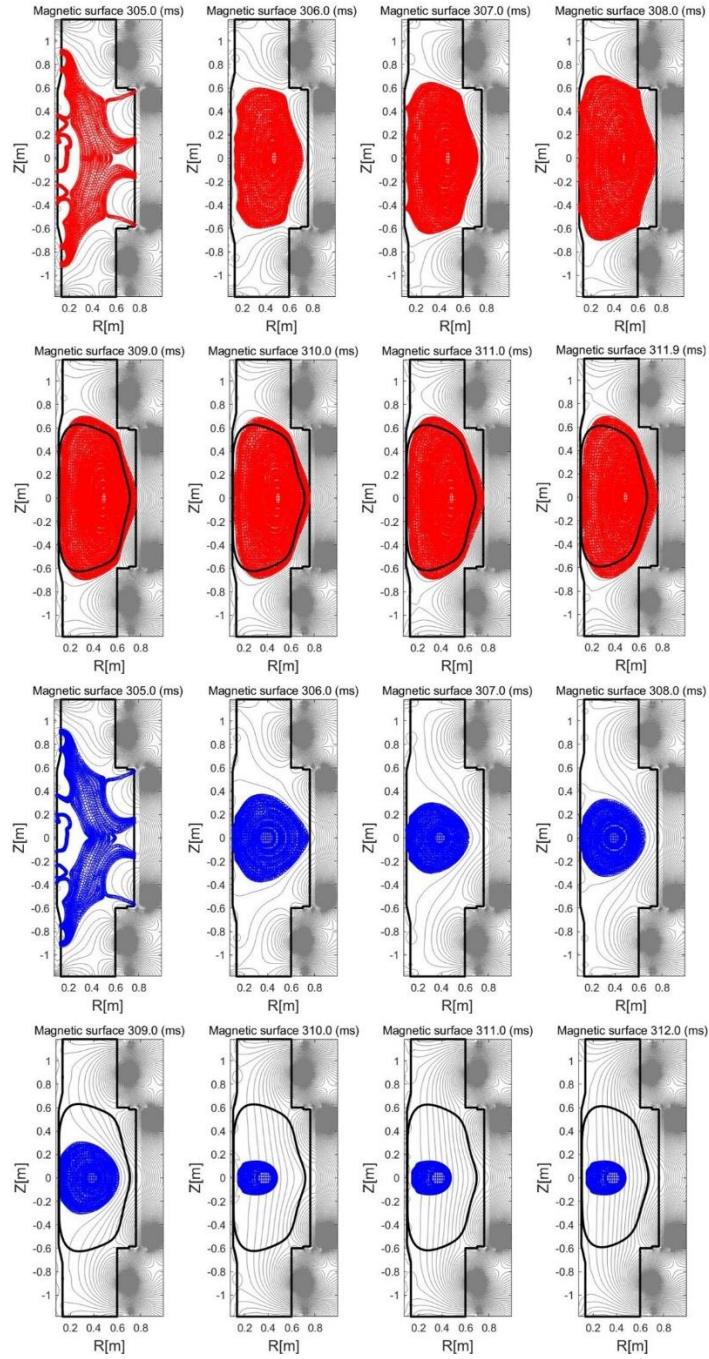


Figure 3.11 Evolution of 2D plasma volume with two methods: red area (finite element method), blue area (single filament) and black line (equilibrium reconstruction).

3.3. Confinement model [12]

In the previous DYON model, the confinement model is established with the assumption that all transport losses are convective. Therefore, the energy confinement time is assumed to be equal to the particle confinement time. In the open field regime, the mechanism of the dominant particle loss is parallel. The confinement time with parallel transport is calculated by dividing the connection length L_f by the ion sound speed C_s , $\tau_{p,\parallel} = L_f/C_s$ where $C_s = \sqrt{\frac{T_e+T_i}{m_i}}$. While perpendicular particle loss can be ignored when L_f is sufficiently short, the perpendicular particle transport becomes dominant as the closed flux surface is formed. In the confinement model at this phase, Bohm diffusion is adopted to calculate the perpendicular particle transport. The Bohm diffusion velocity is expressed as, $v_{Bohm}(t) = \frac{2D_{Bohm}(t)}{a(t)}$ where $D_{Bohm}(t) = \frac{1}{16} \frac{T_e}{B\phi}$. Accordingly, the confinement time due to the perpendicular transport is $\tau_{p,\perp} = a(t)/v_{Bohm}(t)$. The effective confinement time is then obtained by combining two confinement times as, $\frac{1}{\tau_p} = \frac{1}{\tau_{p,\parallel}} + \frac{1}{\tau_{p,\perp}}$. The previous confinement model is adopted for the start-up model in this research. In order to check the validity of the confinement model in VEST ohmic plasma, the effective confinement time between the start-up model and experiments are compared. A set of equations (3.14) is a derivation of the energy confinement time from the power balance equations for obtaining the experimental τ_E .

- Electron power balance: $\frac{3}{2} \frac{d(n_e T_e)}{dt} = P_{oh} - (P_{rad} + P_{iz}) - P_{equi} - P_{trans}^e$
- Ion power balance: $\frac{3}{2} \frac{d(n_i T_i)}{dt} = P_{equi} - P_{CX} - P_{trans}^i$

where P_{oh} is a ohmic heating power, P_{rad} is a radiation power loss, P_{iz} a ionization power loss, P_{equi} is a equilibration power between electron and ion, P_{trans}^e is an electron transport power loss, P_{CX} is a charge exchange loss, and

P_{trans}^i is an ion transport power loss.

- Sum of two balances: $\frac{3}{2} \left(\frac{n_e T_e + n_i T_i}{dt} \right) = P_{oh} - (P_{rad} + P_{iz}) - P_{CX} - \frac{3}{2} \frac{n_e T_e}{\tau_E} -$

$$\frac{3}{2} \frac{n_i T_i}{\tau_E}$$

where $P_{trans}^e = \frac{3}{2} \frac{n_e T_e}{\tau_{Ee}}$ and $P_{trans}^i = \frac{3}{2} \frac{n_i T_i}{\tau_{Ei}}$ with $\tau_{Ee} = \tau_{Ei} = \tau_E$.

- $\frac{dW}{dt} = P_{oh} - (P_{rad} + P_{iz}) - P_{CX} - \frac{W}{\tau_E}$ where $W = \frac{3}{2} (n_e T_e + n_i T_i)$.

- $\tau_E = \frac{W}{P_{oh} - (P_{rad} + P_{iz}) - P_{CX} - dW/dt}$ (3.14)

In τ_E , the ohmic heating power, P_{oh} and stored energy, W can be obtained experimentally by the plasma current and kinetic measurements such as Thomson scattering in VEST. However, it is difficult to obtain other power losses including the ionization, radiation and charge exchange power losses experimentally in VEST. Therefore, sum of other power losses is scanned with ratio of the ohmic heating power. Fig.3.12 is a result of time evolution in τ_E from the model and experiment. According to this result, when the ratio of the ohmic heating power and power losses is between 50 % and 75 %, τ_E from the experiment agrees with the simulation result. As shown in Fig.3.12 (b), the ratio from the simulation is between 50 % and 75 %. Therefore, it is confirmed that the confinement model with convective loss can be applied in VEST ohmic discharges.

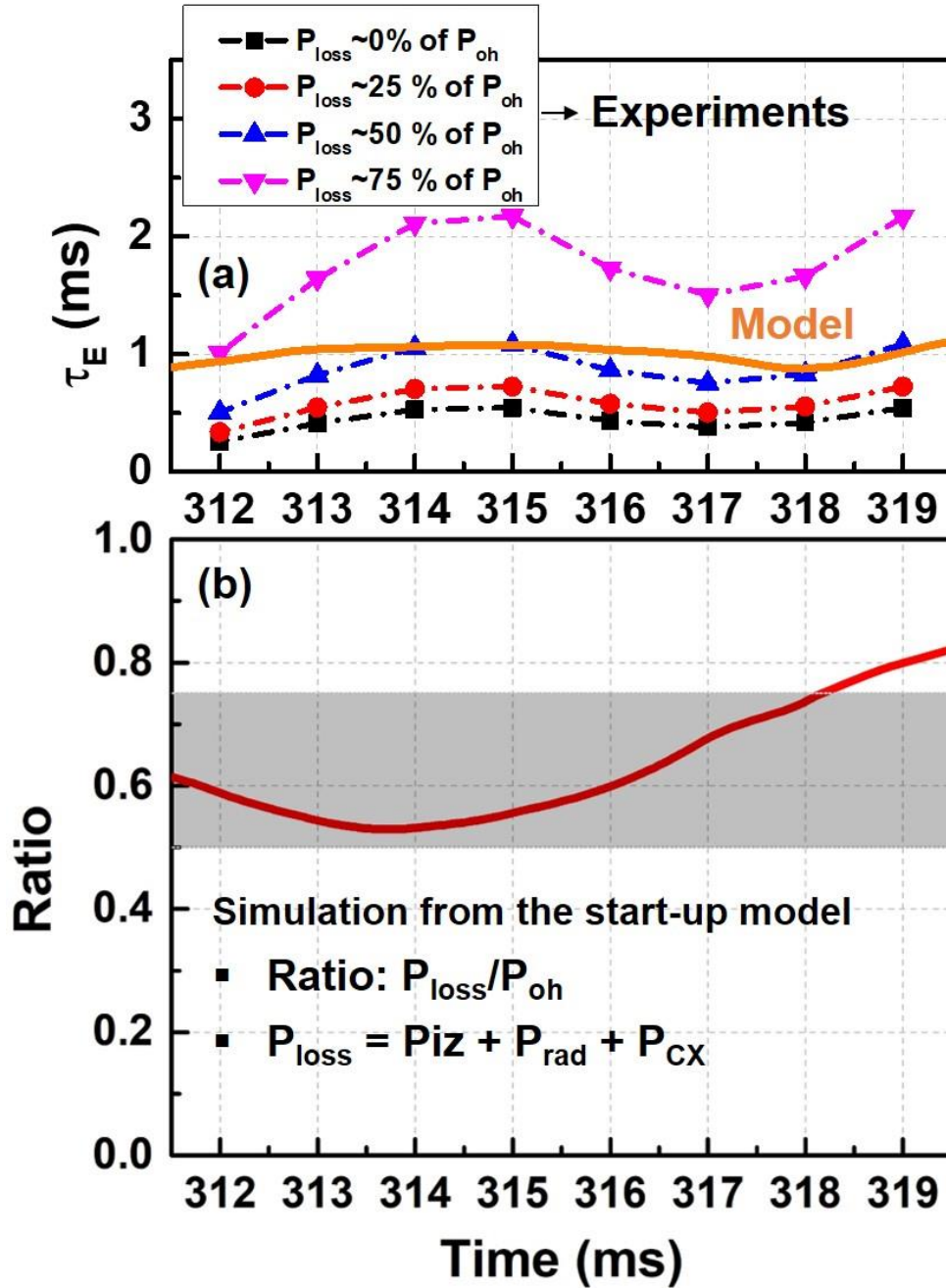


Figure 3.12 Time evolution in (a) the energy confinement time from the experiment (orange line) and model (marked lines) and (b) the ratio of the ohmic heating power and power losses from the model (red line).

3.4. Plasma wall interaction model

In the plasma start-up phase, plasma size expands and plasma current ramps-up after successful formation of closed flux surface. Typically, in early plasma start-up phase, plasma is operated with limited formation. This means that plasma touches limiters or vacuum vessel wall and impurity can flow in the main plasma due to the plasma wall interactions. VEST plasma is mainly operated in limited formation and this effect should be considered in the plasma start-up model. In this section, plasma wall interaction part in the model is described in detail.

The main impurity source is carbon and oxygen on the centerstack. In real situation, both impurities exist and it is observed that line radiation signal related to the carbon and oxygen occurs when the plasma touches the centerstack. However, it is difficult to estimate the ratio of oxygen and carbon impurity quantitatively. Therefore, for simplicity, impurity due to the wall interaction is assumed to be only the carbon. Because the carbon sputtering yield by the hydrogen is a parameter for which it is difficult to quantify, calculation with scan is needed. The carbon sputtering yield is set to be constant in time in each case in order to set the proper sputtering yield in VEST. Fig.3.13 shows the time evolution in the plasma current, the electron temperature and density with each case. In the VEST ohmic discharge, the carbon sputtering yield by hydrogen ion with 0.1 is thought to be a proper value. Based on the value obtained from the test results as shown in Fig.3.13, the carbon sputtering yield input is set with a waveform similar to the time evolution in the CIII line emission signal observed in the VEST ohmic discharge.

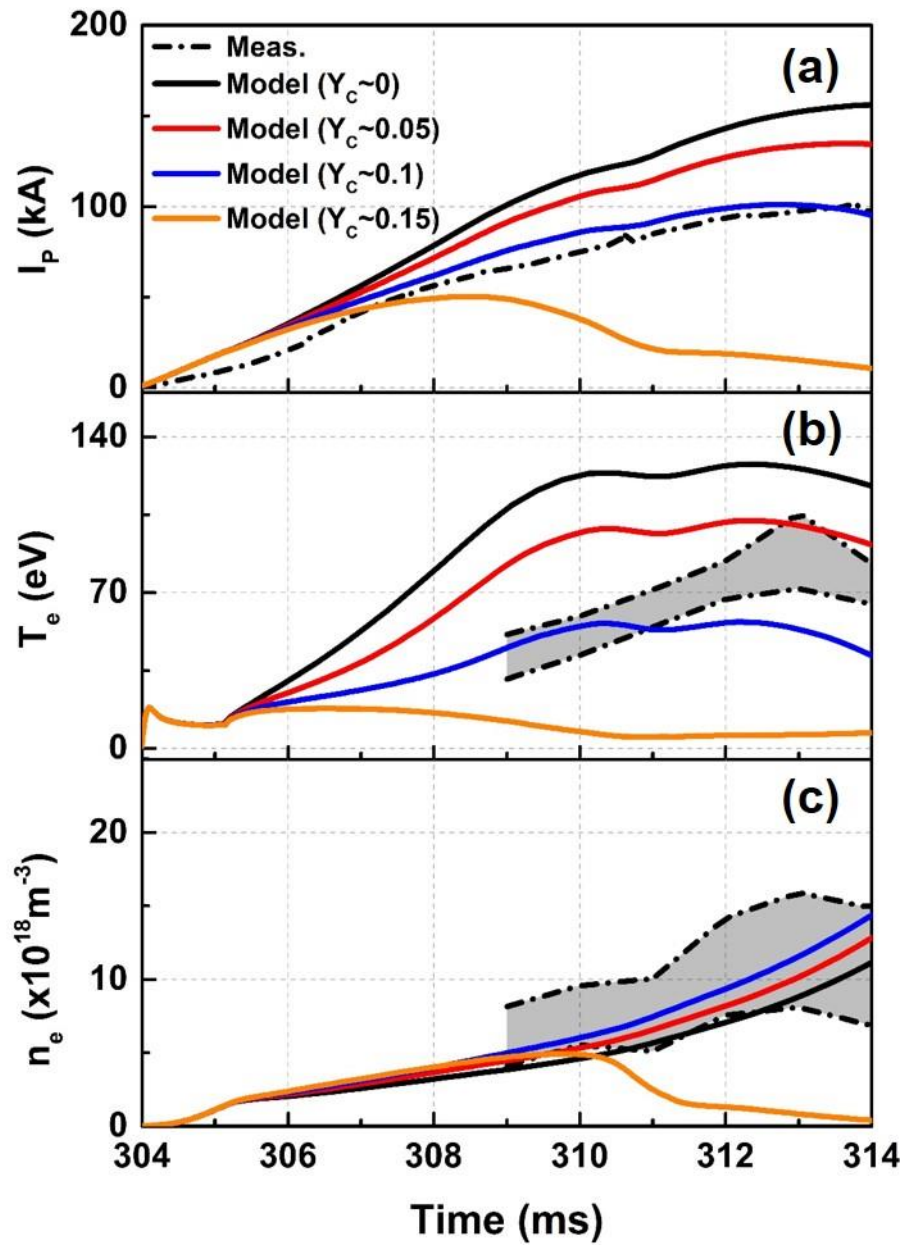


Figure 3.13 Time evolution in (a) the plasma current from the experiment (black dash-dot) and model (lines), (b) the electron temperature from the experiment (shaded region) and model (lines) and (c) the electron density from the experiment (shaded region) and model (lines).

Chapter 4. Model Validation and Prediction of Ohmic Discharges in Spherical Torus Devices

So far the full electromagnetic start-up model is described at chapter 3. The full electromagnetic model which solves circuit system equations with given PF coils and vacuum vessel structure enables to obtain exact loop voltage at plasma center position. To consider the finite aspect ratio effect, plasma self-inductance and resistivity models are improved. Plasma shape information such as plasma volume, major radius and elongation can be estimated in both before and after the closed flux surface formation by developing the Townsend breakdown model. In addition to main models as mentioned above, several sub-models such as confinement model and plasma wall interaction model are carefully checked for application to the ohmic discharges in VEST.

In this chapter, the start-up model validation and prediction of ohmic discharges in spherical torus devices are described. Firstly, burn-through regime in VEST ohmic plasma is determined using the start-up model and this regime is compared to experiments. Detailed evolution parameters such as plasma current, electron temperature & density and filter-scope data (H_α and $CIII$) from the start-up model are also validated in different operational conditions: (1) Central solenoid current waveform, (2) outer PF coil current waveform and (3) wall conditioning methods. After confirming the validity of the start-up model in VEST, ohmic discharges are predicted for VEST-Upgrade by changing several input parameters such as ohmic solenoid coil waveform, prefill pressure and wall sputtering yields (or recycling coefficients). The full electromagnetic start-up model is applied to not only the compact ST device, VEST but also mid- and large size ST devices, MAST and STEP.

4.1. Identification of burn-through regime in VEST

4.1.1. Experimental operation window in E -field and prefill pressure

A set of experiments aimed at determining the operational window of burn-through has been performed in VEST. Ohmic discharges are conducted without pre-ionization procedure (i.e. pure ohmic discharge), in which there are two main operating conditions: loop voltage and prefill pressure. Additionally, outer PF coil currents for equilibrium field are adjusted to control the plasma center position. There are two different ohmic discharges in terms of burn-through success or fail as shown in Fig 4.1. In each ohmic discharge, evolutions of plasma current and three different line emission signals (H_{α} , OII and $CIII$) from filterscope are showed. In first ohmic discharge, a peak in the H_{α} line emission signal near 306 ms is clearly shown, which means successful burn-through of hydrogen neutrals. Although it is not a clear peaked signal as observed in the H_{α} line emission signal, impurities burn-through in OII and $CIII$ line emission signals are seen near 307 ms. With these peaked signals in line emission, plasma current rise normally. Increase in line emission signals during the plasma current rise are mainly caused by the plasma wall interactions. Therefore, discharge features in this phase are far from the burn-through. The ohmic discharge as mentioned is a burn-through success case. The other ohmic discharge as shown in Fig 4.1 is a burn-through fail case. In the case of burn-through fail, simultaneous collapses in both plasma current and line emission signals are observed. It is indicated that radiation barrier isn't overcome in this case. Typically, discharges under the low loop voltage or significant prefill pressure have such discharge features.

Recent several tens of ohmic discharges in VEST are classified in terms of burn-through success or fail based on two discharges as shown in Fig 4.1. Each discharge is plotted with the Townsend breakdown curve in 2-D space which is composed of electric

field and prefill pressure as shown in Fig 4.2. Two breakdown curves are obtained using conventional Townsend breakdown criterion and are compensated with consideration of self-generated electric field by producing a proportional coefficient (~ 4) [16]. Each breakdown curve corresponds to connection length of 150 m and 200 m, respectively. There are three different markers in 2-D space: (1) burn-through success, (2) burn-through fail and (3) breakdown fail. In breakdown fail cases, there are no plasma current and line emission signals. It is observed that plasma breakdown doesn't occur in the prefill pressure under the 3 mPa. In the 2-D space, a boundary between the burn-through success and fail regions is seen. In the section 4.1.2, simulations with the start-up model are conducted to reproduce the burn-through region observed in experiments.

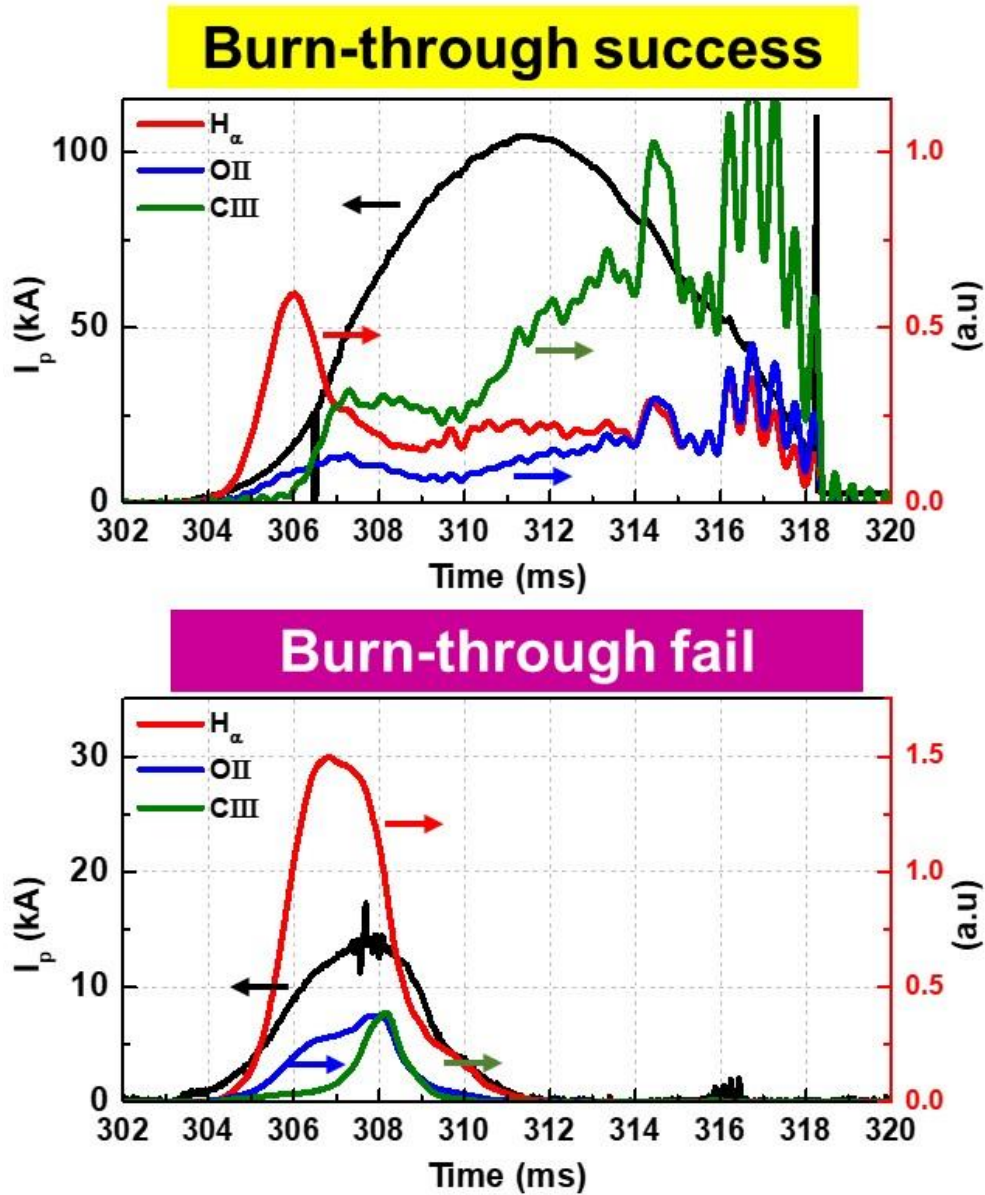


Figure 4.1. Time evolution in the plasma current and filterscope signals (H_α , OII and CIII) at the burn-through success (up) and fail (down) cases.

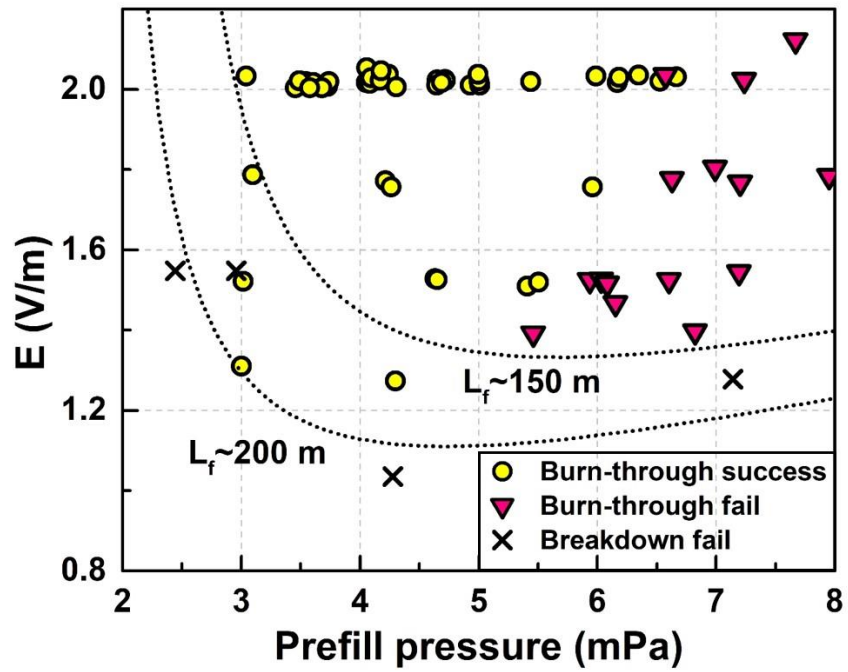


Figure 4.2 Scattered points representing the burn-through success (yellow circle), fail (red upper triangle) and the plasma breakdown fail (black cross) with the Townsend breakdown curve in electric field and prefill pressure space.

4.1.2. Reproduction of burn-through region using the start-up model

Three different lines which divide the region of burn-through success or fail are obtained using the start-up model as shown in Fig 4.3. Input parameters for the start-up model such as plasma shape and wall recycling coefficients are same in all cases except for the PF coil current scenario and prefill pressure. Inputs for PF coil current scenario and neutral pressure are set consistently in operational condition of each ohmic discharge. And initial oxygen atom density is varied with three cases: 0 %, 1 % and 5 %. Simulation result in 5 % initial oxygen atom density doesn't reproduce the experiments and this value is thought to be too large. The 1 % initial oxygen atom density case divides well the burn-through region which is observed in experiments. Oxygen impurity exists in the form of carbon monoxide (CO) and water (H₂O) in VEST. Partial pressure in water is about 1×10^{-6} Torr in RGA measurement [11] as shown in Fig 4.4. Even though partial pressure in carbon monoxide isn't in Fig 4.4, it is empirically known that it exists in similar ratio of water. Therefore, 1 % oxygen atom density in the start-up model is reasonable setting based on the RGA measurement in VEST.

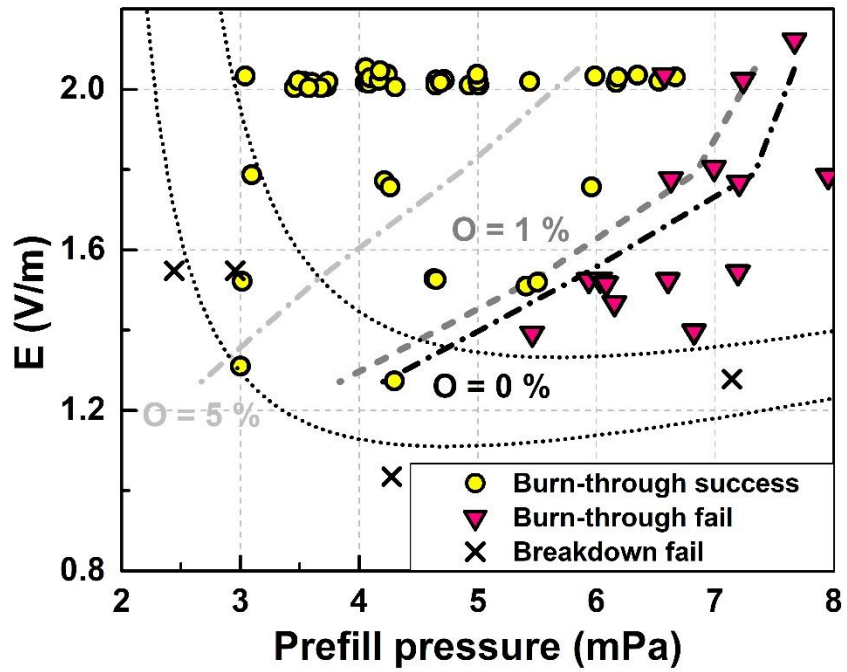


Figure 4.3 Burn-through line obtained by the model with Fig.4.2.

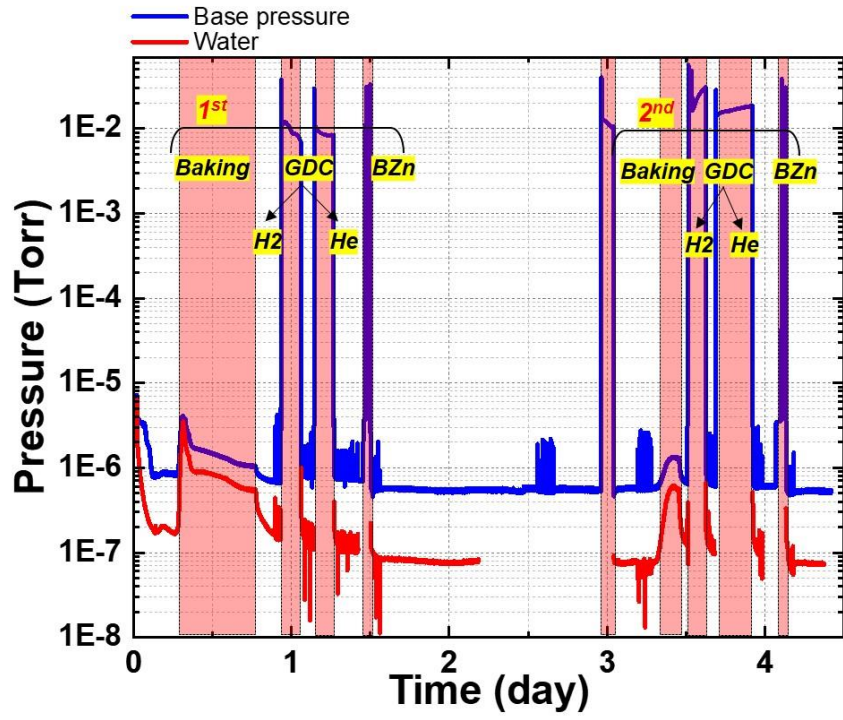


Figure 4.4 Base pressure and partial pressure of water measured by Residual Gas Analyzer (RGA).

4.2. Time evolution of plasma parameters in ohmic discharges with different operational conditions

So far, determination of burn-through is conducted using the start-up model and the start-up model well reproduces the burn-through region observed in experiments. In this section, reproduction in detailed evolution parameters such as plasma current, electron temperature & density and filter-scope data (H_α and $CIII$) using the start-up model are described with several operational conditions: (1) Central solenoid current waveform, (2) outer PF coil current waveform and (3) wall conditioning methods. The central solenoid current waveform determines the loop voltage waveform, which has a significant impact on the plasma current evolution. Outer PF coil current waveform also affects the loop voltage waveform. However, rather than the loop voltage waveform, it has a significant impact on the evolution of plasma shape such as major radius and elongation. Final operational conditions, wall conditioning methods, is related to the plasma wall interactions. Detailed description is given in each section.

4.2.1. Ohmic discharges with different central solenoid currents

Two ohmic discharges with different central solenoid current waveforms are conducted in VEST. Operation conditions in both ohmic discharges are shown in Fig 4.5. As mentioned above, the main difference between two discharges is the central solenoid current waveforms. As a result, the loop voltage induced by the central solenoid has a different waveform in each case. In the shot#37919, maximum loop voltage at machine center (~ 0.4 m) is about 7 V and loop voltage with positive region is about 17 ms as shown in Fig 4.5(b). In the other case, maximum loop voltage is slightly lower than in the case of shot#37919. However, it lasts for ~ 30 ms. Other PF coil current scenarios are adjusted because plasma breakdown and achieved plasma current are different due to the different loop voltage waveform. Time evolution of prefill neutral pressure is almost identical in both cases as shown in Fig 4.5(c).

Figure 4.6 show the ohmic discharge features in discharges with different central solenoid current waveforms. In the shot#37919, the plasma breakdown occurs at 303 ms and there are burn-through and plasma current rise after the plasma breakdown. Plasma current of ~ 100 kA is achieved and it decreases after the peak near 314 ms. There are several reasons for the plasma current evolution without flat-top. It is thought that main two reasons are the excessive equilibrium field by outer PF coils and impurity influxes due to the plasma wall interactions with the inboard centerstack. Several spike signals in plasma current and filterscope signals are observed [43, 44]. These are kinds of MHD activity called the internal reconnection event (IRE) which occurs frequently in spherical tori [45-47]. This phenomenon doesn't affect significantly the global tendency in overall discharge. Electron temperature and density increases in time even during the ramp-down phase. This feature in electron's kinetic property are not investigated in detail. However, the compression heating is thought to be one of the reasons for the continuous increase in electron temperature and density. In the shot#37970, plasma breakdown occurs later than

in the shot#37919 due to the lower loop voltage. Rather than in the shot#37919, plasma current evolution has a flat-top like region during ~ 20 ms. The overall levels of H_α and OII line emission are similar in both ohmic discharge. CIII line emission signal is larger in the shot#37970 than in the shot#37919 and it indicates that there are more plasma wall interactions in the shot#37970. Electron temperature and density do not change significantly in time as shown in Fig 4.5(b). several experimental measurements such as plasma current, electron temperature & density, filterscope signals (H_α and CIII) are utilized for the start-up model validation.

Fig.4.7 and Fig.4.8 show the model results in the shot#37919 and 37970, respectively. In both results, the start-up model well reproduces the overall plasma current evolution. Also, H_α line emission peak in the model agrees with the experiment. It indicates that neutral particle model related to the prefill pressure works well. In both cases, there is a tendency that the electron temperature evolution after the growth of plasma current in the model is different from the one observed in the experiment. In several discharges of VEST, the electron temperature tends to increase even though the plasma current decreases. Although it has not yet been identified in detail, compression heating affects this result. Electron density evolution is well reproduced in both cases. But in the shot#37970, the model underestimates the absolute value in the electron density. Even though the time evolution in CIII line emission is quite different, it doesn't affect the plasma current significantly.

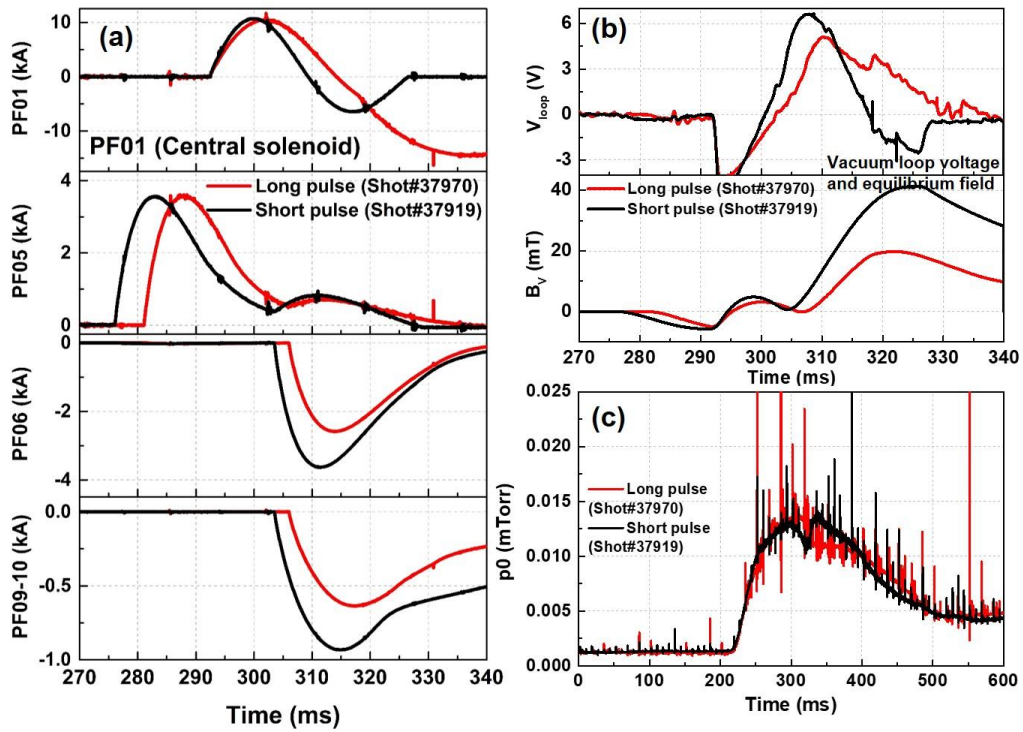


Figure 4.5 Operational conditions in the shot#37970 and 37919: (a) PF coil current waveforms, (b) loop voltage and equilibrium field at machine center, and (c) neutral pressure evolutions.

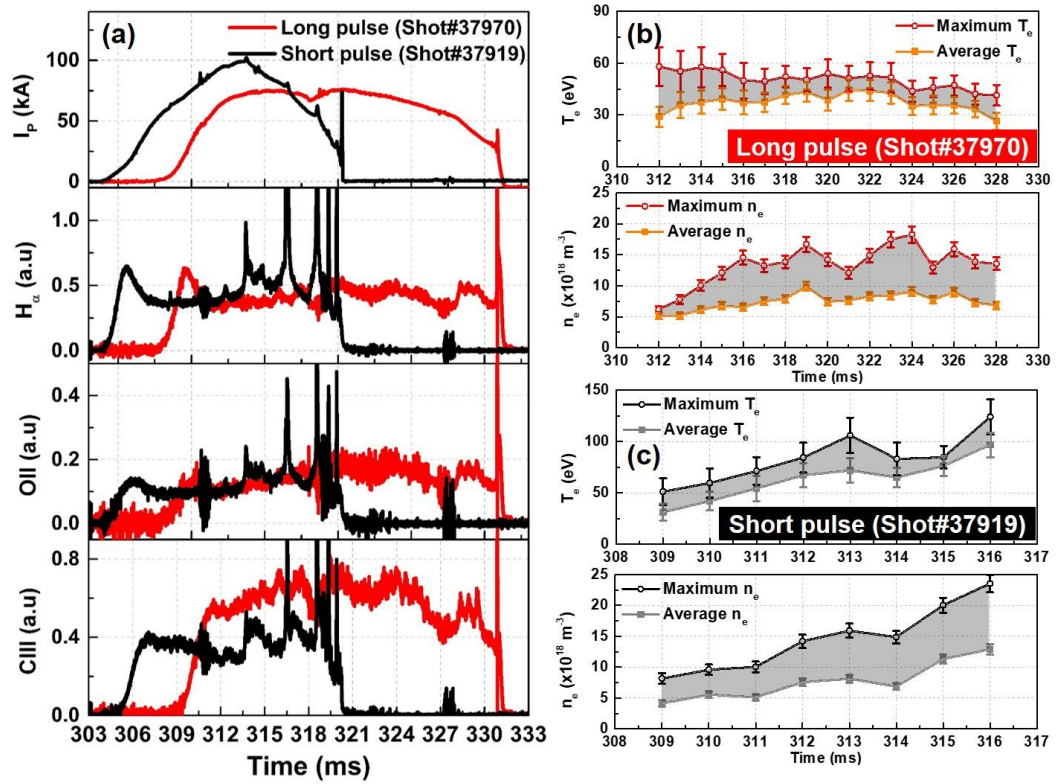


Figure 4.6 Features of ohmic discharges in the shot#37970 and 37919: (a) plasma current and filterscope signals (H_α , OII and CIII), electron temperature and density evolutions (b) in the shot#37970 and (c) in the shot#37919.

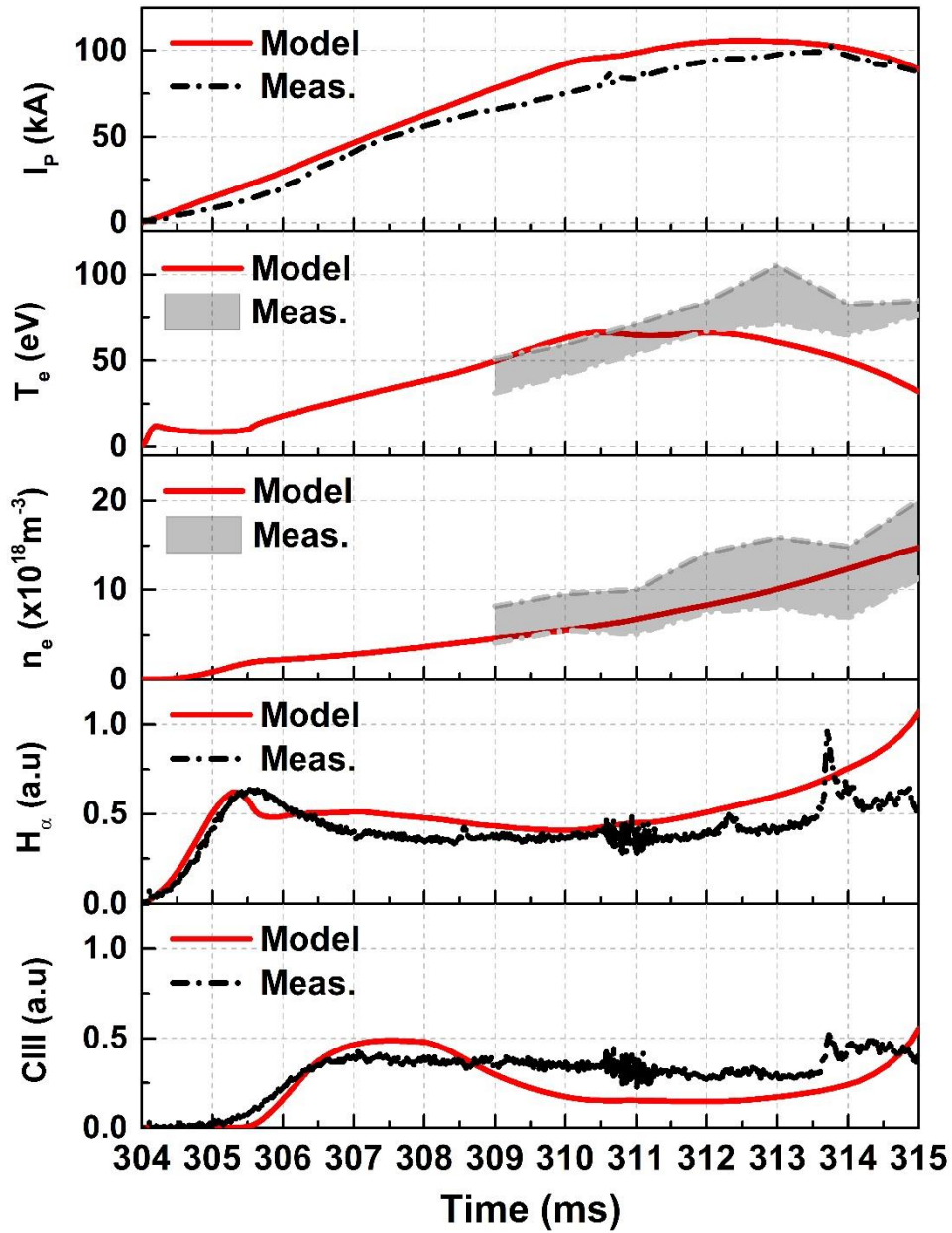


Figure 4.7 Time evolution in (from up to down): plasma current, electron temperature, electron, electron density, H_{α} line emission signal and CIII line emission signal from the model (red) and experiment (black and grey) in the shot#37919.

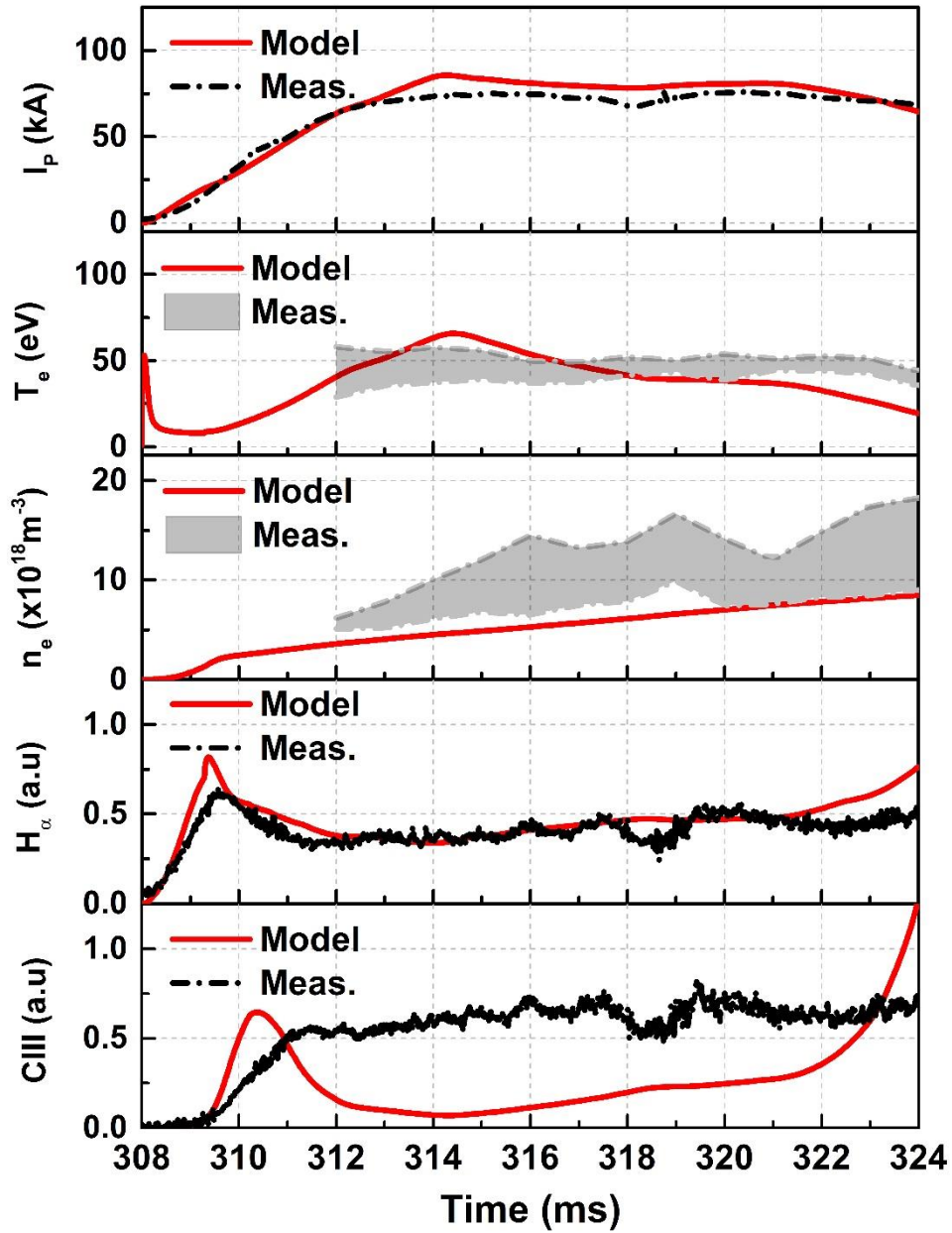


Figure 4.8 Time evolution in (from up to down): plasma current, electron temperature, electron density, H_α line emission signal and CIII line emission signal from the model (red) and experiment (black and grey) in the shot#37970.

4.2.2. Ohmic discharges with different outer PF coil currents

In this section, the start-up model is applied to the ohmic discharges with different PF coil current waveforms. Operational conditions are shown in Fig 4.8. The central solenoid current waveforms are identical in three cases: shot#37440, 37441 and 37442. Outer PF coil currents are different as shown in Fig 4.8(a). Vacuum loop voltage at machine center is almost same due to the identical central solenoid current waveforms. Even though the loop voltages in three cases are slightly different because the outer PF coil currents contribute to the loop voltage waveform, it doesn't have significant impact on the plasma current evolution. As shown in Fig 4.8(c), evolutions of prefill pressure are almost identical in three cases. There is a little difference in the prefill pressure evolution after 350 ms and it is discussed with the results of ohmic discharges in three cases.

Figure 4.8 show the ohmic discharge features in discharges with different PF coil current waveforms. In the early start-up phase before ~306 ms, overall discharge features are almost similar in three cases. After ~306 ms, differences in discharge features begin to occur. In the strong equilibrium field case (shot#37442), impurity line emission signals (OII and CIII) increase rapidly and it indicates that inboard limited plasma is formed early. In the medium and weak equilibrium field discharges (shot#37440 and 37441), difference in impurity line emission signals occurs near the 310 ms. After 312 ms, impurity line emission signals rapidly jump due to the plasma wall interactions with inboard centerstack in the weak equilibrium field case. In all discharges, there are IRE events during the ramp-down phase. Fluctuation tendency in electron density measurements as shown in Fig. 4.9 (b) – (d) is thought to be caused by the IRE events [33]. Fig. 4.10 and Fig. 4.11 are the major radius & outboard limiter signals and fast camera images in three discharges, respectively. Three limiter segments with connected to the electrical ground are located near the outboard vacuum vessel wall. Measured currents flowing through the limiter segments represent the interactions between the plasma and the outer limiter segments.

There are no significant differences in lower and upper limiter current signals as shown in Fig.4.9 (c) and Fig.4.9 (e) among the three cases. However, current signal flowing through mid-outer limiter indicates the difference of outboard wall interactions in three cases. In the weak equilibrium field case (shot#37440), the largest current at mid-outer limiter is observed as shown in Fig.4.9 (d). Also, major radius evolution from the magnetic equilibrium reconstruction shows the consistent results. In addition to the filterscope measurements, fast camera image with CIII filter also indicates the plasma wall interactions with inboard centerstack. For example, bright region observed near the centerstack at 314 ms frame in the weak equilibrium field case is measured due to the plasma wall interactions with the inboard centerstack. It can be seen that the stronger the equilibrium field by PF coils, the faster the bright region near the inboard centerstack occurs. There is also an indirect indication for the plasma wall interactions in prefill pressure evolution as mentioned in Fig.4.8 (c). Even though there is a time response in neutral pressure gauge installed in VEST, the neutral pressure in the strong equilibrium field case increases significantly compared to the other two cases after the minimum pressure. This increase in neutral pressure is mainly caused by the plasma wall interactions. All the experimental data presented in this section can be consistent results. Mainly two different effect, major radius and impurity influx due to the plasma wall interactions, are properly considered for the start-up model validation in ohmic discharges with different outer PF coil currents.

Fig.4.13, Fig.4.14 and Fig.4.15 show the model results in the shot#37440, 37441, and 37442, respectively. In the case of shot#37440, the model reproduces the plasma current evolution well. Especially, the plasma growth delay during 306-308 ms is observed in both the model and experiment. In this range, plasma has small size with outboard limited operation. It is difficult for the plasma current rise due to the higher plasma external inductance during this phase. Other parameters such as electron

temperature, electron density and filterscope signals are agreement with the experimental data. In the case of shot#37441, all parameters are reproduced with reasonable level. In the last case with strongest vertical field, there is a discrepancy between the model and experiment after 310 ms. Even though a single IRE burst does not have a significant impact on the overall evolution, sequential IRE can affect the overall evolution. It is observed that IREs occur continuously in the case of shot#37442. Therefore, the discrepancy during this phase is thought to be caused by the sequential MHD activities. An ohmic discharge less affected by IREs is required in order to investigate only the effect of vertical field strength by PF coil.

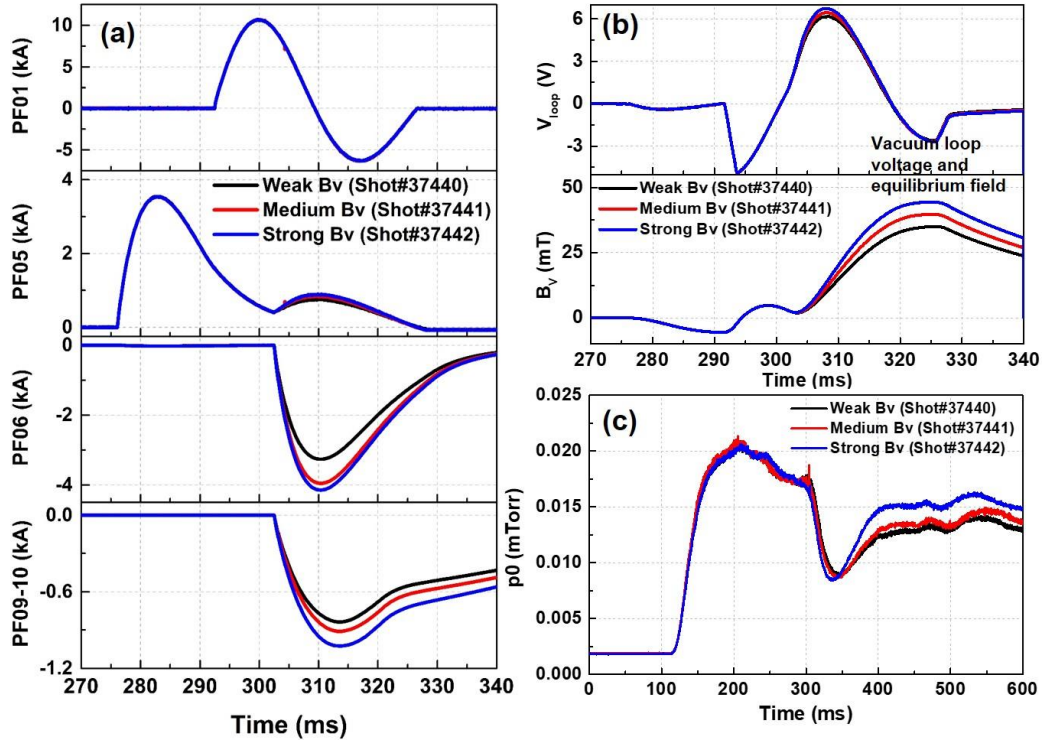


Figure 4.9 Operational conditions in the shot#37440, 37441 and 37442: (a) PF coil current waveforms, (b) loop voltage and equilibrium field at machine center, and (c) neutral pressure evolutions.

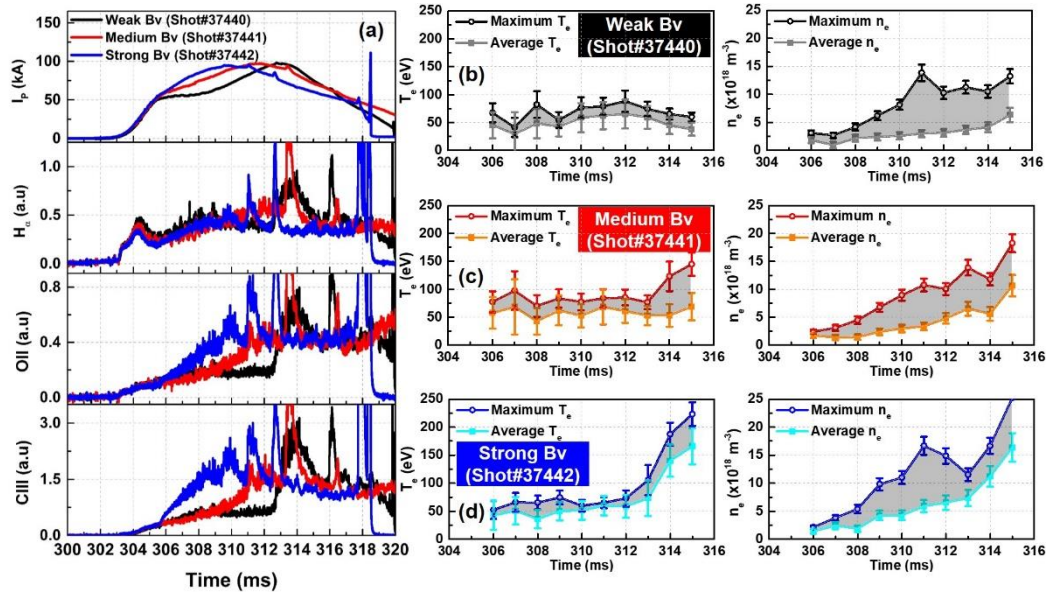


Figure 4.10 Features of ohmic discharges in the shot#37440, 37441 and 37442: (a) plasma current and filterscope signals (H_α , OII and CIII), electron temperature and density evolutions (b) in the shot#37440, (c) in the shot#37441 and (d) in the shot#37442.

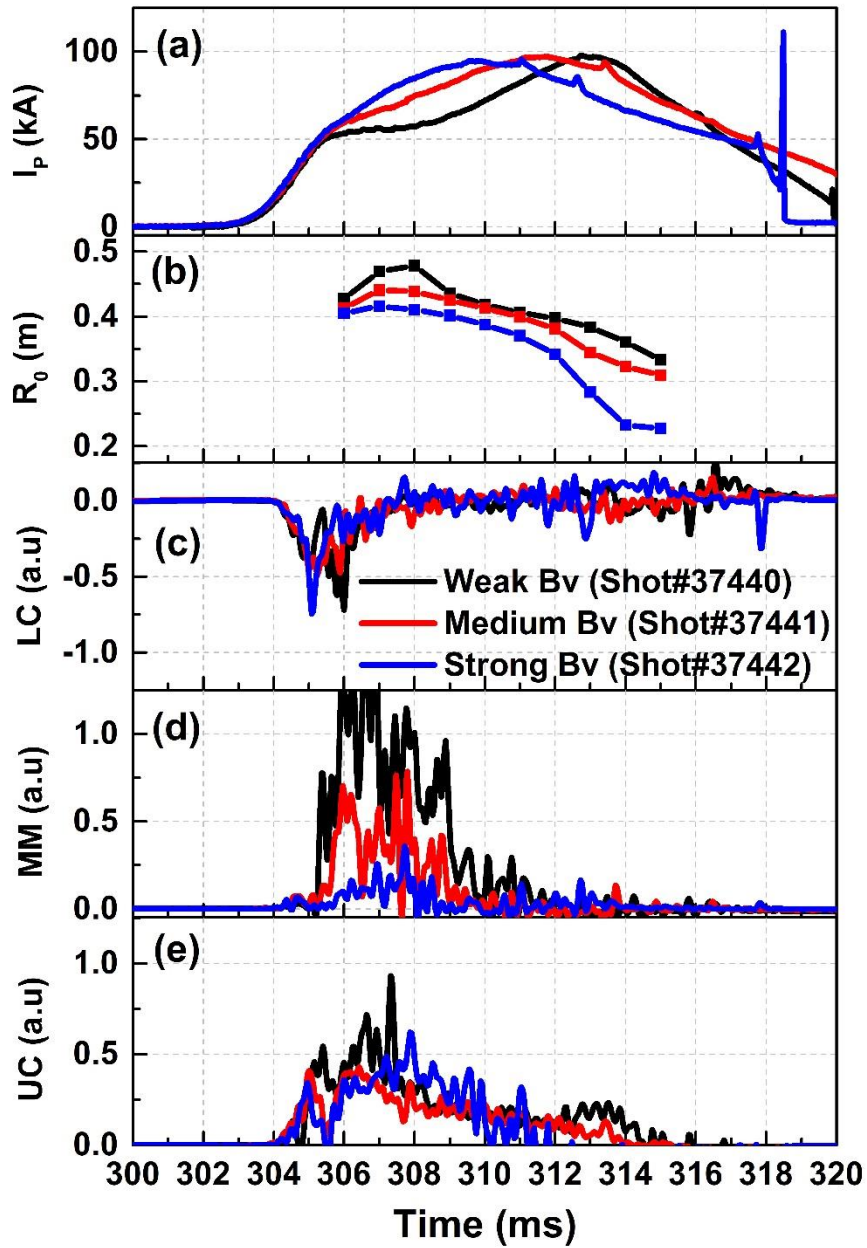


Figure 4.3 Evolution in (a) plasma current, (b) major radius, (c) lower limiter current, (d) mid-limiter current, and (e) upper limiter current in the shot#37440, 37441, and 37442.

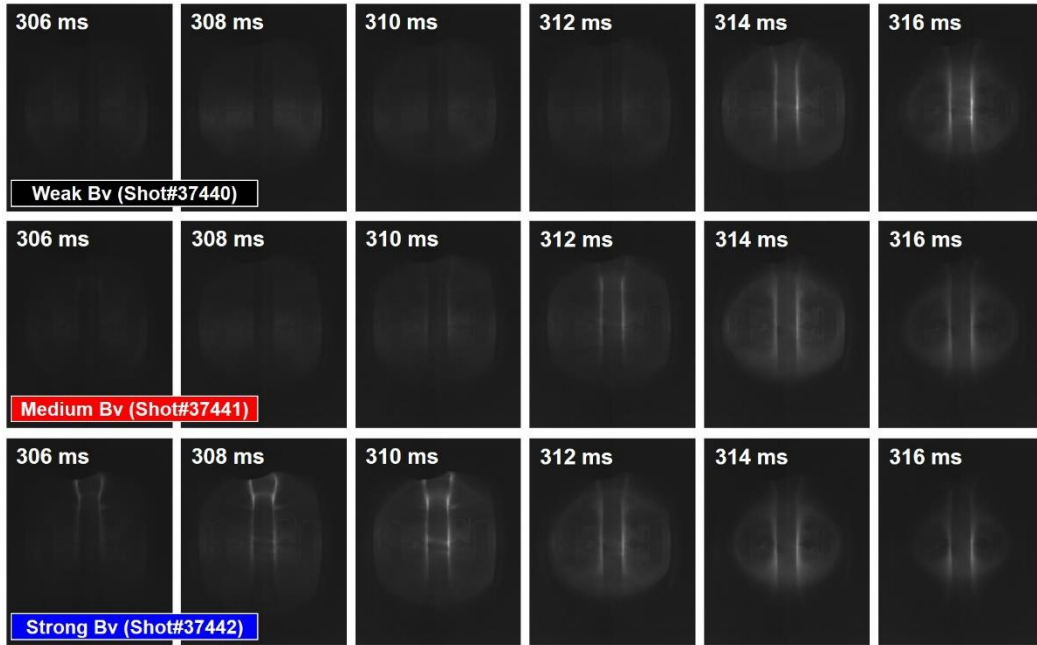


Figure 4.4 CIII filtered fast camera images in the shot#37440, 37441, and 37442.

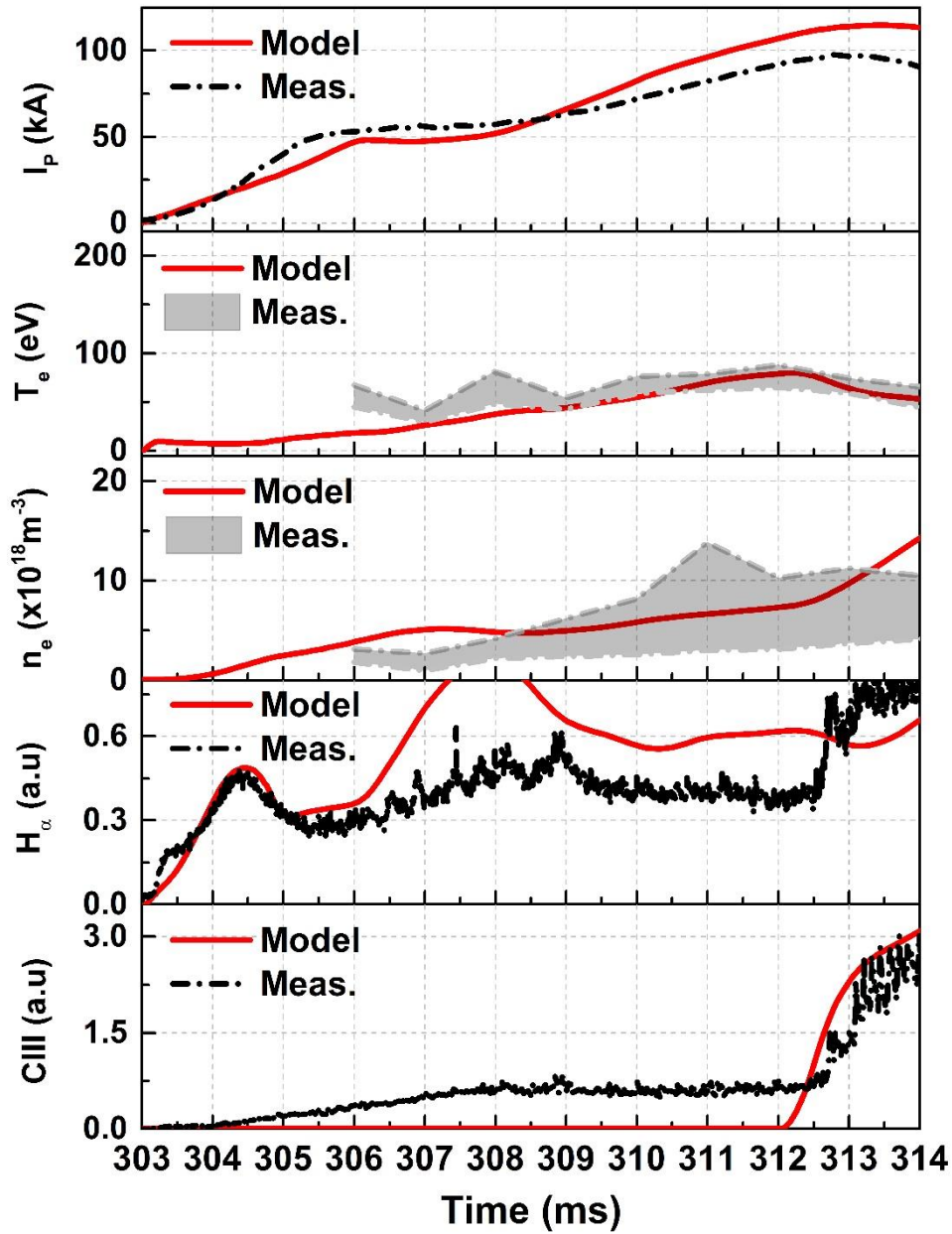


Figure 4.13 Time evolution in (from up to down): plasma current, electron temperature, electron density, H_{α} line emission signal and CIII line emission signal from the model (red) and experiment (black and grey) in the shot#37440.

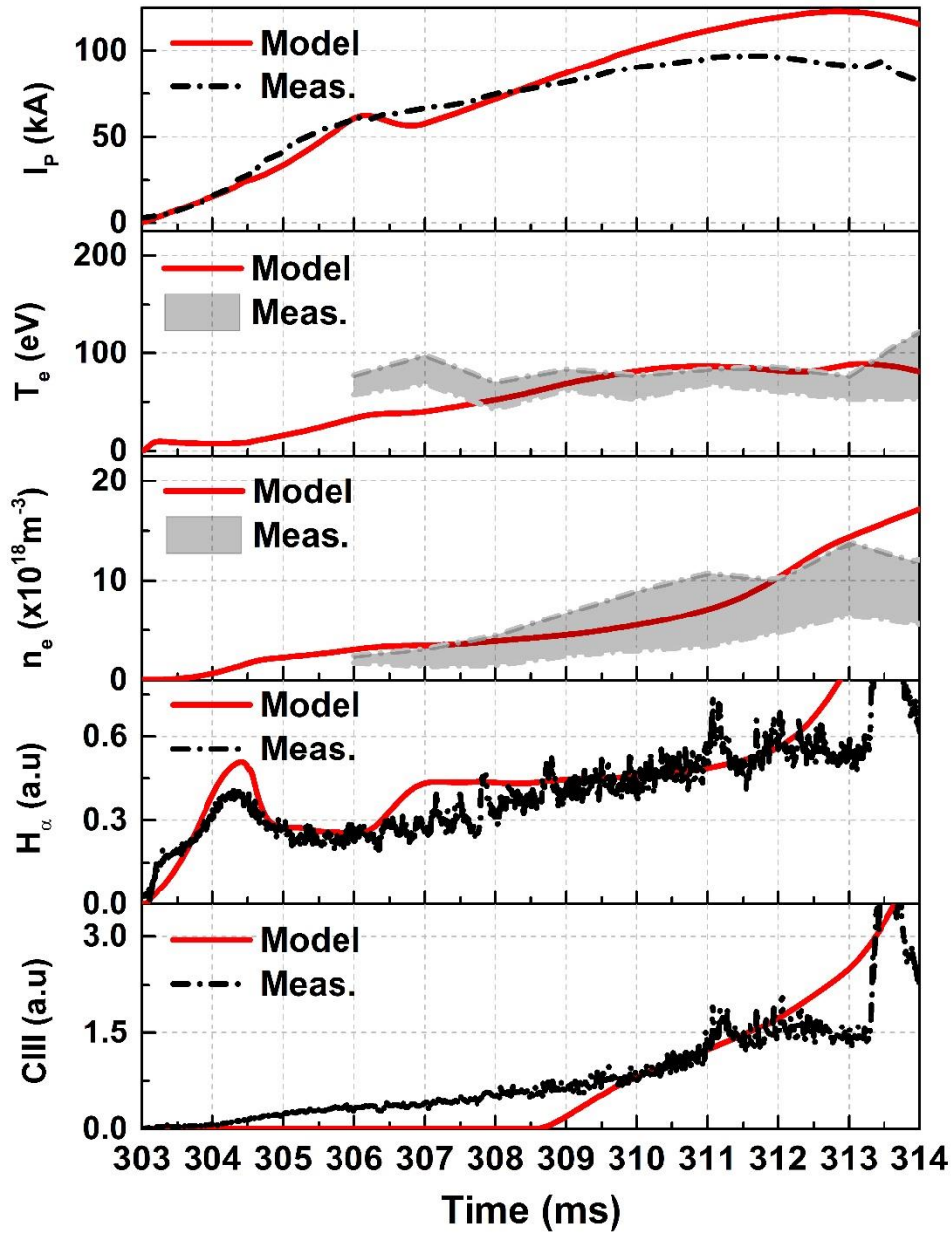


Figure 4.14 Time evolution in (from up to down): plasma current, electron temperature, electron density, H_{α} line emission signal and CIII line emission signal from the model (red) and experiment (black and grey) in the shot#37441.

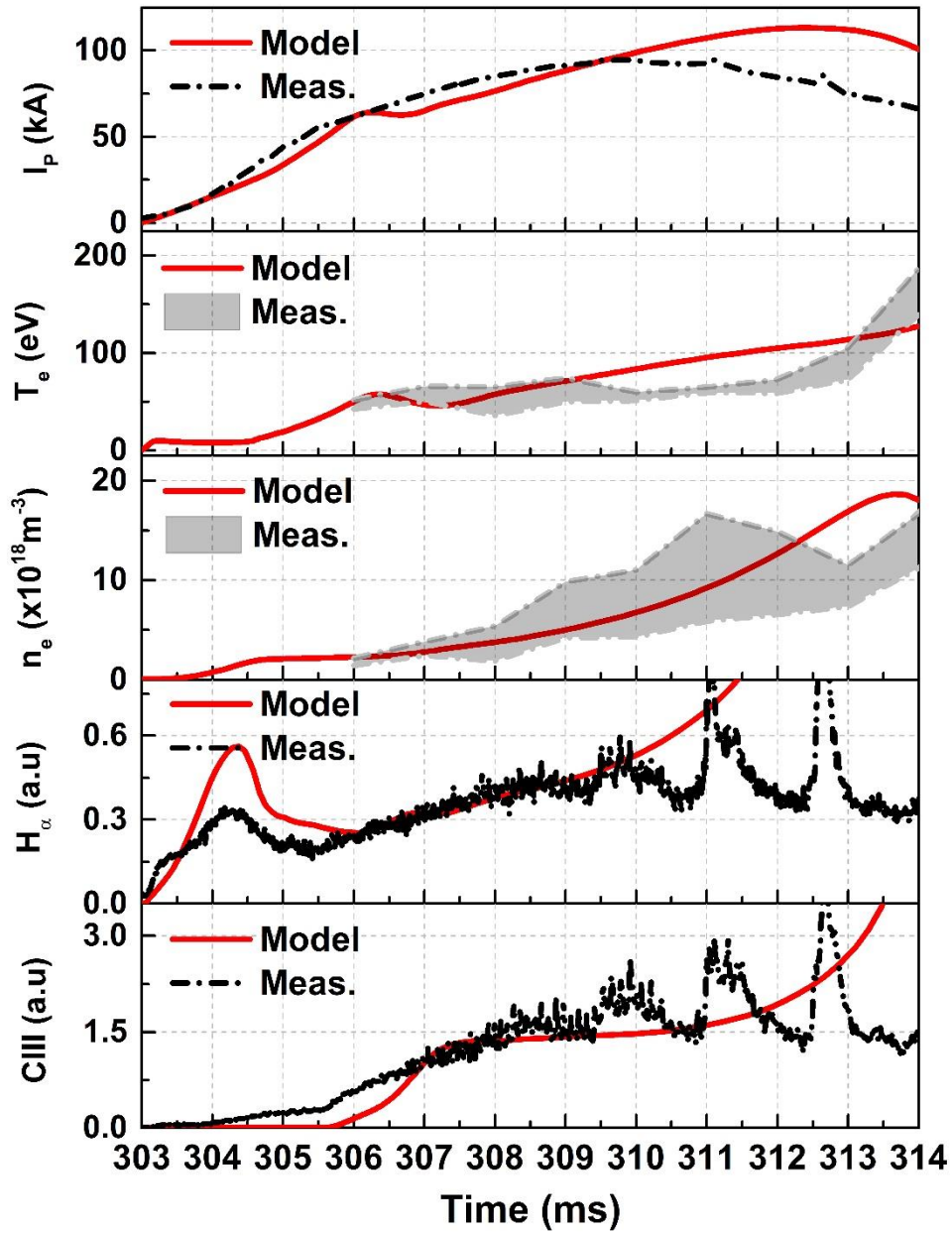


Figure 4.15 Time evolution in (from up to down): plasma current, electron temperature, electron density, H_{α} line emission signal and CIII line emission signal from the model (red) and experiment (black and grey) in the shot#37442.

4.2.3. Ohmic discharges with different wall conditioning methods

Two different wall conditioning methods have been conducted for ohmic discharges in VEST. One is a typical helium glow discharge cleaning (GDC) [48] and the other is a utilization of carborane power during the He-GDC, boronization [49]. First method is effective to reduce the hydrogen retention. However, it doesn't help significantly to reduce impurity retention such as oxygen and carbon. On the other hand, boronization conditioning has an opposite effect to the typical He-GDC conditioning. In other words, excessive hydrogen recycling and reduced oxygen impurity influxes are observed during the ohmic discharge after the boronization conditioning.

Two ohmic discharges with different wall conditioning method are conducted as mentioned above. Operational conditions except for the wall conditioning method are similar in both ohmic discharges as shown in Fig.4.13. Fig.4.14 shows the features of two ohmic discharges. Before ~309 ms, evolution in plasma current, impurity line emission signals are quite similar in both ohmic discharges. In the He-GDC discharge (shot#37866), ramp rate of plasma current decreases and plasma current ramps down after the peak current, which is mainly due to the impurity influx as observed in the OII and CIII line emission signals. The increase of impurity influx is caused by the plasma wall interactions with the centerstack. In the boronization discharge (shot#37906), high plasma current and longer pulse are obtained with reduction of impurity influx. The reduction of impurity influx is clearly observed in the OII and CIII line emission signals. Higher H_{α} line emission signal occurs than in the He-GDC discharge and it indicates the higher hydrogen recycling due to the boronization conditioning. There is no significant difference in electron temperature between two discharges. Even though the impurity influx is significantly reduced, it is thought that excessive hydrogen recycling due to the boronization prevents the electron temperature to rise. Maximum electron density is higher in the boronization discharge and it is consistent with the H_{α} line emission signal.

Fig.4.18 and Fig.4.19 show the model results in the shot#37906 and 37866, respectively. Higher carbon sputtering yield in the shot#37866 is set in order to consider the wall conditions. Overall time evolution in plasma parameters are well reproduced in both model results. Especially, decrease of the plasma current after peak due to the significant impurity influx is clearly reproduced in the case of shot#37866. There is a discrepancy in H_α peak location between the model and experiment. There can be uncertainty in prefill pressure measured by pressure gauge. However, it doesn't affect the overall evolution in both cases.

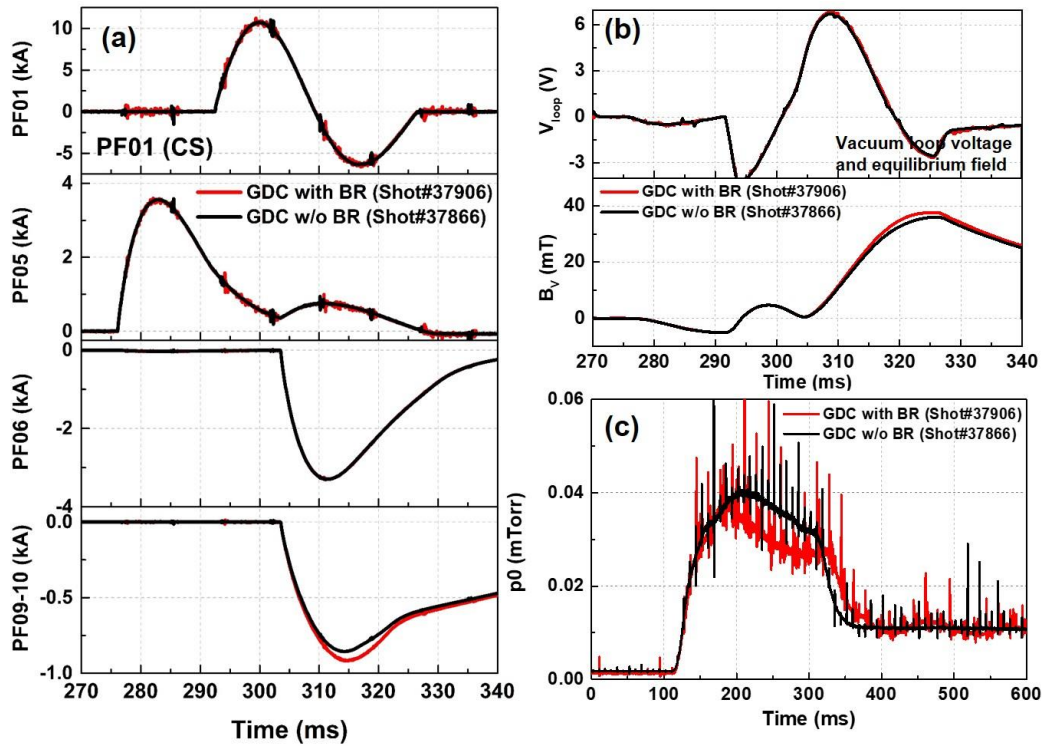


Figure 4.16 Operational conditions in the shot#37906 and 37866: (a) PF coil current waveforms, (b) loop voltage and equilibrium field at machine center, and (c) neutral pressure evolutions.

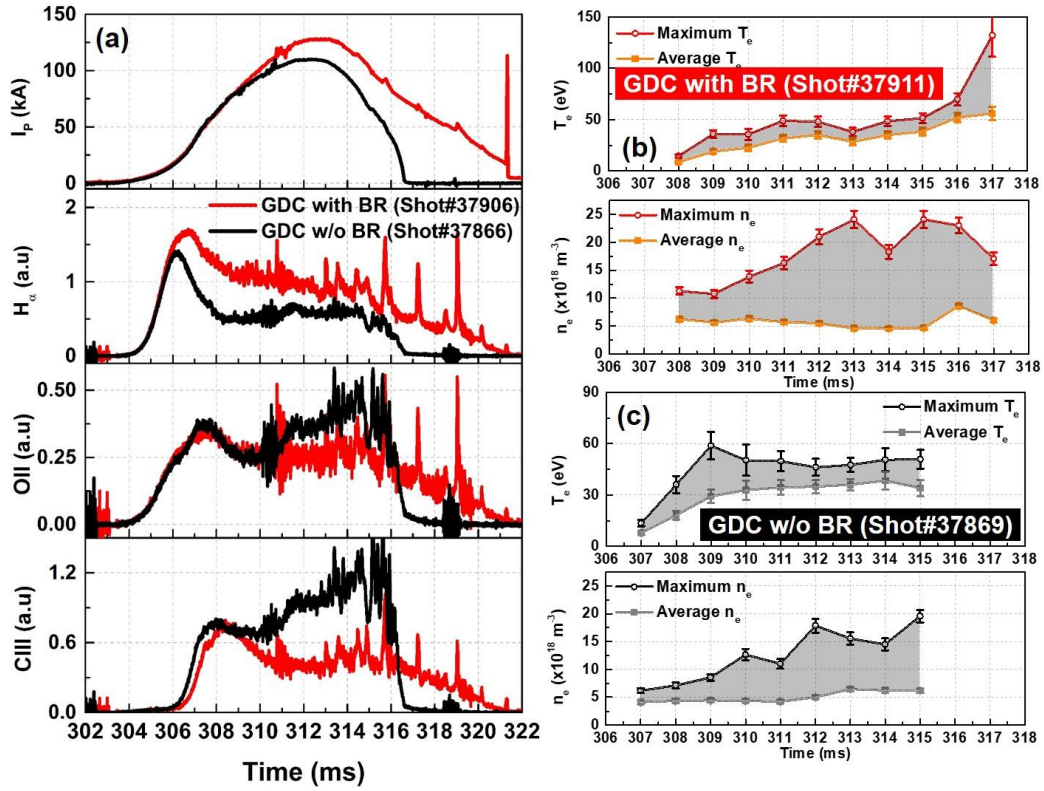


Figure 4.17 Features of ohmic discharges in the shot#37906 and 37866: (a) plasma current and filterscope signals (H_α , OII and CIII), electron temperature and density evolutions (b) in the shot#37911 and (c) in the shot#37869.

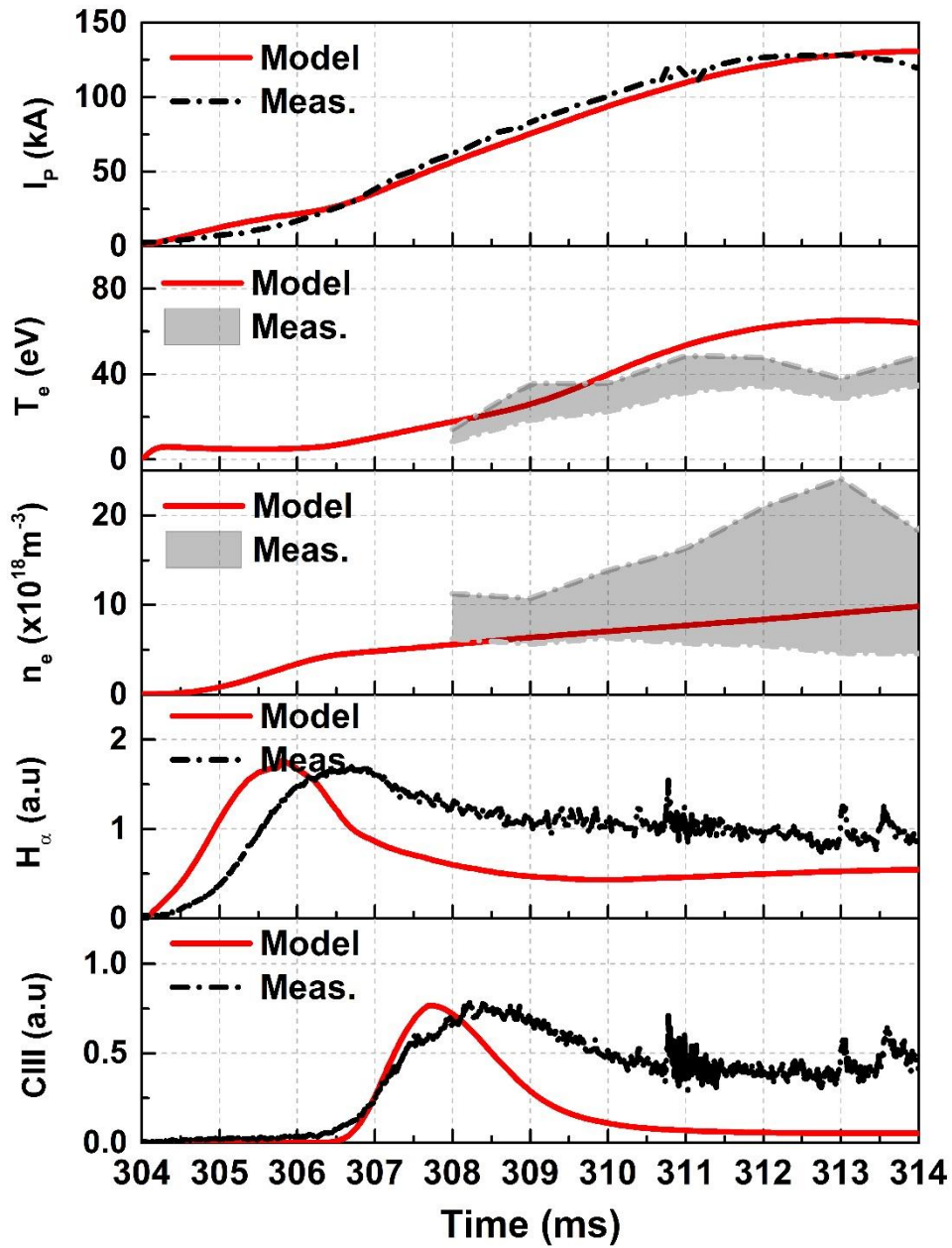


Figure 4.18 Time evolution in (from up to down): plasma current, electron temperature, electron density, H_{α} line emission signal and CIII line emission signal from the model (red) and experiment (black and grey) in the shot#37906 (boronization).

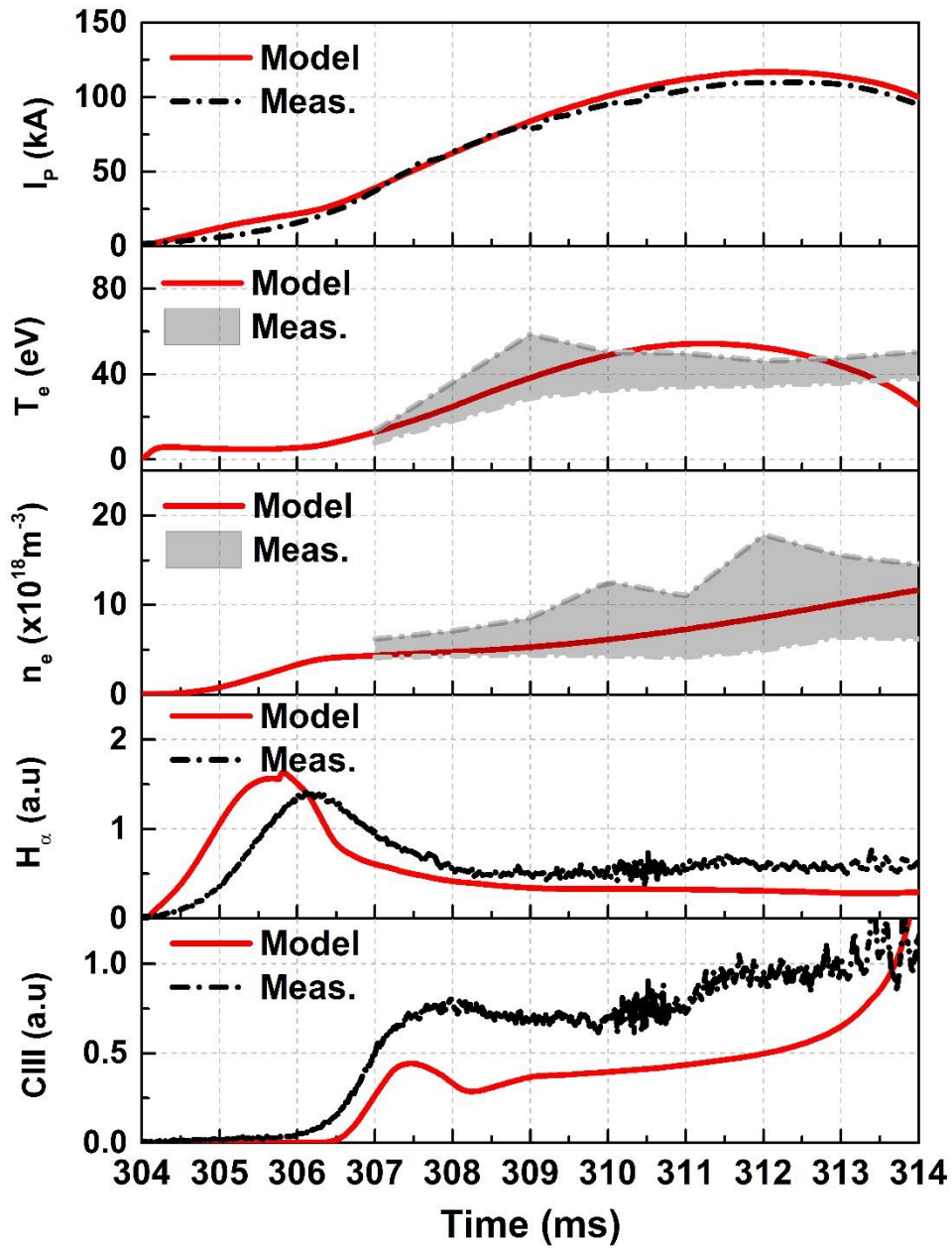


Figure 4.19 Time evolution in (from up to down): plasma current, electron temperature, electron density, H_{α} line emission signal and CIII line emission signal from the model (red) and experiment (black and grey) in the shot#37866 (only GDC).

4.3. Prediction of ohmic discharges for VEST-Upgrade

So far, it is confirmed that the start-up model can be utilized for prediction of ohmic discharges after the validation in several ohmic discharges in VEST. In this chapter, prediction of ohmic discharge is described for achievement of target plasma current in VEST. Firstly, the central solenoid current waveform is adjusted with two cases: slow ramp-down and fast ramp-down. Then, parameters related to the plasma wall interaction are adjusted based on the first results.

Fig. 4.20 shows a prediction of ohmic discharges with two central solenoid current waveforms by using the full electromagnetic start-up model. Input parameters for the calculation as follows in both cases: Prefill neutral pressure (3 mPa), toroidal field (0.18 T), hydrogen recycling coefficient (1.025), and carbon sputtering yield (0.05). Central solenoid current waveforms are set as shown in Fig.4.20 with consideration of limitation CS power system. In the fast ramp-down case, fast burn-through is observed due to the high loop voltage at initial phase. The plasma current evolves with higher ramp-up rate of 13 MA/s on average than the target rate (10 MA/s). With the higher current ramp-up rate, 0.4 MA of plasma current is achieved in the model. However, the maximum plasma current is not maintained due to the lower loop voltage after 300 ms. According to the electron density evolution, prefill neutral pressure of 3 mPa is thought to be sufficient due to the hydrogen wall recycling. In the second case with slow ramp-down, a peak of H_{α} line emission occurs late. Plasma current rises with similar target ramp-up rate on average. After the peak plasma current about 0.3 MA, flat-top phase is achieved during 20 ms. Overall evolution in the plasma current is similar as the target plasma current. Also, prefill neutral pressure of 3 mPa is sufficient as like the fast ramp-down case. Consequently, according to the model result, it is suggested that slow ramp-down of the CS from 20 kA to -20 kA during 50 ms can achieve the target plasma current.

Next, the wall recycling and sputtering parameters are adjusted with the slow ramp-

down of the CS waveform. The results are shown in Fig.4.21. Loop voltage is identical in all cases due to the same CS waveform. In the cases of hydrogen recycling control, plasma current evolutions are similar in three cases. However, plasma current is significantly reduced with higher recycling parameter (~ 1.1) after the peak current. This value is consistent with the boronization case in present ohmic discharge of VEST. With excessive retention of hydrogen neutrals, the electron density increases up to $3 \times 10^{19} m^{-3}$ and the electron temperature decreases constantly. In the control of carbon sputtering yield, the overall plasma parameters such as plasma current and electron temperature are slightly reduced with higher carbon sputtering yield. In VEST, carbon impurity can be reduced by the glow discharge with boronization. Therefore, it is required to control the electron density due to the excessive hydrogen recycling in boronized wall in order to achieve the target plasma current.

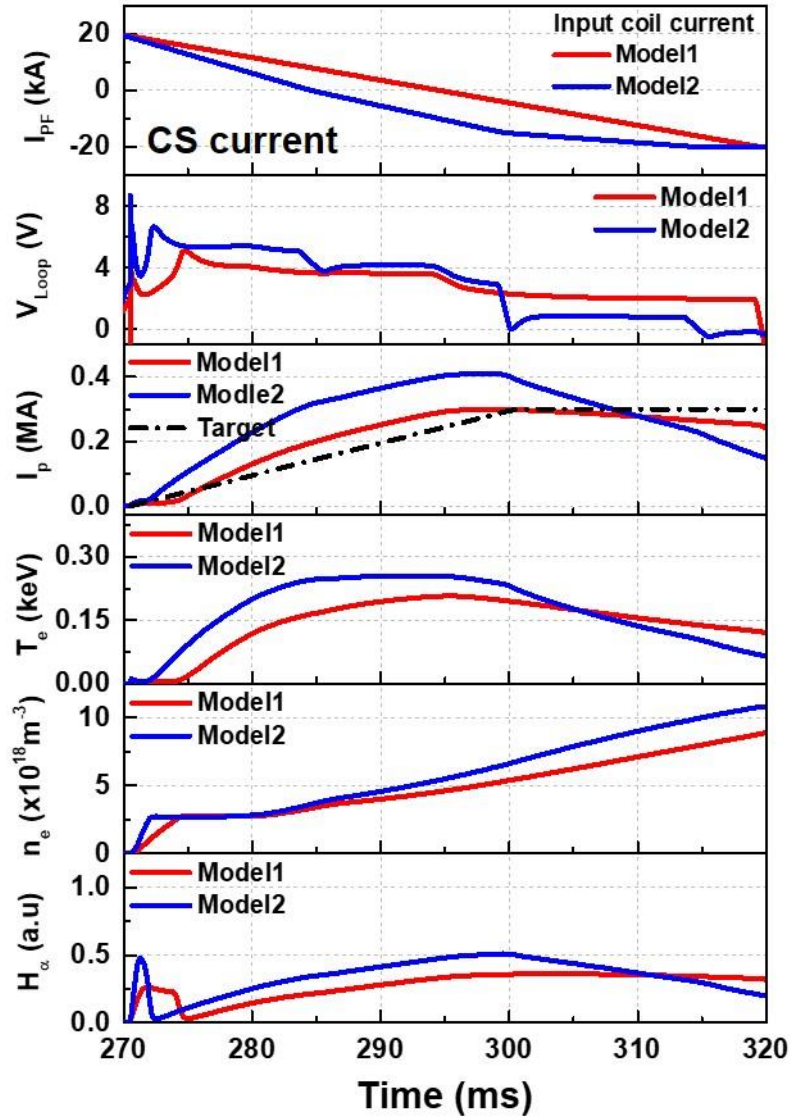


Figure 4.20 Prediction of evolution parameters in two cases (red-slow ramp down and blue-fast ramp down): central solenoid current, loop voltage at plasma center, plasma current, electron temperature, electron density and H_α line emission signal from up to down.

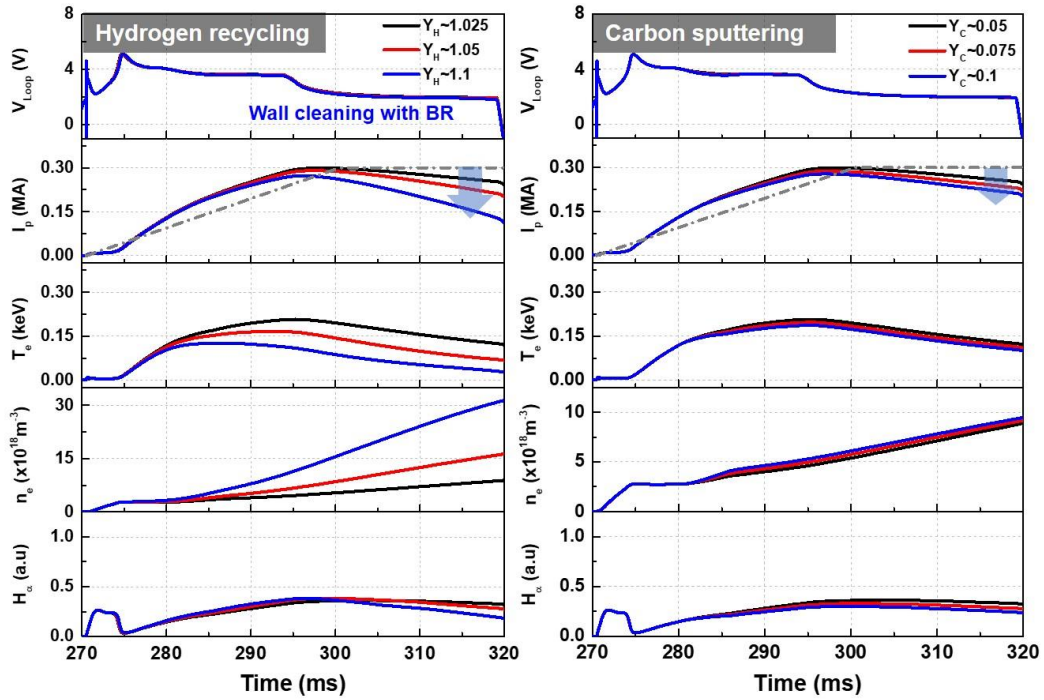


Figure 4.21 Prediction of evolution parameters in two cases (left-hydrogen recycling coefficient and right-carbon sputtering yield): central solenoid current, loop voltage at plasma center, plasma current, electron temperature, electron density and Ha line emission signal from up to down.

4.4. Validation in MAST and prediction in STEP [17, 51]

The start-up model is applied to not only the compact ST, VEST but also the mid- and huge size ST devices, MAST and STEP. Unlike VEST ohmic discharges, when the plasma current grows to some extent, the transport effect is dominant than the start-up features such as electromagnetic or atomic effects in the mid- and huge size devices. Therefore, the start-up model is applied from the plasma breakdown to partial current rise phase for MAST and STEP. For application to the MAST and STEP, the sub-models which are described in section 3 are selectively utilized. First of all, the full electromagnetic model can be utilized regardless of machine specifications. It is difficult to apply the VEST external self-inductance to MAST and STEP because the plasma shape information between VEST and MAST & STEP is different. Therefore, the original Hirshman model for plasma external self-inductance is utilized for simulations in MAST and STEP. Transports are assumed to be fully convective and the carbon sputtering yield for the plasma wall interaction model is set to be constant in time.

There are two main operational scenarios for plasma initiation in MAST, namely double merging compression [50] and conventional direct ohmic start-up. Fig.4.22 depicts the central solenoid and PF coils in MAST. Typical ohmic scenario with the central solenoid is simulated using the full electromagnetic start-up model. Fig.4.X (a) shows the central solenoid and PF coil currents for model inputs. Solving the full circuit equations, the vacuum vessel eddy currents and the plasma current evolutions are obtained as shown in Fig.4.23 (b) and (f). Evolution in the plasma current is reasonably reproduced. The plasma volume from the Townsend model is compared to the one from the EFIT reconstruction. The result between the start-up model and EFIT reconstruction shows good agreement. In addition to the 0D parameters, evolution of 2D poloidal magnetic flux map simulated in the start-up model during the plasma breakdown and burn-through phases is depicted in Fig.4.24. As can be seen in Fig4.23, due to the open magnetic field

lines, the plasma volume is extended to the vessel wall at the beginning. The plasma volume reduced to a smaller volume as the plasma current increases and the closed flux surface are formed. As mentioned above, the calculated plasma volume agrees well with the EFIT volume data (the first plasma volume data in EFIT is available from 30 (ms)).

STEP (Spherical Tokamak for Energy Production) is a UKAEA program that will demonstrate the ability to generate net electricity from fusion and it is on machine design phase [51]. The start-up model can be utilized to design of the central solenoid, PF coils and vacuum vessel structure for reliable burn-through. Fig.4.25 is an example of predictive simulation in STEP [51]. From this result, the successful plasma breakdown occurs near 400 ms after the central solenoid swing. Also, the plasma burn-through is achieved and the plasma current ramps up to ~ 2 MA in the simulation result.

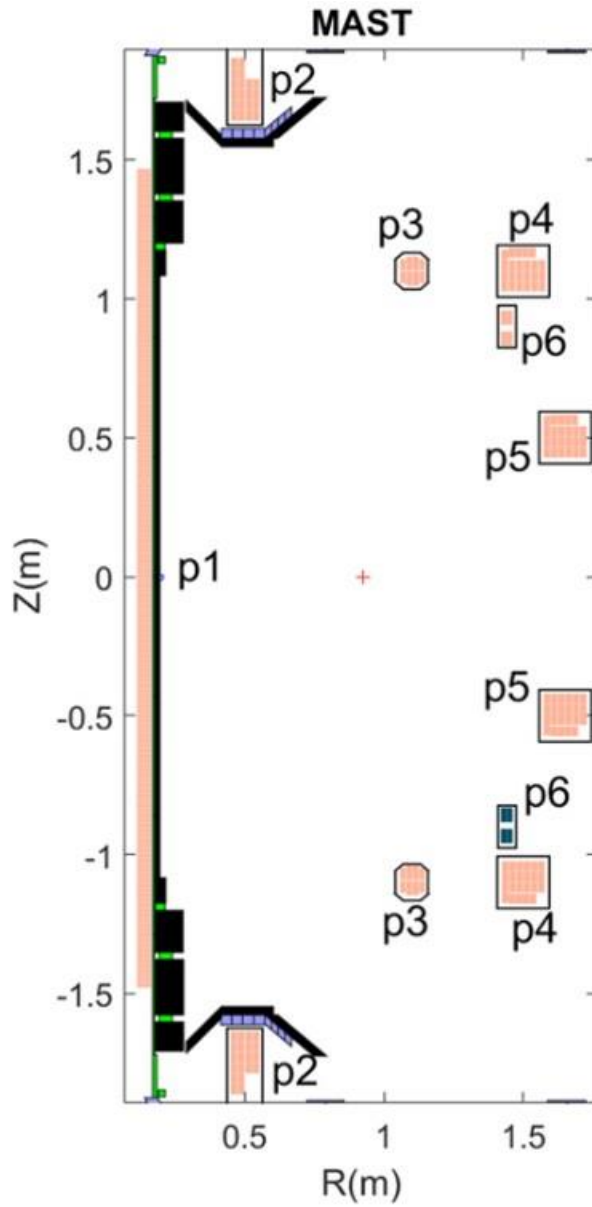


Figure 4.22 Schematic of central solenoid and PF coils (grey color) in MAST. The toroidally conducting vacuum vessel structure are in black color. Taken from figure 2 of [17].

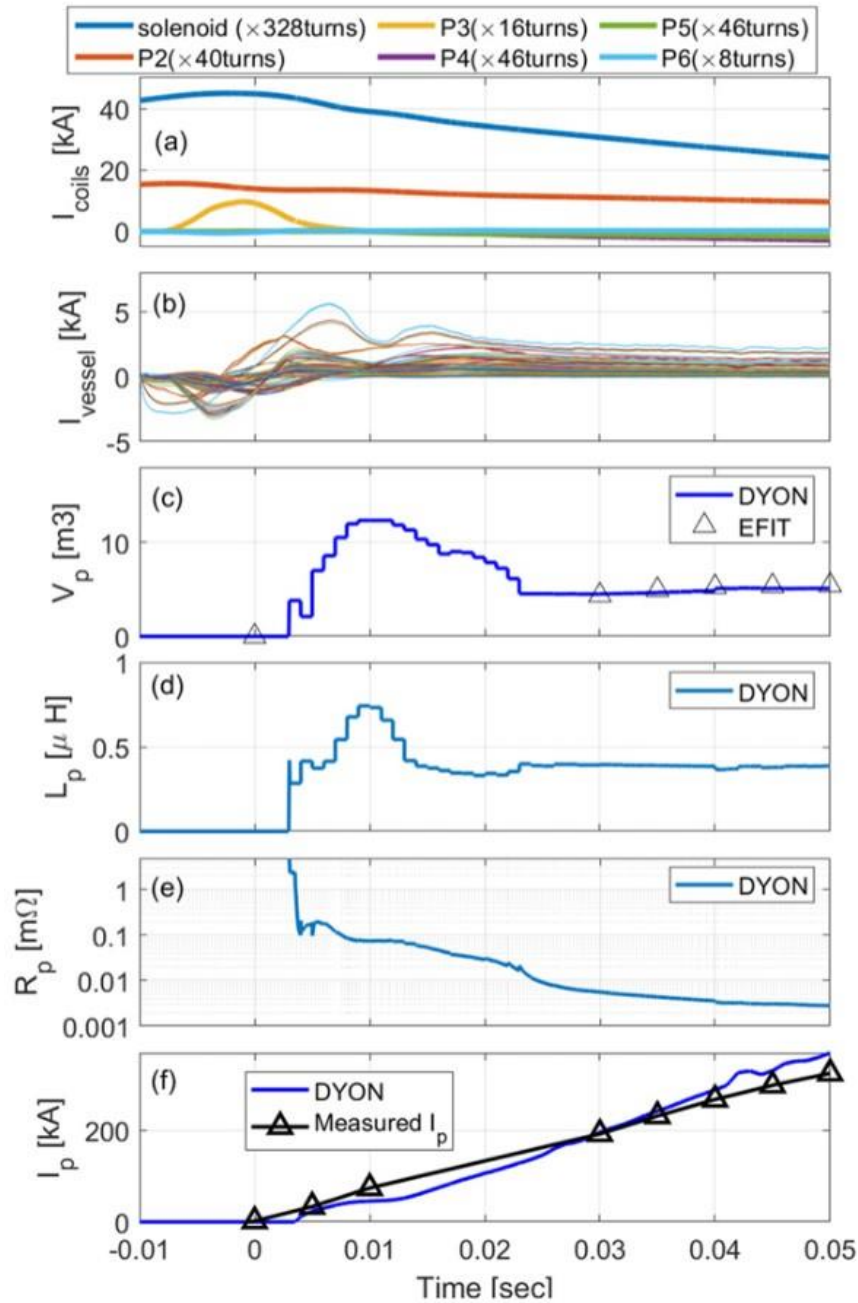


Figure 4.23 (a) Input coil current waveforms utilized in the start-up model, (b) vacuum vessel eddy current, (c) plasma volume, (d) plasma self-inductance, (e) plasma resistance, and (f) plasma current evolution in MAST simulation. Taken from figure 3 of [17].

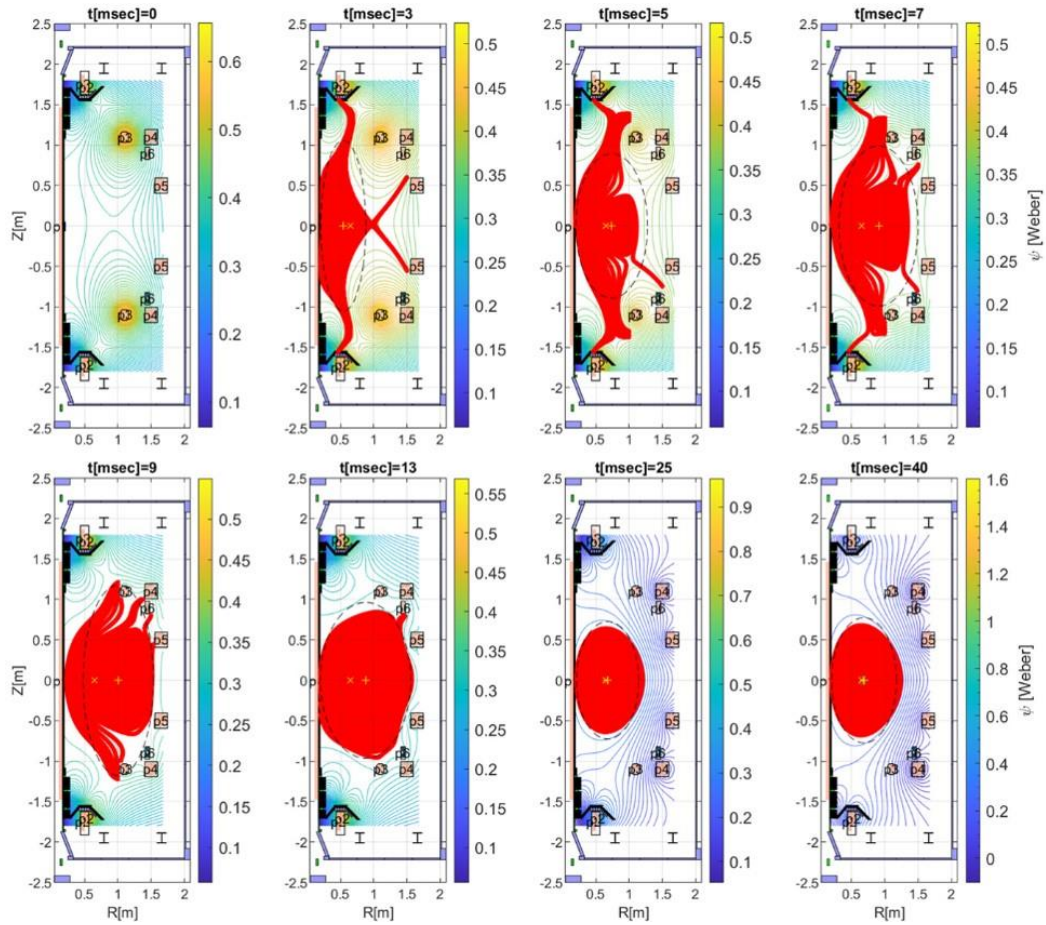


Figure 4.24 Evolution of plasma volume and poloidal magnetic flux map simulated in the start-up model during the plasma breakdown and burn-through phases. Taken from figure 4 of [17].

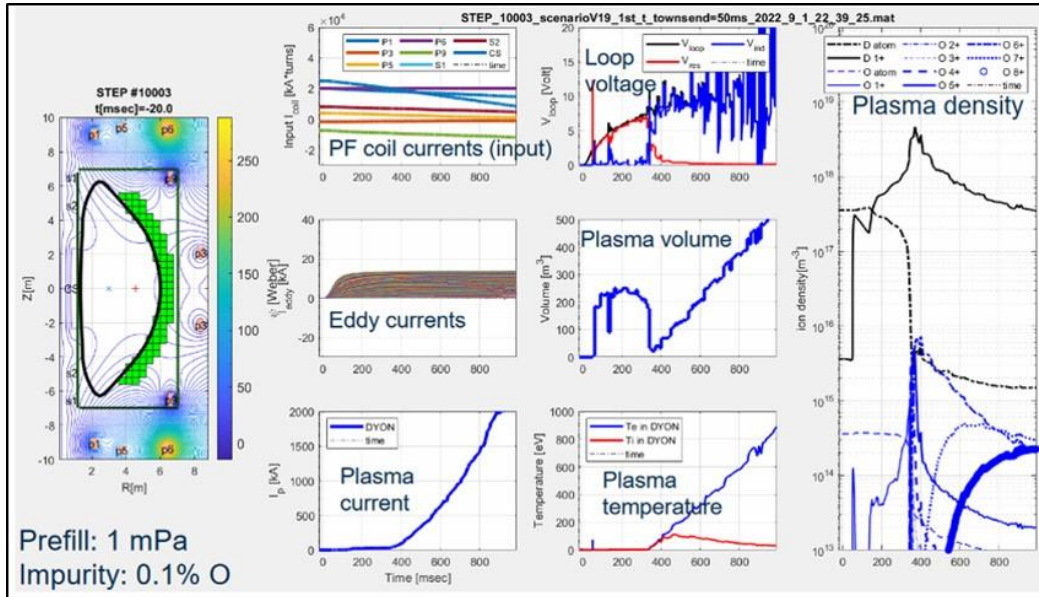


Figure 4.25 Simulation results in STEP: vacuum poloidal magnetic flux map, PF coil currents, vacuum vessel eddy current, plasma current, loop voltage, plasma volume, plasma temperature and plasma density evolutions. Taken from page 21 of [51].

Chapter 5. Conclusions

5.1. Summary and conclusions

In summary, the new start-up model is developed in order to predict ohmic discharges for VEST-Upgrade. In the new start-up model, dynamic electromagnetic effect induced by PF coils and vacuum vessel eddy currents and significant neutral effect due to the plasma wall interactions mainly are considered. In order to confirm validity of the new start-up model in VEST, several ohmic discharges with different operational condition in VEST are reproduced by using the model. After the validation, ohmic discharges with new central solenoid waveforms and different wall condition parameters are predicted in order to achieve the target plasma current. The new start-up model is also validated in a medium size spherical torus, MAST [17]. Finally, predictive simulation for burn-through phase is conducted to utilize for a huge spherical torus (STEP) design [50].

In conclusion, this dissertation presents the development, validation of the model and prediction of new ohmic discharges in several ST devices: VEST, MAST and STEP. The full electromagnetic model can calculate the exact loop voltage with given machine specification. Also, it can be confirmed that a new inductance model without assumption of large aspect ratio is required for a reliable plasma current evolution in spherical tori. The new start-up model can reproduce several ohmic discharges in VEST with reasonable level. According to the prediction of ohmic discharges in VEST, it is suggested that the target plasma current can be achieved with slow ramp-down of the CS current waveform from 20 kA to -20 kA during 50 ms. However, the wall condition with low hydrogen retention wall is required for the target plasma current. In other words, it is difficult to achieve the target plasma current with present wall conditions after the boronization due to the significant hydrogen retention. Therefore, improvements in wall conditioning methods should be required. In order to suggest that the new model can be utilized not

only in VEST but also other devices, the start-up model is validated in MAST ohmic discharges [17]. After the validation in the mid-size ST, the start-up model calculates the burn-through phase in the huge size ST, STEP. From the result in STEP simulation, it is thought that 9 Vs of volt-second provided by central solenoid is sufficient for initiation and target plasma production [50].

5.2. Future works

5.2.1. Preliminary result of small ST formation using the start-up model

There are several alternative start-up methods such as outer PF coil start-up [52], local helicity injection (LHI) start-up [53, 54] and double plasma merging (DPM) start-up [50, 55], which are suggested in spherical torus due to narrow space in centerstack. Above start-up methods have been actively investigated in VEST. Among these methods, the full electromagnetic start-up model in this research can be applied to the outer PF coil start-up and the DPM start-up. The model is utilized for the DPM start-up method.

Fig.5.1 shows a partial solenoid coil current and loop voltage waveforms calculated by the electromagnetic model in the shot#38243. In this shot, other PF coils are not utilized and other operational conditions are as follows: $B_t = 0.1 \text{ T}$ at $(0.25, 0.98) \text{ m}$ and $p_0 = 3.3 \text{ mPa}$. Even though loop voltage is applied with prefilled neutral pressure, no plasma breakdown occurs. The simulation by using the model is conducted with consistent operational conditions with this fail case for model inputs.

Fig.5.2 shows a simulation result with the partial solenoid operation case. In the model result, plasma current with $\sim 1 \text{ kA}$ can be generated with given operational conditions. The burn-through isn't achieved because the loop voltage induced by the partial solenoid coil is thought to be too low. Important thing is that there is an inconsistency between the model and experiment. In the experiment, the plasma breakdown fails. But the plasma breakdown can be achieved according to the model result. Therefore, it is necessary to improve the plasma breakdown model with consideration of other factors, such as self-generated electric field [8, 9].

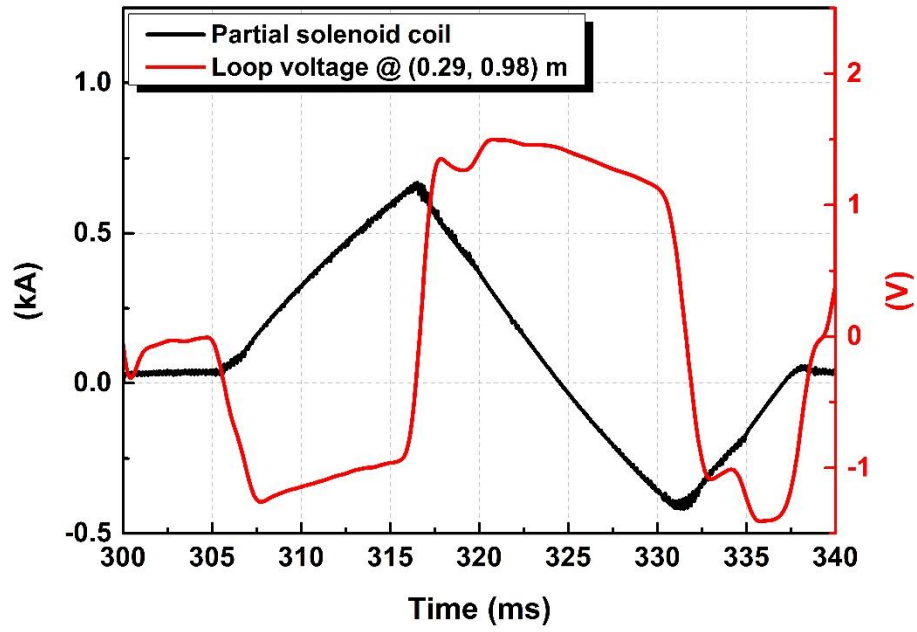


Figure 5.1 Partial solenoid coil current and loop voltage evolution in the shot#38243.

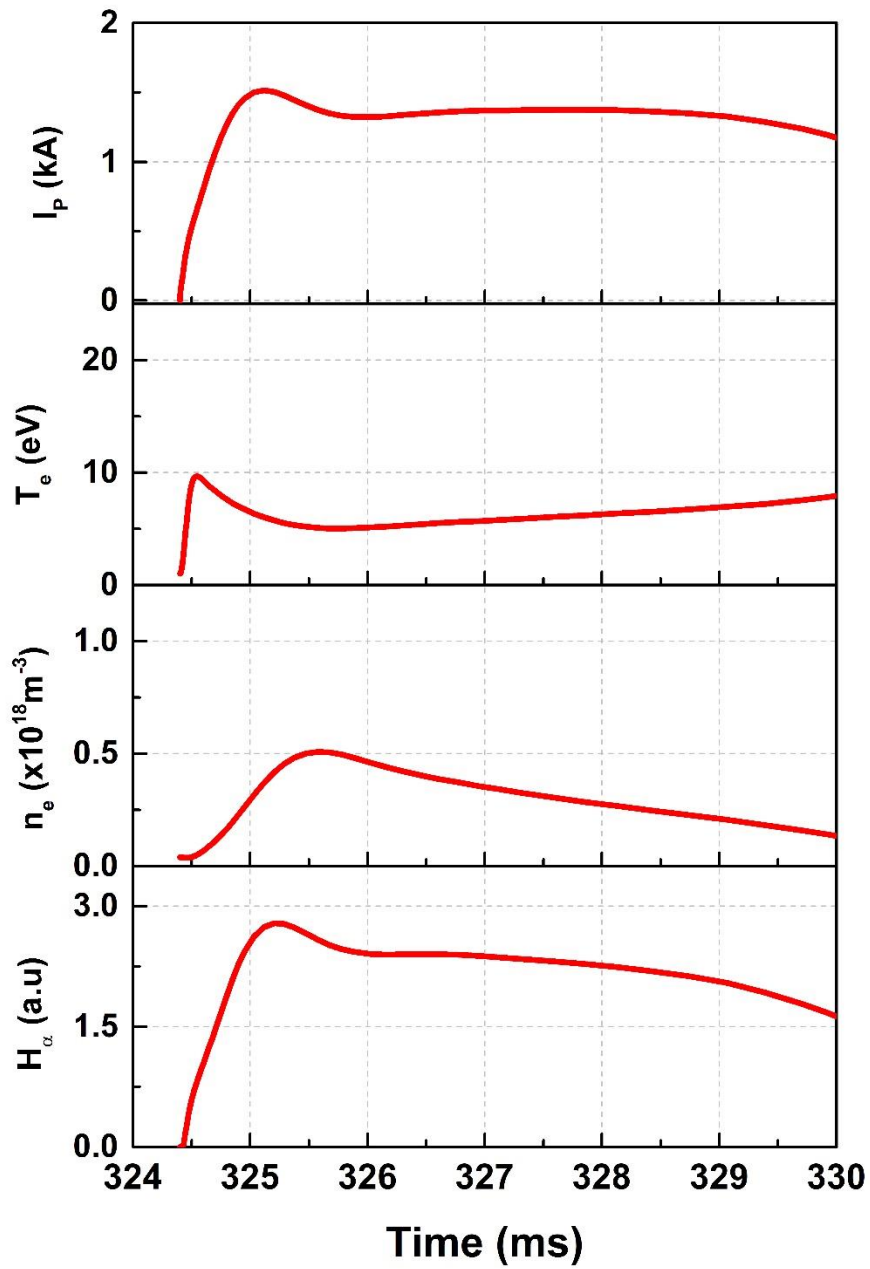


Figure 5.2 Time evolution in the plasma current, electron temperature, electron density and H_α line emission signal from the model (shot#37243: experimentally fail case).

5.2.2. Future works

In this research, several ad-hoc models are utilized such as reference plasma current which determines a transition phase from the open field to closed field configuration. Even though it is confirmed that the ad-hoc model is valid to VEST ohmic discharges suggested here for the model validation, a physics model is required for its application to various circumstance. Dedicated efforts will be conducted to develop a model in a dynamic transition phase.

After the validation in VEST ohmic discharges, prediction of ohmic discharges with several operational conditions are conducted. The model results will be confirmed by experimental results with improved coil power supply system in VEST.

In the previous section (5.2.1), the model is applied to the DPM start-up using partial solenoid coils to check the generation of small ST plasma in sub-chamber of VEST. The model shows a consistent result with the experiment, i.e. no plasma initiation. The model will be utilized for suggestion of operational scenario in order to generate a small ST plasma in sub-chamber of VEST.

Bibliography

- [1] Wesson, J. and D.J. Campbell, *Tokamaks*. Vol. 149. 2011: Oxford university press.
- [2] Ono, M. and R. Kaita, *Recent progress on spherical torus research*. Physics of Plasmas, 2015. **22** (4).
- [3] Popoular, R. *The genesis of toroidal discharges*. Nuclear Fusion, 1976. **16** (37).
- [4] Lloyd, B., et al., *Low-voltage ohmic and electron-cyclotron heating assisted start-up in DIII-D*. Nuclear Fusion, 1991. **31** (2031-2053).
- [5] Lloyd, B., Carolan, P. G. and Warrick, C. D. *ECRH-assisted start-up in ITER*. Plasma Physics and Controlled Fusion, 1996. **38** (1627-1643).
- [6] Mueller, D., *The physics of tokamak start-up*. Physics of Plasmas, 2013. **20** (58101).
- [7] ITER Physics Expert Group on Disruptions, Plasma Control, and MHD et al., *Chapter 8: Plasma operation and control*. Nuclear Fusion, 1999. **39** (2577).
- [8] Min-Gu Yoo, et al., *Evidence of a turbulent ExB mixing avalanche mechanism of gas breakdown in strongly magnetized systems*. Nature Communications, 2018. **9** (3523).
- [9] Min-Gu Yoo and Yong-Su Na, *Understanding the electromagnetic topology during the ohmic breakdown in tokamaks considering self-generated electric fields*. Plasma Physics and Controlled Fusion, 2022. **64** (054008).
- [10] Chung, K., et al., *Design features and commissioning of the versatile experiment spherical torus (VEST) at Seoul National University*. Plasma Science and Technology, 2013. **15** (3).
- [11] Won-ik Jung., et al., *Improvement of vacuum and wall conditioning systems in Versatile Experiment Spherical Torus*. 21st International Spherical Torus Workshop (ISTW 2022), 5 November 2022, online..
- [12] Hyun-Tae Kim, W. Fundamenski, A.C.C. Sips and JET-EFDA Contributors, *Enhancement of plasma burn-through simulation and validation in JET*. Nuclear Fusion, 2012. **52** (103016).
- [13] Hyun-Tae Kim, A.C.C. Sips, P.C.de Vries and JET- EFDA Contributors, *Plasma burn-through simulations using the DYON code and predictions for ITER*. Plasma Physics and Controlled Fusion, 2013. **55** (124032).
- [14] Hyun-Tae Kim, A.C.C. Sips, W. Fundamenski and EFDA-JET Contributors, *PSI effects on plasma burn-through in JET*. Journal of Nuclear Materials, 2013. **438** (S1271-S1274).
- [15] G. Granucci., et al., *Experiments and modeling on FTU tokamak for EC assisted plasma start-up studies in ITER-like configuration*. Nuclear Fusion, 2015. **55** (093025).
- [16] D. J. Battaglia., et al., *Reduced model for direct induction startup scenario development on MAST-U and NSTX-U*. Nuclear Fusion, 2019. **59** (126016).
- [17] Hyun-Tae Kim., et al., *Development of full electromagnetic plasma burn-through model and validation in MAST*. Nuclear Fusion, 2022. **62** (126012).
- [18] JongGab Jo., et al., *Efficient pre-ionization by direct X-B model conversion in VEST*. Physics of Plasmas, 2017. **24** (012103).

- [19] T. S. Kim., *Conceptual design of NBI beamline for VEST plasma heating*. Fusion Engineering and Design, 2016. **109-111**, PartA (411-415).
- [20] Tae-Seong Kim, Bongki Jung and Seung Ho Jeong, *Beam extraction characteristics of a low-energy, high-current pulsed ion source of a versatile experiment spherical torus neutral beam injector*. Fusion Engineering and Design, 2018. **136**, PartB (1365-1369).
- [21] Bong-Ki Jung., et al., *Development of pulse power supply system based on Marx generator for the arc ion source of the VEST NBI*. Fusion Engineering and Design, 2017. **123** (358-361).
- [22] Sun-Ho Kim., et al., *Heating and current drive by fast wave in lower hybrid range of frequency on Versatile Experiment Spherical Torus*. Fusion Engineering and Design, 2016. **109-111**, PartA (707-711).
- [23] JongGab Jo., et al., *Modified propagation path and expanded coupling regime of lower hybrid fast wave by n_{\parallel} -upshift via wave scattering in VEST*. Physics of Plasmas, 2019. **26**, (012506).
- [24] YoungHwa An., et al., *Plasma start-up design and first plasma experiment in VEST*. Fusion Engineering and Design, 2015. **96-97**, (274-280).
- [25] YoungHwa An., et al., *Efficient ECH-assisted plasma start-up using trapped particle configuration in the versatile experiment spherical torus*. Nuclear Fusion, 2016. **57** (016001).
- [26] L.L. Lao., et al., *MHD equilibrium reconstruction in the DIII-D tokamak*. Fusion Science and Technology, 2005. **48** (968-977).
- [27] Jeongwon Lee., et al., *Design and commissioning of magnetic diagnostics in VEST*. Fusion Engineering and Design, 2013. **88**, (1327-1331).
- [28] Yang Jeong-hun., et al., *Design of a dual sensor probe array for internal field measurement in Versatile Experiment Spherical Torus*. Review of Scientific Instruments, 2012. **83** (10D721).
- [29] J. Yang, J. W. Lee, B. K. Jung, K. J. Chung, and Y. S. Hwang, *Development of internal magnetic probe for current density profile measurement in Versatile Experiment Spherical Torus*. Review of Scientific Instruments, 2014. **85** (11D809).
- [30] Jeongwon Lee., et al., *Development of equilibrium fitting code using finite element method in versatile experiment spherical torus*. Fusion Engineering and Design, 2018. **131**, (141-149).
- [31] Young-Gi Kim., et al., *Development of Thomson scattering system on VEST*. Fusion Engineering and Design, 2019. **143**, (130).
- [32] D. Kim, Y. -G. Kim, J. H. Lee, Y. S. Na, and Y. S. Hwang, *Upgrade of Thomson scattering system on VEST*. Fusion Engineering and Design, 2019. **146**, (1131).
- [33] J. H. Kim, Y. -G. Kim, D. Kim, J. H. Lee, and Y. S. Hwang, *Radial profile measurement with an improved 1 kHz Thomson scattering system on Versatile Experiment Spherical Torus*. Review of Scientific Instruments, 2021. **92** (043539).
- [34] YooSung Kim., et al., *Design of combined system of helium charge exchange spectroscopy and hydrogen beam emission spectroscopy in VEST*. Fusion Engineering and Design, 2017. **123**, (975-978).

- [35] Seongcheol Kim., et al., *Plasma burn-through simulation for a small spherical torus VEST with DYON simulator*. 1st International Fusion and Plasma Conference, 22-26 August 2022, Jeju, Republic of Korea.
- [36] Rajiv Goswami, Jean-Francois Artaud, and ADITYA team, *An enhanced tokamak startup model*. Physics of Plasmas, 2017. **24** (012508).
- [37] S. P. Hirshman. and G. H. Neilson, *External inductance of an axisymmetric plasma*. Physics of Fluids, 1986. **29** (790).
- [38] Osamu Mitarai and Yuichi Takase, *Plasma current rampup by the outer vertical field coils in a spherical tokamak reactor*. Plasma Science and Technology, 2003. **43**.
- [39] J. L. Barr., et al., *A power-balance model for local helicity injection startup in a spherical tokamak*. Nuclear Fusion, 2018. **58** (076011).
- [40] O. Sauter, C. Angioni, and Y. R. Lin-Liu, *Neoclassical conductivity and bootstrap current formulas for general axisymmetric equilibria and arbitrary collisionality regime*. Physics of Plasmas, 1999. **6** (2834).
- [41] C. T. Hsu, K. C. Shaing, R. P. Gormley, and D. J. Sigmar, *Bootstrap current induced by fusion born alpha particles*. Physicas of Fluids B, 1992. **4** (4023).
- [42] W. A. Houlberg, K. C. Shaing, S. P. Hirshman, and M. C. Zarnstorff, *Bootstrap current and neoclassical transport in tokamaks of arbitrary collisionality and aspect ratio*. Physics of Plasmas, 1997. **4** (3230).
- [43] Seongcheol Kim, Jae Young Jang, YooSung Kim, and Y. S. Hwang, *Acceleration of ion rotation during internal reconnection events in the versatile experiment spherical torus (VEST)*. Nuclear Fusion, 2021. **61** (126011).
- [44] E.C. Jung., et al., *Observation of MHD-correlated blobs during internal reconnection events in VEST*. Nuclear Fusion, 2022. **62** (126029).
- [45] P. Helander., et al., *Ion acceleration during reconnection in MAST*. Physics Review Letters, 2002. **89** (23).
- [46] A. Ejiri., et al., *Ion temperature increase during MHD events on the TST-2 spherical tokamak*. Nuclear Fusion, 2003. **43** (547-552).
- [47] I. Semenov., et al., *Phenomenology of internal reconnections in the National Spherical Torus Experiment*. Physics of Plasmas, 2003. **10** (664).
- [48] H. Y. Lee., et al., *Development of wall conditioning and impurity monitoring systems in Versatile Experiment Spherical Torus (VEST)*. Fusion Engineering and Design, 2016. **109-111**, PartB (1082-1086).
- [49] J. Yang., et al., *Effect of boronization in VEST: Achieving 0.1 MA discharge*. Fusion Engineering and Design, 2018. **137** (358-361).
- [50] M.P. Gryazevich and A. Sykes, *Merging-compression formation of high temperature tokamak plasma*. Nuclear Fusion, 2017. **57** (072003).
- [51] Ken McClements., et al., *Plasma scenario development in the Spherical Tokamak for Energy Production (STEP)*. 21st International Spherical Torus Workshop (ISTW 2022), 1 November 2022, online.
- [52] 이현영, *Study on Solenoid-free Startup utilizing outer PF coils with help of pre-ionization via direct XB model conversion in VEST, VEST 장치에서 EBW 전이*

온화와 바깥쪽 PF 코일을 이용하여 솔레노이드 사용 없는 시동 연구. 2019, 서울 : 서울대학교 대학원: 서울.

- [53] JongYoon Park., et al., *Design and development of the helicity injection system in Versatile Experiment Spherical Torus*, 2015. **96-97** (269-273).
- [54] 박종윤, *Non-inductive current drive utilizing 3D magnetic flux ropes in Versatile Experiment Spherical Torus, VEST 장치에서의 3D 자기 플럭스 로프를 활용한 비유도적 전류 구동 연구*. 2022, 서울 : 서울대학교 대학원: 서울.
- [55] K.J. Cung., et al., *Initial plasma start-up using partial solenoid coils in Versatile Experiment Spherical Torus (VEST)*. *Fusion Engineering and Design*, 2013. **88** (787-790).

국 문 초 록

구형 토러스 장치에서의 저항 가열 방전 예측을 위한 전자기장 시동 모델 개발과 검증

김 성 철

에너지시스템공학부

(핵융합 및 플라즈마 공학 전공)

서울대학교 대학원

서울대학교에 설치되어 운전중인 구형 토러스 장치, VEST에서의 저항 가열 플라즈마 업그레이드를 위한 플라즈마 시동 예측을 위하여 토카막 초기 시동 모델이 개발되었다. VEST 장치의 저항 가열 플라즈마는 중심부 솔레노이드, 외부 폴로이달 자기장 코일 및 내벽에 흐르는 전류에 의한 전자기장 효과와 플라즈마-내벽 상호작용에 의한 불순물 유입 영향을 크게 받기 때문에 모델에 이러한 효과들을 고려할 필요가 있다. 모델 개발 과정에서 기존 연구사례에서 활용되던 여러 무차원 기반의 시동 코드 중 원자 프로세스가 잘 반영이 되어있는 DYON 코드를 활용하였다.

본 연구에서 저항 가열 예측을 목적으로 토카막 시동 모델을 개발하기 때문에 모델의 타당성을 확인하기 위하여 실험 데이터를 통한 검증이 필요하다. 모델 검증 과정은 VEST 장치에서 수행한 여러 운전 조건의 저항 가열 플라즈마에서 플라즈마 전류, 전자온도 와 밀도, 필터스코프 데이터를 상호비교를 통해 이루어졌다.

시동 모델의 주요 결과는 플라즈마 전류와 전자온도 및 밀도 성장이라 할 수 있다. 플라즈마 전류는 회로방정식을 통해 계산이 되며, 회로방정식에 주요 회로 변수들을 정확하게 모델링 할 필요가 있다. 기존 연구 사례에서는 플라즈마 전류를 발생시키는 일주전압을 정확하게 계산하는데 있어서 한계를 지니고 있었다. 정확한 일주

전압을 계산하기 위해서는 주어진 코일과 진공용기 구조를 고려한 전자기장 해석이 필요하다. 본 연구에서는 이를 위한 전자기장 해석 모델을 개발하였으며 VEST 장치의 플럭스 루프 실험데이터를 활용하여 개발된 모델을 검증하였다. 플라즈마 전류 성장을 결정하는 다른 중요한 요소는 플라즈마 인덕턴스와 플라즈마 저항이라 할 수 있다. 본 연구에서는 기존에 넓게 활용하는 중형비가 큰 토카막 플라즈마 가정의 인덕턴스 모델이 구형 토러스에서는 타당하지 않다는 것을 확인하였고, VEST 평형 데이터를 활용하여 Hirshman 모델을 기반으로 새로운 플라즈마 인덕턴스 모델을 개발하였다. 또한, 구형 토러스에서는 플라즈마 저항이 높은 가둠 입자 비율로 인하여 신고전 효과의 영향으로 일반적인 스피처 비저항 모델로 계산한 플라즈마 저항보다 클 수 있다. 이러한 효과를 고려하기 위하여 플라즈마가 폐자기면을 형성한 이후 영역에서 O. Sauter의 해석모델을 도입하여 플라즈마유�효저항을 계산하였으며, 정확한 정량적인 계산을 위하여 NCLASS 코드 결과를 활용하였다. 본 연구에서의 가둠 모델은 기존 연구에서 활용하던 하전입자의 대류에 의한 수송손실 기반의 가둠 모델을 그대로 활용하였다. 해당 모델의 타당성을 확인하기 위하여 모델과 실험에서 얻은 에너지 가둠 시간을 비교하였으며, VEST 오믹 방전 적용에 있어서 해당 모델이 합당함을 확인하였다. 플라즈마 내벽 상호작용의 경우, 탄소를 주요 불순물원으로 가정하여 수소 이온에 의한 탄소 원자 방출 계수를 적절히 찾고 검증과정에서 이를 활용하였다.

개발된 시동 모델의 VEST의 적용성에 대한 타당성을 확인하기 위하여 VEST의 여러 오믹 방전을 대상으로 검증과정이 이루어졌다. 오믹 방전은 (1) 중심부 슬레노이드 전류 파형 조건, (2) 외부 폴로이달 자기장 코일 전류 파형 조건 그리고 (3) 플라즈마 내벽 조건으로 분류하여 선정되었다. 세 조건 모두 모델은 전반적으로 실험 데이터를 합당한 수준으로 재생산할 수 있음을 확인하였다. 하지만, VEST에서 일반적으로 플라즈마 전류가 하락하는 구간에서 전자 온도가 상승하는 것이 주로 관측되지만 현재 개발된 모델을 통하여 이를 재생산하는데 한계가 있었다. 이는 플라즈마

의 부피가 급격하게 줄어들면서 발생하는 가열효과로 여겨지며 이러한 효과를 반영하기 위해서는 모델을 개선이 필요할 것으로 보인다. 검증과정을 통해 전반적인 방전 성장은 비교적 재생산을 잘 할 수 있음을 확인하였기 때문에 새로운 타겟 전류 달성을 위한 플라즈마 예측에 본 모델을 활용하였다. 예측 결과를 통하여 중심부 솔레노이드 코일을 +20 kA 에서 -20 kA 으로 50 ms 동안 강하시켜 일주전압을 발생시킬 경우 타겟 플라즈마 전류와 유사한 결과를 얻을 수 있음을 확인할 수 있었다. 다만, 플라즈마 내벽에서 수소 및 불순물 보유 수준이 낮을 경우로 전제가 되었다. 현재 장치에서 보론화 조건의 내벽 상태에서는 수소 보유가 매우 높기 때문에 타겟 플라즈마 전류 달성을 위해서는 진공 내벽 컨디셔닝 방법을 개선할 필요가 있다. 개발된 모델은 VEST 장치뿐만 아니라 중-대형 구형 토러스 장치에서도 적용이 되었다. 중형 구형 토러스 장치인 MAST에서 본 모델의 검증과정이 이루어 졌으며 영국에서 진행중이며 설계 단계에 있는 STEP 프로젝트를 위한 번-스루 예측에 활용이 되었다.

본 연구에서는 무차원의 DYON 시뮬레이터 기반으로 VEST 장치에서 저항 가열 방전 예측을 위한 토카막 초기 시동 모델을 개발하였고, VEST 플라즈마 방전 대상으로 실험 데이터를 재생산하는 검증과정을 거쳤다. 이를 통해 본 모델의 타당성을 확인하였고 이를 바탕으로 타겟 전류를 달성하기 위한 플라즈마 전류 예측에 활용하였다. 또한, MAST 및 STEP 장치에 적용을 통하여 본 모델이 장치의 차이에 제약받지 않고 폭 넓게 활용이 될 수 있다는 것을 확인하였다. 본 연구에서는 개발된 모델을 중심부 솔레노이드에 의한 저항 가열 방전에 국한하여 활용하였지만, 외부 코일 시동이나 이중 플라즈마 머징과 같은 대안적인 시동 방법에도 활용할 수 있을 것이라 기대한다.

주요어: 토카막 시동, 번-스루, 토카막 시동 모델, 전자기장 해석, 구형 토러스, VEST

학 번: 2014-22716